IMPLEMENTATION AND ASSESSMENT OF THE GENERALIZED RIEMANN PROBLEM METHOD IN AN UNSTRUCTURED SOLVER

A THESIS SUBMITTED TO
THE GRADUATE SCHOOL OF NATURAL AND APPLIED SCIENCES
OF
MIDDLE EAST TECHNICAL UNIVERSITY

BY

ULAŞ CANBERK AYAN

IN PARTIAL FULFILLMENT OF THE REQUIREMENTS
FOR
THE DEGREE OF MASTER OF SCIENCE
IN
MECHANICAL ENGINEERING

SEPTEMBER 2022

Approval of the thesis:

IMPLEMENTATION AND ASSESSMENT OF THE GENERALIZED RIEMANN PROBLEM METHOD IN AN UNSTRUCTURED SOLVER

submitted by **ULAŞ CANBERK AYAN** in partial fulfillment of the requirements for the degree of **Master of Science in Mechanical Engineering Department, Middle East Technical University** by,

Prof. Dr. Halil Kalıpçılar
Dean, Graduate School of **Natural and Applied Sciences** ———————

Prof. Dr. Mehmet Ali Sahir Arıkan
Head of Department, **Mechanical Engineering** ———————

Assist. Prof. Dr. Özgür Uğraş Baran
Supervisor, **Mechanical Engineering, METU** ———————

Prof. Dr. Mehmet Haluk Aksel
Co-supervisor, **Mechanical Engineering, METU** ———————

Examining Committee Members:

Prof. Dr. Mehmet Metin Yavuz
Mechanical Engineering, METU ———————

Assist. Prof. Dr. Özgür Uğraş Baran
Mechanical Engineering, METU ———————

Assist. Prof. Dr. Ali Karakuş
Mechanical Engineering, METU ———————

Assist. Prof. Dr. Onur Baş
Mechanical Engineering, TEDU ———————

Assist. Prof. Dr. Hediye Atik
Aerospace Engineering, Atılım University ———————

Date:

I hereby declare that all information in this document has been obtained and presented in accordance with academic rules and ethical conduct. I also declare that, as required by these rules and conduct, I have fully cited and referenced all material and results that are not original to this work.

Name, Surname: Ulaş Canberk Ayan

Signature   :

ABSTRACT

IMPLEMENTATION AND ASSESSMENT OF THE GENERALIZED RIEMANN PROBLEM METHOD IN AN UNSTRUCTURED SOLVER

Ayan, Ulaş Canberk

M.S., Department of Mechanical Engineering

Supervisor: Assist. Prof. Dr. Özgür Uğraş Baran

Co-Supervisor: Prof. Dr. Mehmet Haluk Aksel

September 2022, 89 pages

High-order accuracy in the Computational Fluid Dynamics (CFD) solvers became an important necessity with increasing computational resources and algorithms. Resolving discontinuities and regions where high gradients formed accurately is the main topic for high-order schemes. The Generalized Riemann Problem (GRP) method came to the fore with its ability to improve the accuracy in these regions and discontinuities. With the GRP method, the second-order accuracy is not achieved by the piece-wise linear reconstruction method only but also by time variation of flux and resolved state. In this thesis, the GRP method is implemented in a finite volume, open-source CFD solver. The generalized MINMOD limiter is implemented in the solver and investigated since it is a key ingredient of the GRP method. The robustness and accuracy of the implemented method are tested with five cases in one dimension and compared with analytical solutions and reference solutions. The implemented method is validated for the two-dimensional domain with well-known benchmark tests such as; the inviscid Prandtl-Meyer expansion fan case for evaluating the two-dimensional (2D) performance on rarefaction wave accuracy, inviscid Wedge case for

investigating the 2D performance on shock wave accuracy, and RAE 2822 airfoil case for examining the aerodynamic performance for viscous flows. A three-dimensional study is conducted with ONERA M6 Wing. The results are in good agreement with the experimental results and analytical solutions. Finally, an assessment and discussion are presented for the limiter used in the GRP method.

Keywords: GRP, Riemann solver, Godunov method, CFD, high-resolution

ÖZ

GENELLEŞTİRİLMİŞ RIEMANN PROBLEMİ YÖNTEMİNİN YAPILANDIRILMAMIŞ BİR ÇÖZÜCÜDE UYGULANMASI VE DEĞERLENDİRİLMESİ

Ayan, Ulaş Canberk

Yüksek Lisans, Makina Mühendisliği Bölümü

Tez Yöneticisi: Dr. Öğr. Üyesi. Özgür Uğraş Baran

Ortak Tez Yöneticisi: Prof. Dr. Mehmet Haluk Aksel

Eylül 2022, 89 sayfa

Hesaplamalı akışkanlar dinamiği (HAD) çözücülerinde yüksek dereceli doğruluk, artan hesaplama kaynakları ve algoritmalar ile erişilebilir hale gelmiştir. Yüksek gradyanların oluştuğu bölgelerin ve süreksizliklerin doğru bir şekilde çözülmesi, yüksek mertebeli şemalar için ana konudur. Genelleştirilmiş Riemann Problemi (GRP) yöntemi, bu bölgelerde ve süreksizliklerde doğruluğu iyileştirme yeteneği ile ön plana çıkmıştır. GRP yöntemi sayesinde, ikinci mertebeden doğruluk, sadece parçalı doğrusal yeniden kurma yöntemi ile değil, aynı zamanda akı ve çözülmüş durumun zamana göre değişimi ile elde edilmektedir. Bu tezde, GRP yöntemi, sonlu hacim yöntemini kullanan, açık kaynak kodlu bir HAD çözücüde uygulanmıştır. GRP yönteminin temel bir bileşeni olan genelleştirilmiş MINMOD sınırlayıcısı da çözücüye uygulanmış ve incelenmiştir. Uygulanan yöntemin gürbüzlüğü ve hassasiyeti tek boyutta beş denektaşı ile test edilmiş ve analitik çözümler ve referans çözümler ile karşılaştırılmıştır. Uygulanan bu yöntem, iyi bilinen denektaşı testleri ile iki boyutlu alan için doğrulanmıştır. Bu testlerden ağdasız Prandtl-Meyer genişleme fanı, uygulanan yöntemin iki

boyutlu genişleme dalgası performansını değerlendirmek için; ağdasız kama testi, uygulanan yöntemin iki boyutlu şok dalgası performansını araştırmak için; RAE 2822 kanat profili testi, uygulanan yöntemin ağdalı akışlarda aerodinamik performansını incelemek adına çözülmüştür. ONERA M6 kanadı ile üç boyutlu bir çalışma yapılmıştır. Sonuçlar, deneysel sonuçlar ve analitik çözümlerle iyi bir uyum içindedir. Son olarak GRP yönteminde kullanılan sınırlayıcısı için bir değerlendirme ve tartışma sunulmuştur.

Anahtar Kelimeler: GRP, Riemann çözücüsü, Godunov metodu, HAD, yüksek çözünürlük

To Tarçın, whom I could not spare enough time for...

ACKNOWLEDGMENTS

TABLE OF CONTENTS

LIST OF TABLES

LIST OF FIGURES

FIGURES

LIST OF ABBREVIATIONS

ABBREVIATIONS

1D	One Dimensional
2D	Two Dimensional
3D	Three Dimensional
ADER	Arbitrary Derivative
AoA	Angle of Attack
AUSM	Advection Upstream Splitting Method
CAD	Computer Aided Drawing
CFD	Computational Fluid Dynamics
CUSP	Convective Upwind Split Pressure
EOS	Equation of State
FDM	Finite Difference Method
FEM	Finite Element Method
FVM	Finite Volume Method
FVS	Flux Vector Splitting
GRP	Generalized Riemann Problem
IVP	Initial Value Problem
MHD	Magnetohydrodynamic
MUSCL	Monotone Upwind Schemes for Scalar Conservation Laws
P-M	Prandtl-Meyer
PDE	Partial Differential Equation
RCM	Random Choice Method
RP	Riemann Problem
TVD	Total Variation Diminishing
WENO	Weighted Essentially Non-Oscillatory

LIST OF SYMBOLS

SYMBOLS

ρ	Density
ϕ, ψ	Riemann Invariants
S	Entropy
α_σ	Slope Coefficient
β, α	Characteristic Coordinates
U	Conserved Variable Vector
C_{cfl}	Courant–Friedrichs–Lewy Condition
C_d	Drag Coefficient
F	Flux Vector
e	Internal Energy
C_l	Lift Coefficient
M	Mach Number
C_p	Pressure Coefficient
W	Primitive Variable Vector
p	Pressure
Re	Reynolds Number
σ	Shock Speed
σ_i	Slope of the Cell
R^A	Solution of Associated Riemann Problem
c	Speed of Sound
γ	Ratio of Specific Heats
S_H, S_T	Head and Tail Speeds of Rarefaction Wave
E	Total Energy
T	Temperature
t	Time
u	Velocity

CHAPTER 1

INTRODUCTION

Over the past decades, thanks to increasing computational resources and efficient algorithms, numerical modeling started to play an essential role in research, engineering analysis, and design processes. Due to the high mesh numbers, increasingly complex geometries, and physical conditions, Computational Fluid Dynamics (CFD) has become an area that requires more computational resources. Thus, interest in fast and robust CFD schemes increased day by day. Although experimental measurements still play an important role, CFD has come to the fore with its advantageous features such as cost, time, ease of use, easy adaptation to different conditions, repeatability, and useful outputs for needs. Despite new methods and achievements in CFD, considering the diverse needs in today's ever-changing requirements, there are still many areas for improvement for CFD. One of these areas is the development of high-order methods for the compressible flow regime. Although the first-order methods are robust, fast, and efficient, high-order methods improve the accuracy of the solution without a finer mesh necessity which yields faster, more efficient, and more accurate results.

1.1 Background

In gas and fluid dynamics problems, the flow equations for compressible fluid result in hyperbolic partial differential equations (PDEs) if the flow is assumed as inviscid and adiabatic [1]. There are three common numerical methods used in CFD for PDEs:

- Finite Difference Method (FDM)

- Finite Element Method (FEM)

- Finite Volume Method (FVM)

Integral relations between control volumes and their bounds can be used to derive Euler and Navier-Stokes equations. Discrete domains imply finite control volumes or cells. Therefore, from a computational perspective, it is preferable to utilize integral equations. Locally, the fundamental equations are applied to these control volumes resulting in FVM.

Scalar equations like Burgers' equation or systems of conservation equations like the Euler equations solutions involve shocks and solution discontinuities. Any discontinuity in the solution must be captured by numerical algorithms. Upwind methods are used to capture discontinuities in flow variables rather than central numerical methods. Upwind methods are based on the direction of flow information. Flux Vector Splitting (FVS) and Riemannian are the two most used methods for determining the upwind direction. [2]

1.1.1 Flux Vector Splitting Methods

FVS methods only consider the wave propagation direction. In FVS methods like Van Leer's scheme [3], the convective flux vector is split into two parts with respect to the upwind or downwind direction of specific characteristic variables. On the other hand, there are brand-new FVS methods like Advection Upstream Splitting Method (AUSM) introduced by Liou et al. [4, 5] or the Convective Upwind Split Pressure (CUSP) introduced by Jameson [6, 7].

1.1.2 Riemannian Methods

The fluxes are calculated at the face of the control volume in the Riemannian methods. Differently from the FVS methods, both wave propagation direction and waves themselves are treated in Riemannian methods. In order to calculate the flux, a right and left state is defined at the discontinuity, which is the face of the control volume. Solving local Riemann problems exactly at the faces of cells in order to calculate inter-cell
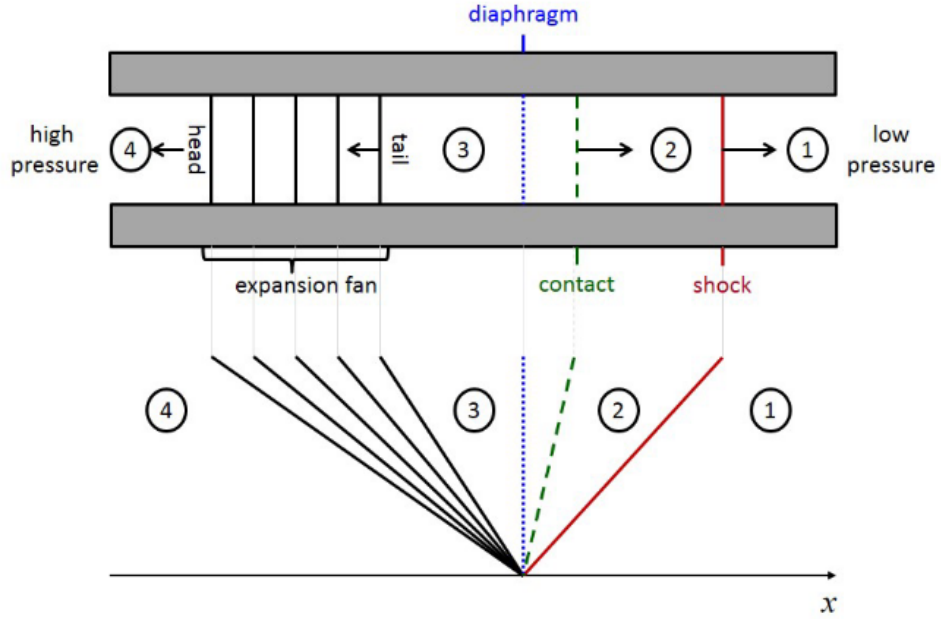
Figure 1.1: Sketch of Shock Tube [10]

fluxes is first introduced by Godunov [8], an extension of the CIR [9] upwind scheme.

1.1.2.1 The Riemann Solvers

The Riemann problem (RP) is defined as a specific initial value problem (IVP) characterized by piece-wise constant initial states and discontinuity, as given in (1.1).

$$u\left(x, t^0\right) = \begin{cases} u_L & if \quad x < x_0 \\ u_R & if \quad x > x_0 \end{cases} \tag{1.1}$$

The RP has an exact analytical solution for the Euler equations. Additionally, because shocks and rarefaction waves may be properties of the solution, it is particularly helpful for understanding the Euler equations. In Euler equations, the shock tube problem is a fundamental physical issue in gas dynamics. A sketch of the shock tube is given in Figure 1.1.

The RP is represented physically by a gas-filled tube with two chambers in different initial data isolated by a removable membrane at $x = x_0$. The wave structure can be one of the four given in Figure 1.2.

3
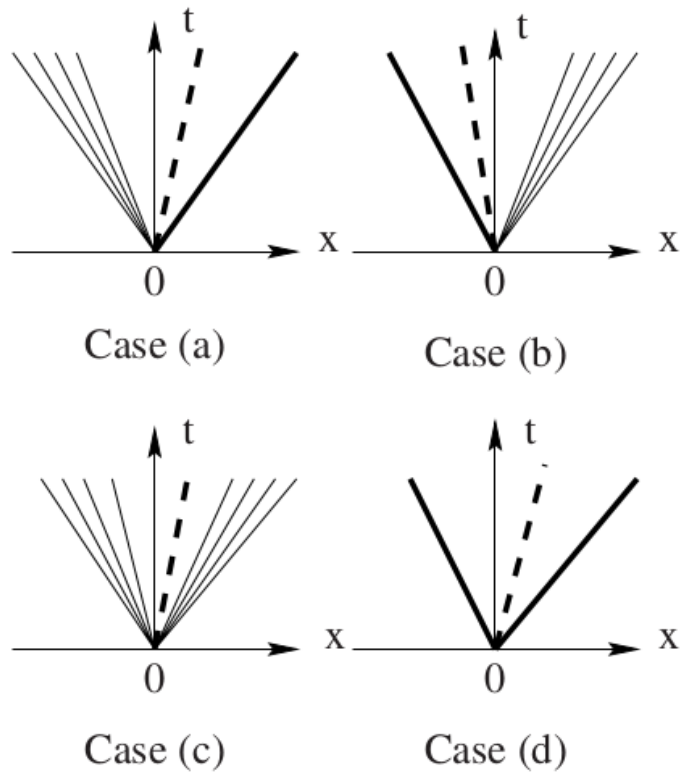
Figure 1.2: Possible wave patterns of RP solution: (a) rarefaction wave, contact discontinuity, shock wave (b) shock wave, contact discontinuity, rarefaction wave(c) rarefaction wave, contact discontinuity, rarefaction wave (d) shock wave, contact discontinuity, shock wave [1]

The Godunov method and its high-order extensions utilize the local exact solution to the RP. Following the Godunov method with exact Riemann solution, approximate Riemann solvers were introduced by Harten, Lax, and van Leer (HLL)[11], Osher et al. [12], Roe [13], HLLE[14], and HLLC (C for contact) [15] for decreasing the computational effort and increasing the robustness.

When applying, assessing, and developing approximate Riemann solvers, a thorough understanding of the exact solution is equally essential since shock and rarefaction waves may appear as characteristics of the solution even if their speeds are estimated. Considering a wave configuration with three constant states, which are separated by two waves, HLL Riemann solvers calculate the inter-cell flux by applying the conservation laws in the integral form. The HLL method ignores the middle wave, the contact discontinuity. In order to calculate the speeds of waves used in the HLL solver, Eindfelt[14] and Davis[16] introduced new methods. The HLL method with wave speed estimate is known as the HLLE solver. However, the two-wave assumption is not correct for Euler equations since this assumption may lead to the low resolution of physical characteristics in the solution. In order to overcome this issue, in 1992, Toro, Spruce, and Speares [15] introduced an extended method called HLLC. The HLLC method involves all three waves, including contact discontinuity. The HLLC method provides better results than HLL at the discontinuity regions while preserving its efficiency. Also, in the last decade, further developments of the HLLC methods, as well as extensive implementations, have been done. Batten et al. [17] introduced new alternatives in order to calculate wave speeds, and Batten, Leschziner, and Goldberg [18] made an implicit version of HLLC available.

1.1.2.2 Beyond the First-Order

Building high-order methods for simulating compressible fluid flow has a growing interest. The first second-order Godunov-type schemes were introduced by Kolgan [19] and van Leer [20]. Thanks to the work of van Leer, the second-order accuracy for Godunov-type schemes were obtained by a piece-wise linear distribution in each cell and named "Monotone Upwind Schemes for Scalar Conservation Laws" (MUSCL). Van Leer pioneered a whole class of reconstruction-evolution methods called MUSCL
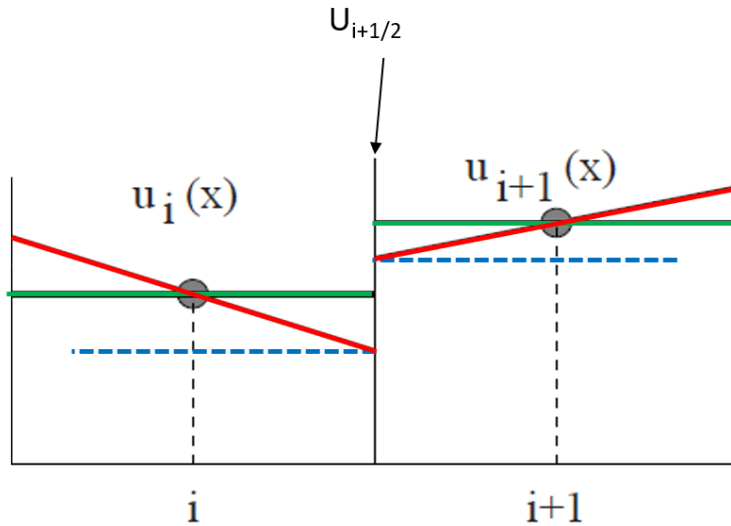
Figure 1.3: Piece-wise Linear Cell Distribution

interpolation. A variety of variations were invented after his original work, and all of these derivatives are commonly referred to as MUSCL interpolations. The sketch of piece-wise linear cell distribution is given in Figure 1.3 and shown by red lines. If the accuracy is first-order, the cell distribution is constant and shown by green lines. Although cell distribution is piece-wise linear, the inputs (left and right states) of the Riemann solver are still taken as constant at the cell boundary and shown by blue dashed lines.

Monotone methods, such as the first-order Godunov scheme, do not produce spurious oscillations. Godunov [8] stated that *"monotone methods are at most first-order accurate."* Nonphysical oscillations may occur where sharp gradients or discontinuities show up in the high-order linear methods. These oscillations are a numerical issue that should be addressed. Constructing high-order methods without nonphysical oscillations is possible with non-linear methods named Total Variation Diminishing (TVD), which are the most widely used ones. According to TVD, the difference between adjacent points must decrease or remain the same. As a result, TVD schemes start with the maximum amount of variation. The principal conditions for a TVD scheme are:

- The maxima must not increase.

6
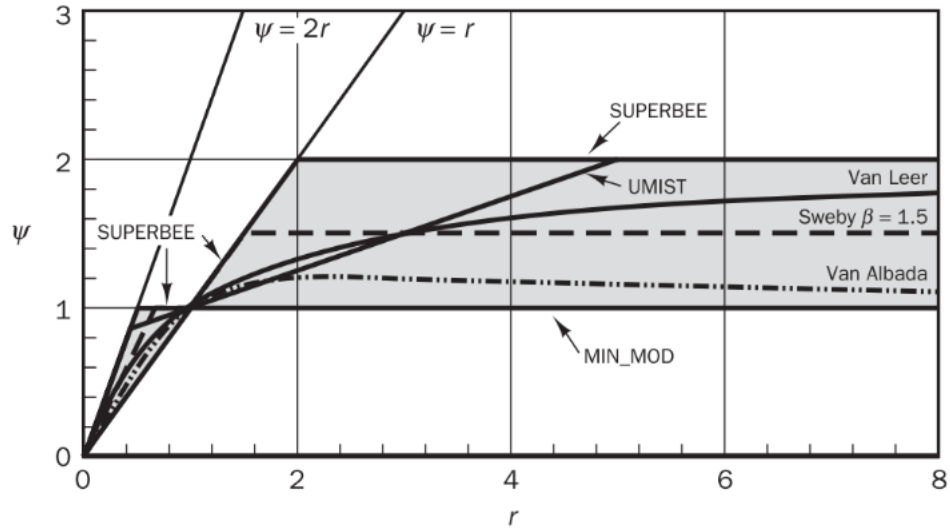
Figure 1.4: Range of Some TVD Schemes [21]

- The minima must not decrease.

- There can be no more local extrema formed.

Limiters are commonly used to resolve the nonphysical oscillations issue and provide TVD property. The forward and backward gradient terms of the aforementioned MUSCL reconstruction are limited by gradient limiters, forcing the scheme to have the TVD feature in a strong shock or discontinuity zone. The range of some possible TVD limiters which are second-order accurate is given in Figure 1.4.

The details of some widely used TVD limiters, such as Van Leer [22], SUPERBEE [23], MINBEE (MINMOD) [23], and Van Albada [24] limiters, can be found in the literature. However, for a variety of reasons, these limiters cannot be directly extended to unstructured grids in the same way as they apply to structured grids [25].

A limiter was developed specifically for unstructured grids by Barth and Jespersen[26]. This limiter, however, has effects comparable to the TVD condition, which decreases accuracy on smooth extrema. As a result, Venkatakrishnan [27] suggested an enhancement by using a differentiable function analogous to the limiter of van Albada, which is built on structured grids.
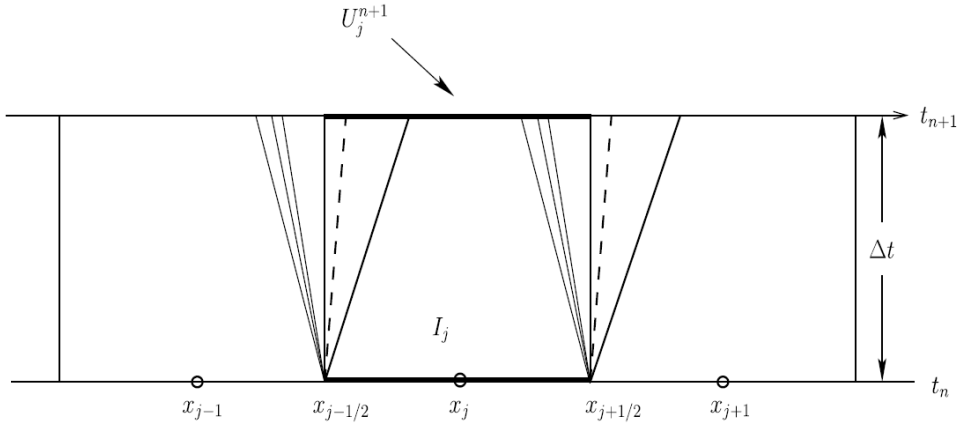
Figure 1.5: A Sketch of Godunov Scheme and Cell Distribution [28]

1.1.2.3 The Generalized Riemann Problem

The associated RP, where constant states are divided by discontinuities, is the Cauchy problem. Although the order of Godunov schemes can be increased by different discretizations, up to this point, the left and right states of the discontinuity remain monotone. The schematic of the values of cells and an example of the application of the RP at each cell face can be seen in Figure 1.5.

For Riemann solvers to produce a time-centered, high-order flux at a specified boundary, it is necessary to assess the state as well as the flux over time. This constitutes the essence of the GRP. It is appropriate to think of the GRP solver as a utility that collects right and left states as well as their gradients at the cell interfaces, which is shown in Figure 1.3 by red lines. The difference between wave configurations of GRP and associated RP is given in Figure 1.6.

An arbitrary but smooth vector field away from the interface can be defined by governing hyperbolic equations, incorporating source terms, to generalize classical, piecewise constant data. This approach was first introduced on Euler equations by Ben-Artzi and Falcovitz[30], named as Generalized Riemann Problem (GRP), which is a second-order accurate scheme that inspired many works.

With the studies of Ben-Artzi and Falcovitz [30], [31], and Ben-Artzi [32], the development of second-order accurate GRP solvers accelerated. It was LeFloch and Raviart [33] and Bourgeade et al. [34] who generalized their formula to any gen-
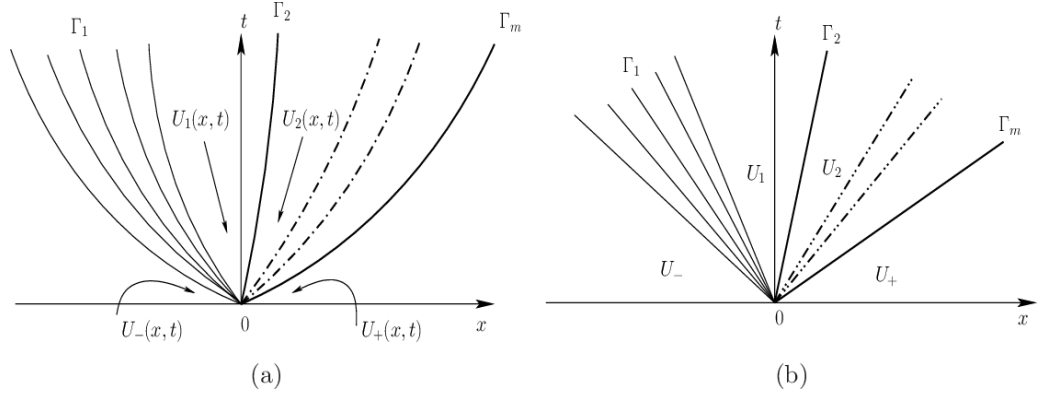
Figure 1.6: (a) Wave Patterns for the GRP (b) Wave Patterns for the Associated RP [29]

eral hyperbolic system with self-similar variables. However, LeFloch and Raviart's work was more thoroughly systematization of the GRP approach. The Ben-Artzi and Falcovitz textbook [35] contributed to the acceptance of GRP solvers.

The GRP development continued by Ben-Artzi, Li, and Warnecke [36] for the Euler system. Also, Ben-Artzi and Li [37] contributed to the development of the GRP method for general systems. In most cases, the direct Eulerian scheme is effective and reliable at capturing shocks and contact discontinuities. Li and Chen have developed a GRP solver for shallow water equations [38]. A GRP solver for third-order accuracy was also developed by Qian, Li, and Wang [28] and for the Euler system by Wu, Yang, and Tang [39]. It has proven to be a challenging task to obtain the exact GRP for the Euler system with an accuracy of more than third order. In the study of Pan et al. [40], the robustness of the GRP method is shown for Navier-Stokes equations. A two-stage fourth-order scheme based on the approximation of GRP and discretization of the fourth-order "Weighted Essentially Non-Oscillatory" (WENO) method was introduced by Li et al. [41, 42], which also demonstrates the robustness of the GRP method in the application of Navier-Stokes equations. Moreover, Du and Li [43] extended the fourth-order accuracy to the fifth-order thanks to the Hermite WENO construction method applied earlier. Yang and Tang [44], as well as Wu and Tang [45], applied the GRP solver to relativistic fluid dynamics. Because thermodynamical influences are properly incorporated into the solver's design, as demonstrated in Li and Wang [46], the analytical and non-linear extraction of the GRP solver can handle very challenging problems like high temperature and high-density flows. For

9

high-order approximations of the linear advection equation, a GRP-type scheme is developed by Berthon, Sarazin, and Turpault [47], with adding another polynomial approximation in order to increase the compactness of the scheme.

PDE evolution and mesh redistribution are two distinct components of the adaptive GRP system presented by Han, Li, and Tang [48]. Zhang and Shang [49] offer an extension of the Random Choice Method (RCM) derived by Toro by using a random sampling technique to select states assigned to the subsequent time level and providing a local solution to the GRP. ADER techniques were developed by Toro et al. [50], Titarev and Toro [51, 52], Montecinos and Toro [53], and Castro and Toro [54] to attempt approximate solutions to the GRP. Taube et al. [55] have developed an ADER scheme for the Magnetohydrodynamic (MHD) problem. Additionally, a GRP method that was based on the LeFloch and Raviart approach was presented by Goetz and Iske [56] and Goetz and Dumbser [57]. According to Ben-Artzi and Falcovitz [35], Ben-Artzi, Li, and Warnecke [36], Ben-Artzi and Li [37], and Han et al. [48], the second-order ADER method can be described as the acoustic variant of GRP. However, the second-order ADER method fails when resolving strong discontinuities.

1.2 Present Study

In the field of CFD, high-order methods can provide considerably more accurate solutions than low-order methods, which is desirable for simulating flows with complex solution structures. This study's objective is to implement a high-order GRP solver into the in-house, open-source finite volume CFD solver, validate and assess its performance under various flow conditions and regimes with various geometries.

In this study, the upwind flux computation with the GRP method [36] is implemented in the open-source solver. Also, new limiter functionalities for unstructured meshes are added to the code base to match the original work. This particular limiter is also assessed in the thesis. In addition to one-dimensional and two-dimensional domains, an assessment on the three-dimensional domain is done, which is missing in the original work.

The results of exact solutions, theoretical solutions, and previously proven performance prediction codes serve as the basis for validating the developed solver that is the subject of this thesis.

1.3   Thesis Layout

The governing equations of the flow are explained in Chapter 2.

In Chapter 3, the numerical methods used in this thesis are presented. Firstly, the exact Riemann solution is explained since it is the heart of both Godunov and the GRP schemes. Then, the Godunov method is introduced with its wave configurations. Finally, the GRP scheme is studied, which is the main scope of this thesis.

In Chapter 4, test cases and results of the solver are presented and discussed. Firstly, the sharp rarefaction and shock wave and contact discontinuity solution accuracy of the GRP implemented solver is validated by comparing with the exact solution and Godunov scheme in different orders with five one-dimensional test cases. Secondly, two-dimensional validation of the GRP solver is done by inviscid wedge, Prandtl-Meyer Expansion, and RAE 2822 airfoil test cases. RAE 2822 Airfoil test case is also validation for the viscous solving capability of the solver and the accuracy of the aerodynamic performance. Finally, a three-dimensional case is solved in order to prove the 3D capability of code and accuracy in different flow regimes with complex geometry.

Finally, the conclusion and future works are presented in Chapter 5.

CHAPTER 2

GOVERNING EQUATIONS

2.1 Euler Equations

The one-dimensional conservative formulation of the differential form of the Euler equations is given by Equation (2.1).

$$U_t + F\left(U\right)_x = 0 \tag{2.1}$$

Vectors of conservative variables and fluxes, U and $F\left(U\right)$, are given in Equation (2.2).

$$U = \begin{bmatrix} \rho \\ \rho u \\ E \end{bmatrix}, \ F = \begin{bmatrix} \rho u \\ \rho u^2 + p \\ u\left(E + p\right) \end{bmatrix} \tag{2.2}$$

Here, ρ is density, u is velocity, p is pressure, and E is the total energy per unit volume defined in Equations (2.3) and (2.4).

$$E = \rho \left(\frac{1}{2} u^2 + e \right) \tag{2.3}$$

$$e = e\left(\rho, p\right) \tag{2.4}$$

where e is the specific internal energy obtained from Equation of State (EOS). The conservation laws (2.1)-(2.2) can also be written in the quasi-linear form:

$$U_t + A(U) U_x = 0 \tag{2.5}$$

The coefficient matrix, i.e., the Jacobian matrix, is defined as in Equation (2.6).

$$A(U) = \frac{\partial F}{\partial U} = \begin{bmatrix} \partial f_1/\partial u_1 & \partial f_1/\partial u_2 & \partial f_1/\partial u_3 \\ \partial f_2/\partial u_1 & \partial f_2/\partial u_2 & \partial f_2/\partial u_3 \\ \partial f_3/\partial u_1 & \partial f_3/\partial u_2 & \partial f_3/\partial u_3 \end{bmatrix} \tag{2.6}$$

For the Euler equations, the Jacobian matrix is calculated as in Equation (2.7).

$$A(U) = \begin{bmatrix} 0 & 1 & 0 \\ -\frac{1}{2}(\gamma-3)\left(\frac{u_2}{u_1}\right)^2 & (3-\gamma)\left(\frac{u_2}{u_1}\right) & (\gamma-1) \\ -\frac{\gamma u_2 u_3}{u_1^2} + (\gamma-1)\left(\frac{u_2}{u_1}\right)^3 & -\frac{\gamma u_3}{u_1} - \frac{3}{2}(\gamma-1)\left(\frac{u_2}{u_1}\right)^2 & \gamma\left(\frac{u_2}{u_1}\right) \end{bmatrix} \tag{2.7}$$

The Jacobian matrix is simplified as in Equation (2.8).

$$A(U) = \begin{bmatrix} 0 & 1 & 0 \\ -\frac{1}{2}(\gamma-3)u^2 & (3-\gamma)u & (\gamma-1) \\ (\gamma-1)u^3 - \gamma u E/\rho & \gamma E/\rho - \frac{3}{2}(\gamma-1)u^2 & \gamma u \end{bmatrix} \tag{2.8}$$

In this equation γ is defined as the ratio of specific heats and found by $\gamma = c_p/c_v$. With the ideal-gas EOS, Euler equations satisfy the homogeneity property as in Equation (2.9).

$$F(U) = A(U) U \tag{2.9}$$

The system's eigenvalues are given in Equation (2.10):

$$\lambda_1 = u - c \,, \ \lambda_2 = u \,, \ \lambda_3 = u + c \tag{2.10}$$

Note that c is the speed of sound. The characteristic polynomial is defined in Equation (2.11).

14

$$|A - \lambda I| = 0 \tag{2.11}$$

Right eigenvectors with vector $K = [k_1, k_2, k_3]^T$, are calculated by solving Equation (2.12).

$$AK = \lambda K \tag{2.12}$$

The solution of Equation (2.12) leads to the three eigenvectors given in Equation (2.13).

$$K^{(1)} = \begin{bmatrix} 1 \\ u - c \\ H - uc \end{bmatrix} , \ K^{(2)} = \begin{bmatrix} 1 \\ u \\ \frac{1}{2}u^2 \end{bmatrix} , \ K^{(3)} = \begin{bmatrix} 1 \\ u + c \\ H + uc \end{bmatrix} \tag{2.13}$$

Note that H is the total enthalpy.

CHAPTER 3

NUMERICAL METHODS

Understanding the Riemann problem (RP) and its solution has a key role in solving a system of conservation laws, which are hyperbolic. In this chapter, the exact solution of the RP, the Godunov scheme, which uses the exact Riemann solution at the cell faces, and the GRP solution are investigated.

3.1 The Riemann Problem

The Initial Value Problem (IVP) for the conservation laws is the RP for the 1D Euler equations;

$$
\left.
\begin{aligned}
U_t + F\left(U\right)_x &= 0\,, \\
U = \begin{bmatrix} \rho \\ \rho u \\ E \end{bmatrix}\,,\ F = \begin{bmatrix} \rho u \\ \rho u^2 + p \\ u\left(E + p\right) \end{bmatrix}\,,
\end{aligned}
\right\}
\tag{3.1}
$$

The initial values for Equation (3.1) are given in Equation (3.2).

$$
U\left(x,0\right) = U^{(0)}(x) = \begin{cases} U_L & if \quad x < 0 \\ U_R & if \quad x > 0 \end{cases}
\tag{3.2}
$$

As introduced in Chapter 1, the RP has an exact analytical solution for the Euler equations; the shock tube problem, a fundamental physical issue in gas dynamics, is a part of the RP in the context of the Euler equations. The RP is represented physically by a gas-filled tube with two chambers separated by a removable membrane at $x =$
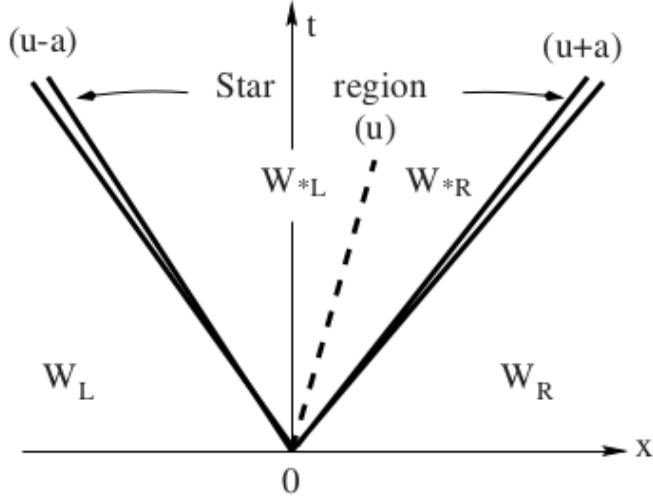
Figure 3.1: Solution Structure of the RP [1]

x_0, as shown in Figure 1.1. When solving the RP, the primitive variable form is employed by the vector of $W = (\rho, u, p)^T$ instead of vector U of conserved variables. The Riemann problem's solution structure is given in Figure 3.1.

Three waves separate four states after the sudden rupture of the diaphragm, which are W_L, W_{*L}, W_{*R}, W_R. Subscripts R and L stand for right and left states in the wave structure. The unknown region between two waves is named as star region, and the contact discontinuity divides this region into two sub-regions. The right and left waves could be shock wave or rarefaction wave, while contact discontinuity is always in the middle. Particle velocity, u_*, and pressure, p_*, are constant throughout the star region, based on the Euler equations' eigenstructure, but two constant quantities exist for density, ρ_{*L} and ρ_{*R}. In the next part, a solution procedure is presented in order to find unknown variables ρ_{*L}, ρ_{*R}, u_*, p_*.

3.1.1   The Exact Solution Procedure For The Riemann Problem

By solving for the root of the algebraic equation given in (3.3) with the ideal gas EOS, pressure p_* can be found.

$$f_L(p, W_L) + f_R(p, W_R) + u_R - u_L = 0 \qquad (3.3)$$

The non-linear wave function f_L is given as in Equation (3.4).

$$f_L\left(p,\,W_L\right) = \begin{cases} (p - p_L)\left[\dfrac{A_L}{p+B_L}\right]^{\frac{1}{2}} & if \quad p > p_L \;\; (shock) \\[2mm] \dfrac{2c_L}{(\gamma-1)}\left[\left(\dfrac{p}{p_L}\right)^{\frac{\gamma-1}{2\gamma}} - 1\right] & if \quad p \le p_L \;\; (rarefaction) \end{cases} \tag{3.4}$$

The non-linear wave function f_R is given as in Equation (3.5).

$$f_R\left(p,\,W_R\right) = \begin{cases} (p - p_R)\left[\dfrac{A_R}{p+B_R}\right]^{\frac{1}{2}} & if \quad p > p_R \;\; (shock) \\[2mm] \dfrac{2c_R}{(\gamma-1)}\left[\left(\dfrac{p}{p_R}\right)^{\frac{\gamma-1}{2\gamma}} - 1\right] & if \quad p \le p_R \;\; (rarefaction) \end{cases} \tag{3.5}$$

The constants are given in Equation (3.6).

$$\left. \begin{array}{ll} A_L = \frac{2}{(\gamma+1)\rho_L}\,, & B_L = \frac{(\gamma-1)}{(\gamma+1)}p_L \\[2mm] A_R = \frac{2}{(\gamma+1)\rho_R}\,, & B_R = \frac{(\gamma-1)}{(\gamma+1)}p_R \end{array} \right\} \tag{3.6}$$

Finally, particle velocity can be obtained from Equation (3.7).

$$u_* = \frac{1}{2}\left(u_L + u_R\right) + \frac{1}{2}\left[f_R\left(p_*\right) - f_L\left(p_*\right)\right] \tag{3.7}$$

The non-linear wave function f_L determines the relationships between the known state W_L on the left side and the undetermined particle speed u_*. The relationships depend on the wave's type (rarefaction or shock). The right data state W_R and the unknown u_* are connected by the function f_R, which determines relations across the right non-linear wave.

ρ_{*R} and ρ_{*L} can be obtained utilizing Equations (3.8) and (3.9). These equations are the relationships between the ratios of pressure and density across the shock waves depending on the direction after u_* and p_* have been calculated.

$$\rho_{*L} = \rho_L\left[\frac{\left(\frac{\gamma-1}{\gamma+1}\right) + \left(\frac{p_*}{p_L}\right)}{\left(\frac{\gamma-1}{\gamma+1}\right)\left(\frac{p_*}{p_L}\right) + 1}\right] \tag{3.8}$$

$$\rho_{*R} = \rho_R \left[\frac{\left(\frac{\gamma-1}{\gamma+1}\right) + \left(\frac{p_*}{p_R}\right)}{\left(\frac{\gamma-1}{\gamma+1}\right)\left(\frac{p_*}{p_R}\right) + 1} \right] \tag{3.9}$$

Similarly, if the type of the waves is rarefaction, Equations (3.10) and (3.11) are used for calculating the ρ_{*L} and ρ_{*R}.

$$\rho_{*L} = \rho_L \left(\frac{p_*}{p_L} \right)^{\frac{1}{\gamma}} \tag{3.10}$$

$$\rho_{*R} = \rho_R \left(\frac{p_*}{p_R} \right)^{\frac{1}{\gamma}} \tag{3.11}$$

The speed of shock waves (S_L, S_R) for left and right directions can be found by Equations (3.12) and (3.13).

$$S_L = u_L - c_L \left[\frac{(\gamma+1)}{2\gamma} \frac{p_*}{p_L} + \frac{\gamma-1}{2\gamma} \right]^{\frac{1}{2}} \tag{3.12}$$

$$S_R = u_R + c_R \left[\frac{(\gamma+1)}{2\gamma} \frac{p_*}{p_R} + \frac{\gamma-1}{2\gamma} \right]^{\frac{1}{2}} \tag{3.13}$$

Note that c_R and c_L are the sound speed of the right and left states. Additionally, the speed of sound upstream of the rarefaction wave is calculated from Equations (3.14) and (3.15).

$$c_{*L} = c_L \left(\frac{p_*}{p_L} \right)^{\frac{\gamma-1}{2\gamma}} \tag{3.14}$$

$$c_{*R} = c_R \left(\frac{p_*}{p_R} \right)^{\frac{\gamma-1}{2\gamma}} \tag{3.15}$$

The calculation of c_* allows for the calculation of the *head* and the *tail* speeds of a rarefaction wave by Equations (3.16) and (3.17).

$$S_{HL} = u_L - c_L , \ S_{TL} = u_* - c_{*L} \tag{3.16}$$

$$S_{HR} = u_R + c_R \, , \ S_{TR} = u_* + c_{*R} \tag{3.17}$$

Finally, the solution for the left fan and right fan inside a rarefaction wave is found in Equations (3.18) and (3.19).

$$W_{Lfan} = \begin{cases} \rho = \rho_L \left[\frac{2}{(\gamma+1)} + \frac{(\gamma-1)}{(\gamma+1)c_L} \left(u_L - \frac{x}{t} \right) \right]^{\frac{2}{\gamma-1}} \\ u = \frac{2}{(\gamma+1)} \left[c_L + \frac{(\gamma-1)}{2} u_L + \frac{x}{t} \right] \\ p = p_L \left[\frac{2}{(\gamma+1)} + \frac{(\gamma-1)}{(\gamma+1)c_L} \left(u_L - \frac{x}{t} \right) \right]^{\frac{2\gamma}{\gamma-1}} \end{cases} \tag{3.18}$$

$$W_{Rfan} = \begin{cases} \rho = \rho_R \left[\frac{2}{(\gamma+1)} - \frac{(\gamma-1)}{(\gamma+1)c_R} \left(u_R - \frac{x}{t} \right) \right]^{\frac{2}{\gamma-1}} \\ u = \frac{2}{(\gamma+1)} \left[-c_R + \frac{(\gamma-1)}{2} u_R + \frac{x}{t} \right] \\ p = p_R \left[\frac{2}{(\gamma+1)} - \frac{(\gamma-1)}{(\gamma+1)c_R} \left(u_R - \frac{x}{t} \right) \right]^{\frac{2\gamma}{\gamma-1}} \end{cases} \tag{3.19}$$

3.1.2   The Godunov Scheme

Godunov [8] developed a conservative application of the first-order upwind technique to non-linear systems of hyperbolic conservation laws. Within each cell boundary, the RP must be resolved, whether it can be an exact solution or a proper approximation, in order for Godunov's method to work. By assuming that there is a local RP at the cell interfaces, the Godunov method assumes that the solution is constant over a cell at a given time t, even though the accuracy is second-order (see Figure 1.3), and evaluates the flow field variables at the following time step. In Figure 3.2, this averaging procedure is illustrated.

In the first version of Godunov's method, new average values, U_i^{n+1}, are defined at time $t^{n+1} = t^n + \Delta t$ by Equation (3.20).

$$U_i^{n+1} = \frac{1}{\Delta x} \int_{x_{i-\frac{1}{2}}}^{x_{i+\frac{1}{2}}} \widetilde{U} \left(x, t^{n+1} \right) dx \tag{3.20}$$

This calculation is applied within each cell $I_i = \left[x_{i-\frac{1}{2}}, x_{i+\frac{1}{2}} \right]$.
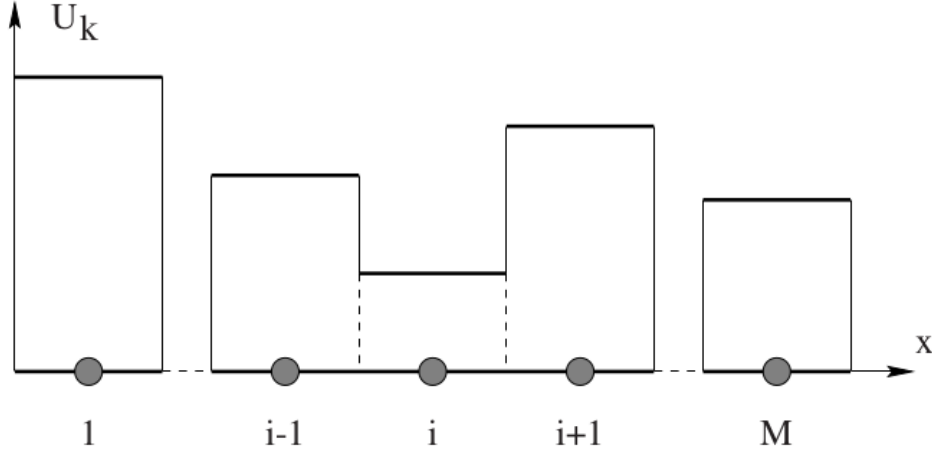
Figure 3.2: The Average Values of Cells for U [1]

Godunov suggests solving the two RPs at the upstream boundary of the cell, $RP\left(U_{i-1}^n, U_i^n\right)$, and downstream boundary of the cell, $RP\left(U_i^n, U_{i+1}^n\right)$, to obtain the solution, which yields the local solutions for $U_{i-\frac{1}{2}}^n$ and $U_{i+\frac{1}{2}}^n$. The U_i^{n+1} is then calculated by the integral average of the solutions, $U_{i-\frac{1}{2}}^n$ and $U_{i+\frac{1}{2}}^n$, as shown by Equation (3.21).

$$U_i^{n+1} = \frac{1}{\Delta x}\int_0^{\frac{1}{2}\Delta x} U_{i-\frac{1}{2}}\left(\frac{x}{\Delta t}\right) dx + \frac{1}{\Delta x}\int_{-\frac{1}{2}\Delta x}^0 U_{i+\frac{1}{2}}\left(\frac{x}{\Delta t}\right) dx \qquad (3.21)$$

One critical point in this method is that one must select Δt such that characteristics of the inter-cell boundaries do not interact; otherwise, incorrect solutions will be found. Due to the drawbacks of this method, a more attractive second edition of Godunov's technique is given by Equation (3.22).

$$U_i^{n+1} = U_i^n + \frac{\Delta t}{\Delta x}\left[F_{i-\frac{1}{2}} - F_{i+\frac{1}{2}}\right] \qquad (3.22)$$

The inter-cell numerical flux can be calculated by Equation(3.24) if the condition is met by the time step Δt, which is given in Equation (3.23).

$$\Delta t \leq \frac{\Delta x}{S_{max}^n} \qquad (3.23)$$

$$F_{i+\frac{1}{2}} = F\left(U_{i+\frac{1}{2}}(0)\right) \qquad (3.24)$$

22
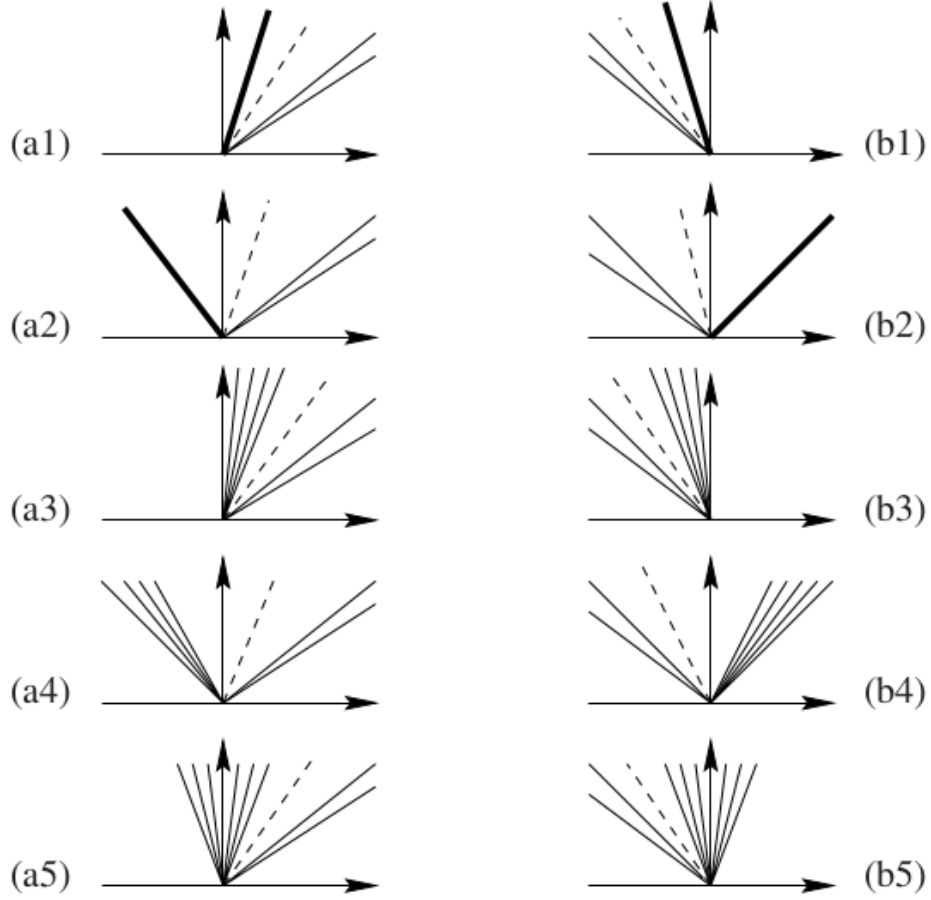
Figure 3.3: Ten Possible Wave Configurations of Godunov Scheme [1]

Inter-cell fluxes $F_{i-\frac{1}{2}}$ and $F_{i+\frac{1}{2}}$ must be calculated in order to march the solution to the next time step using the conservative formula (3.22). The Godunov flux $F_{i+\frac{1}{2}}$ for an ordinary cell interface $x_{i+\frac{1}{2}}$ is calculated using (3.24). The solution $U_{i+\frac{1}{2}}(x/t)$ of the Riemann problem $RP\left(U_i^n, U_{i+1}^n\right)$ calculated at the point $S = x/t = 0$ is therefore required. Figure 3.3 shows Euler equation solutions of ten possible wave configurations.

Five sub-cases (a) arise when the sampling point is located at the contact discontinuity's left, and similarly, the remaining five sub-cases (b) arise when the sampling point is located at the contact discontinuity's right. In Figure 3.3, the shock wave is shown by a thick line, the rarefaction wave is shown by a fan, and the contact discontinuity is shown by a dashed line. If $0 \leq u_*$, in the star region, the particle speed is positive (case a), and the particle speed in the star region is negative (case b) if $u_* \geq 0$.

23

Table 3.1: Ten Possible Sampling Values for Calculating Godunov Flux

Case	(a): particle speed is positive	(b): particle speed is negative
1	W_L	W_R
2	W_{*L}	W_{*R}
3	W_L	W_R
4	W_{*L}	W_{*R}
5	W_{Lfan}	W_{Rfan}

In order to calculate Godunov flux, one must compute the value along the t-axis $(x = 0)$. For case (a) of Figure 3.3, case (a1) is a right shock wave, and the sampling point lies behind the shock wave as the left state, case (a2) is a left shock wave where the sampling point is between two waves, case (a3) is a right rarefaction wave, and sampling point lies behind the rarefaction wave as left state, case (a4) is a left rarefaction wave where sampling point is between two waves finally case (a5) is a sonic rarefaction wave where the sampling point is inside the wave.

For case (b) of the figure, case (b1) is a left shock wave, and the sampling point lies behind the shock wave as the right state, case (b2) is a right shock wave where the sampling point is between two waves, case (b3) is a left rarefaction wave, and sampling point lies behind the rarefaction wave as right state, case (b4) is a right rarefaction wave where sampling point is between two waves finally case (b5) is a sonic rarefaction wave where the sampling point is inside the wave.

A summary of sampled values needed for calculating Godunov flux for ten possible wave configurations is given in Table 3.1.

3.1.2.1 Time Step Size

Up to here, inter-cell flux calculation (3.24) to be used in the conservation formula is presented. With the selection of desired discretization length Δx, the size of the time step Δt must be determined in order to solve Equation (3.22). The C_{cfl} condition is used to determine the time step by Equation (3.25).

$$\Delta t = \frac{C_{cfl}\Delta x}{S_{max}^n} \tag{3.25}$$

Note that the range of C_{cfl} is given in Equation (3.26).

$$0 < C_{cfl} < 1 \tag{3.26}$$

A reliable option for the Euler equations is given in Equation (3.27).

$$S_{max}^n = \max_i \left\{ |u_i^n| + c_i^n \right\} \tag{3.27}$$

3.2 The Generalized Riemann Problem Scheme

The GRP scheme is an analytic extension of the second-order Godunov scheme, which takes the form given in Equation (3.28).

$$U_i^{n+1} = U_i^n - \frac{\Delta t}{\Delta x} \left(F\left(U_{i+\frac{1}{2}}^{n+\frac{1}{2}} \right) - F\left(U_{i-\frac{1}{2}}^{n+\frac{1}{2}} \right) \right) \tag{3.28}$$

In this equation, $U_{i+\frac{1}{2}}^{n+\frac{1}{1}}$ and $U_{i-\frac{1}{2}}^{n+\frac{1}{1}}$ are the value of U at the cell interface $x = x_{i+\frac{1}{2}}$ and $x = x_{i-\frac{1}{2}}$ respectively, averaged over time interval $[t_n, t_{n+1}]$. The GRP method then proceeds to determine the value $U_{i+\frac{1}{2}}^{n+\frac{1}{1}}$ by solving the GRP with second-order accuracy at each point $\left(x_{i+\frac{1}{2}}, t_n \right)$. More specifically, the equations used for calculating the midpoint value $U_{i+\frac{1}{2}}^{n+\frac{1}{1}}$ are:

$$U_{i+\frac{1}{2}}^{n+\frac{1}{2}} = U_{i+\frac{1}{2}}^n + \frac{\Delta t}{2} \left(\frac{\partial U}{\partial t} \right)_{i+\frac{1}{2}}^n, \qquad U_{i+\frac{1}{2}}^n = R^A \left(0; U_{i+\frac{1}{2},-}^n, U_{i+\frac{1}{2},+}^n \right) \tag{3.29}$$

In Equation (3.29), $R^A \left(\left(x - x_{i+\frac{1}{2}} \right) / (t - t_n) ; U_{i+\frac{1}{2},-}^n, U_{i+\frac{1}{2},+}^n \right)$ is the solution to the associated RP for Equation (3.1) centered at $\left(x_{i+\frac{1}{2}}, t_n \right)$. Where $U_{i+\frac{1}{2},-}^n$, and $U_{i+\frac{1}{2},+}^n$ are the limiting values of the initial data on both sides. It is clear that only time

derivative $\left(\frac{\partial U}{\partial t}\right)_{i+\frac{1}{2}}^{n}$ must be defined for the GRP method when the classical Riemann solution $U_{i+\frac{1}{2}}^{n}$ or the Godunov scheme is considered.

The analytical integration of the conservation laws throughout time is the primary component of GRP. In the sections that follow, the direct derivation of the GRP for compressible flows is provided by using Riemann invariants to eliminate the singularity at the discontinuity.

Similar to the Godunov scheme, there are ten possible wave configurations which are given in Figure 3.4. The shock wave, rarefaction wave, and contact discontinuity are illustrated by a thick line, a combination of lines, and a dashed line, respectively. Differently from the Godunov scheme, in the GRP method, the two waves are considered independently from the flow direction when sampling on the t-axis, which is the vertical axis.

For better understanding, wave configuration for the GRP (a) and associated RP (b) in Figure 3.5 can be considered. Differently from the case (b), the waves are not linear in case (a) since variable distribution in cells is not taken as constant when compared with all other second-order schemes. When calculating the flux at the cell boundary, the piece-wise linear reconstruction in the cell and the gradients are taken into account in the GRP method, as given in Figure 1.3 with red lines. A shock wave moves in the right direction, a centered rarefaction wave moves towards the left, and a contact discontinuity separates two waves in the star region. According to the contact discontinuity's location, the left and right intermediate region is indicated by U_1 and U_2, respectively, where velocity u, and pressure p are continuous and density ρ have a jump. U_* is the limiting state.

3.2.1 The Preliminaries

For smooth flows, Euler equations (3.1) become

$$\frac{D\rho}{Dt} + \rho\frac{\partial u}{\partial x} = 0, \qquad \rho\frac{Du}{Dt} + \frac{\partial p}{\partial x} = 0, \qquad \frac{DS}{Dt} = 0 \qquad (3.30)$$

In this equation, S is the entropy, and $D/Dt = \partial/\partial t + u\partial/\partial x$ is the material deriva-
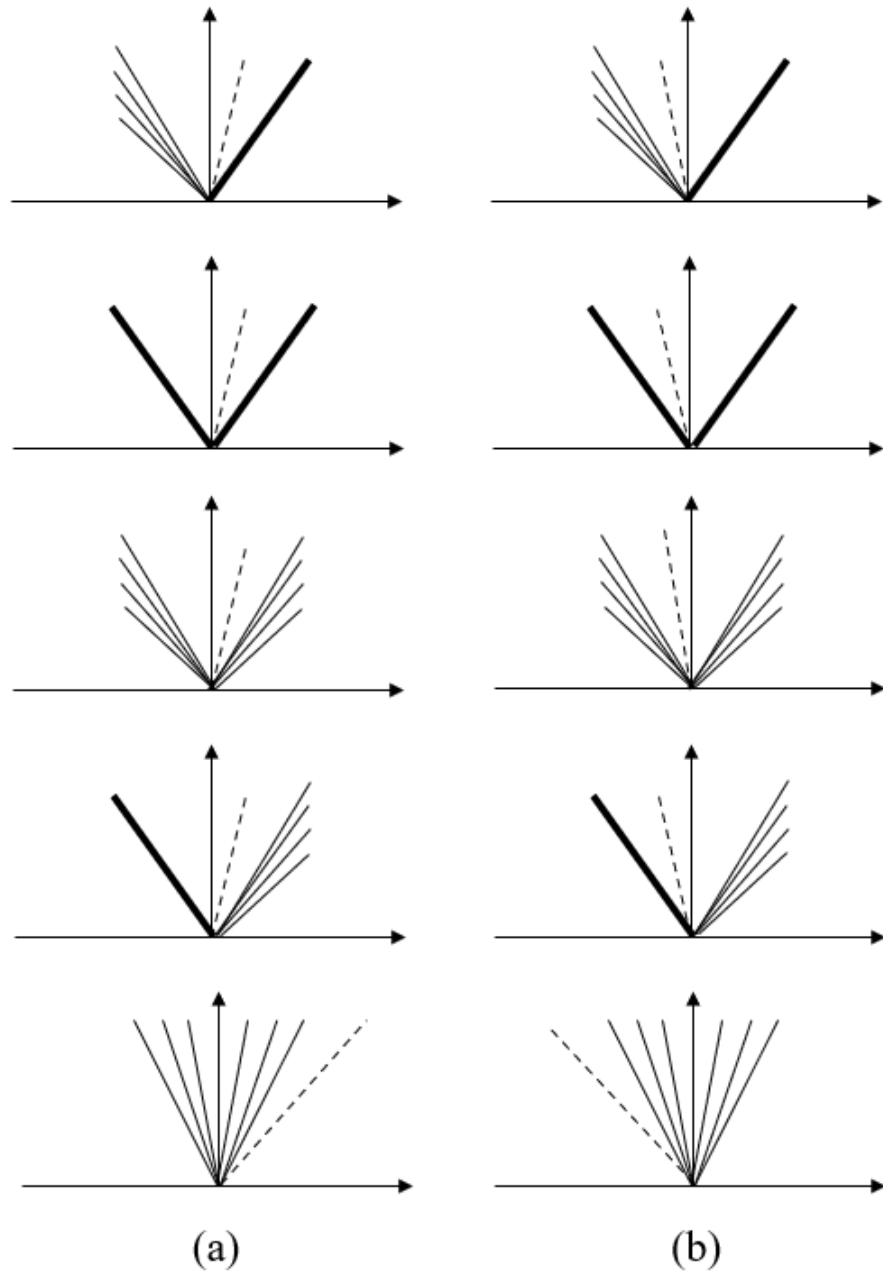
Figure 3.4: Ten Possible Wave Structures of GRP Scheme: (a) $u_* > 0$ (b) $u_* < 0$
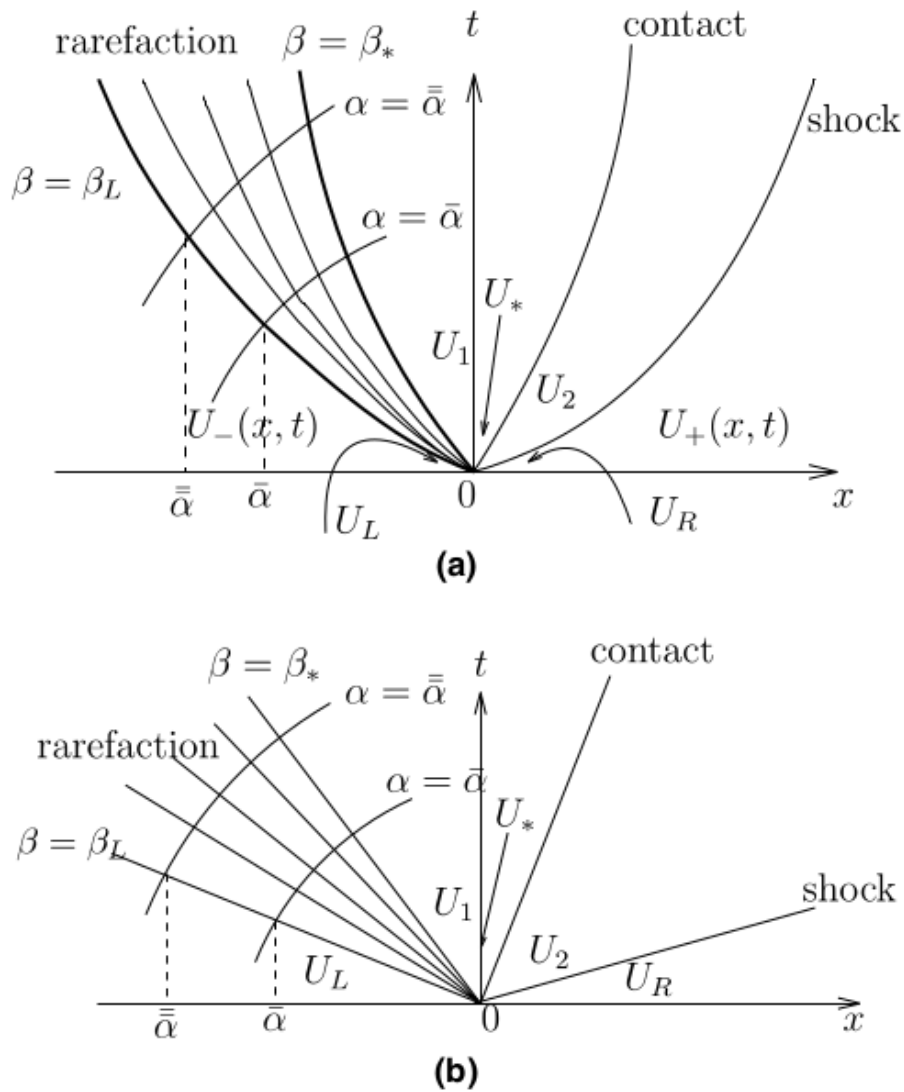
Figure 3.5: Typical Wave Configuration: (a) GRP Solution (b) Associated RP Solution [36]

tive. The energy change can be found in Equation (3.31) by using Temperature T.

$$de = TdS + \frac{p}{\rho^2}d\rho \tag{3.31}$$

The local speed of sound can be calculated by Equation (3.32).

$$c^2 = \frac{\partial p(\rho, S)}{\partial \rho} \tag{3.32}$$

The entropy is constant along a streamline. The Riemann invariants, ϕ and ψ, which are an important part of this scheme, are defined in Equation (3.33).

$$\phi = u - \int^\rho \frac{c(\omega, S)}{\omega}d\omega, \qquad \psi = u + \int^\rho \frac{c(\omega, S)}{\omega}d\omega \tag{3.33}$$

If all thermodynamic components are treated as functions of density and entropy, which is also a Riemann invariant linked to $u-c$ and $u+c$ characteristics, the Equation (3.33) becomes:

$$\phi = u - \frac{2c}{\gamma - 1}, \qquad \psi = u + \frac{2c}{\gamma - 1} \tag{3.34}$$

Note that $c^2 = \gamma p/\rho$ for an ideal gas. Using Equation (3.34),

$$d\phi = du - \frac{\gamma}{(\gamma - 1)\rho c}dp + \frac{c}{(\gamma - 1)\rho}d\rho, \qquad d\psi = du + \frac{\gamma}{(\gamma - 1)\rho c}dp - \frac{c}{(\gamma - 1)\rho}d\rho \tag{3.35}$$

Also,

$$TdS = \frac{dp}{(\gamma - 1)\rho} - \frac{c^2}{(\gamma - 1)\rho}d\rho \tag{3.36}$$

In the GRP scheme, the flow variables are assumed to be piece-wise linear. The initial data can be shown as:

$$U(x,0) = \begin{cases} U_L + xU_L', & x < 0 \\ U_R + xU_R', & x > 0 \end{cases} \tag{3.37}$$

Note that vectors U_L, U_L' U_R U_R' are constant. The associated Riemann solution determines the solution's initial structure up to this point.

3.2.2 The Resolution of Centered Rarefaction Waves

The resolution of centered rarefaction waves (CRWs) is the key component of the GRP scheme. The Riemann invariants remain unchanged along an isentropic rarefaction wave which can be seen in the associated RP. They are still regular within the non-isentropic rarefaction wave, which can be seen in the GRP. The variables ρ, u, and p become singular in terms of the rate of change at the initial discontinuity. Knowing that the entropy is constant along a streamline, the entropy equation can be solved first when separated from the continuity and momentum equations. The primitive variables pressure and velocity are continuous across the contact discontinuity between two waves. Therefore, firstly, the directional derivatives of pressure and velocity are treated, and secondly, the directional derivatives of density are calculated without concerning particle velocity at the star region.

When treating the sonic case, i.e., the sampling point is inside a rarefaction wave, the fact that one of the characteristic curves is tangent to the t-axis, the information obtained from the rarefaction wave can be used to determine how each flow variable changes over time.

At the singularity, $(0,0)$, we can calculate the time derivatives of the flow variables based on the rarefaction wave associated with the $u - c$ characteristic family. The states ahead or behind the rarefaction wave are indicated by $U_-(x,t)$ (respectively, $U_1(x,t)$), see Figure 3.5, where $U_-(x,t)$ corresponds to the left initial data $U_L + U_L'x$. In the rarefaction wave, characteristic curves are denoted by β and α, $\beta_L = u_L - c_L$, $\beta_* = u_* - c_*$. Note that β represents the initial value of slope $u - c$ characteristic at the origin and α is the intersection of transversal characteristic curves with the leading β-curve. These characteristic curves are integrals of Equation (3.38), respectively.

$$\frac{dx}{dt} = u - c, \qquad \frac{dx}{dt} = u + c \qquad (3.38)$$

The limiting values (Du/Dt) and (Dp/Dt) meet the linear relation given in Equation (3.39).

$$a_L \frac{Du}{Dt}(0, \beta) + b_L \frac{Dp}{Dt}(0, \beta) = d_L(\beta) \qquad (3.39)$$

Note that a_L and b_L can be found in Equation (3.40).

$$(a_L, b_L) = \left(1, \frac{1}{\rho_{1*} c_{1*}}\right) \qquad (3.40)$$

The function $d_L(\beta)$ only depends on the associated Riemann solution and the initial states, which can be calculated by Equation (3.41).

$$d_L = \left[\frac{1 + \mu^2}{1 + 2\mu^2}\left(\frac{c_{1*}}{c_L}\right)^{1/(2\mu^2)} + \frac{\mu^2}{1 + 2\mu^2}\left(\frac{c_{1*}}{c_L}\right)^{(1+\mu^2)/\mu^2}\right] T_L S_L' - c_L \left(\frac{c_{1*}}{c_L}\right)^{1/(2\mu^2)} \psi_L' \qquad (3.41)$$

Similarly, the coefficients where rarefaction wave linked with $u + c$ characteristic family can be found from Equations (3.42) and (3.43).

$$(a_R, b_R) = \left(1, -\frac{1}{\rho_{2*} c_{2*}}\right) \qquad (3.42)$$

$$d_R = \left[\frac{1 + \mu^2}{1 + 2\mu^2}\left(\frac{c_{2*}}{c_R}\right)^{1/(2\mu^2)} + \frac{\mu^2}{1 + 2\mu^2}\left(\frac{c_{2*}}{c_R}\right)^{(1+\mu^2)/\mu^2}\right] T_R S_R' + c_R \left(\frac{c_{2*}}{c_R}\right)^{1/(2\mu^2)} \phi_R' \qquad (3.43)$$

Note that $\mu^2 = \frac{\gamma - 1}{\gamma + 1}$.

3.2.3 The Resolution of Shock Waves

The resolution of shock waves is treated with the idea of van Leer [20]. The instantaneous values of temporal derivatives are obtained by resolving a pair of two equations in terms of material derivatives of velocity and pressure. Along the shock wave, which belongs $u + c$ family of characteristics, assuming the propagation speed is positive and to the right direction, the Rankine-Hugoniot condition can be expressed in the form given in Equation (3.44).

$$u = \overline{u} + \Phi\left(p; \overline{p}, \overline{\rho}\right) \tag{3.44}$$

the (ρ, p)-Rankine-Hugoniot condition is defined in Equation (3.45).

$$\rho = H\left(p; \overline{p}, \overline{\rho}\right) \tag{3.45}$$

The speed of the shock wave can be found from Equation (3.46).

$$\sigma = \frac{\rho u - \overline{\rho u}}{\rho - \overline{\rho}} \tag{3.46}$$

In the pre-shock region, the time derivatives of $\overline{U}$ can be replaced by the x-derivatives of U, and similarly, in the post-shock region, the x-derivatives of U can be replaced by the time derivatives. The variables p and u are continuous over the contact discontinuity, and therefore the total derivatives Dp/Dt and Du/Dt are also continuous in between two waves. By taking the limit $t \rightarrow 0_+$, total derivatives can be calculated from Equation (3.47).

$$\frac{Du}{Dt} \rightarrow \left(\frac{Du}{Dt}\right)_*, \qquad \frac{Dp}{Dt} \rightarrow \left(\frac{Dp}{Dt}\right)_*, \qquad \frac{\partial \overline{U}}{\partial x} \rightarrow U'_R \tag{3.47}$$

Moreover,

$$(\rho, u, p) \rightarrow (\rho_{2*}, u_*, p_*), \qquad (\overline{\rho}, \overline{u}, \overline{p}) \rightarrow (\rho_R, u_R, p_R) \tag{3.48}$$

The limiting values $(Du/Dt)_*$ and $(Dp/Dt)_*$ can be found from Equation (3.49).

$$a_R \left(\frac{Du}{Dt} \right)_* + b_R \left(\frac{Dp}{Dt} \right)_* = d_R \qquad (3.49)$$

The constants a_R, b_R, d_R depend only on the associated RP and initial states, described in Equation (3.50).

$$
\begin{aligned}
a_R &= 1 + \rho_{2*}.\left(\sigma_R - u_* \right).\Phi_1 \\
b_R &= - \left[\frac{1}{\rho_{2*}.c_{2*}^2}.\left(\sigma_R - u_* \right) + \Phi_1 \right] \\
d_R &= L_p^R.p_R' + L_u^R.u_R' + L_\rho^R.\rho_R'
\end{aligned}
\qquad (3.50)
$$

The constants in Equation (3.50) can be calculated from Equations (3.51) and (3.52).

$$
\begin{aligned}
L_p^R &= -\frac{1}{\rho_R} + \left(\sigma_R - u_R \right).\Phi_2 \\
L_u^R &= \sigma_R - u_R - \rho_R.c_R^2.\Phi_2 - \rho_R.\Phi_3 \\
L_\rho^R &= \left(\sigma_R - u_R \right).\Phi_3
\end{aligned}
\qquad (3.51)
$$

$$\Phi_1 = \frac{\partial \Phi}{\partial p}\left(p_*; p_R, \rho_R \right), \qquad \Phi_2 = \frac{\partial \Phi}{\partial \overline{p}}\left(p_*; p_R, \rho_R \right), \qquad \Phi_3 = \frac{\partial \Phi}{\partial \overline{\rho}}\left(p_*; p_R, \rho_R \right) \qquad (3.52)$$

The coefficients that correspond to the $u - c$ characteristic family for the shock wave can be found similarly from Equation (3.53).

$$
\begin{aligned}
a_L &= 1 - \rho_{1*}.\left(\sigma_L - u_* \right).\Phi_1 \\
b_L &= -\frac{1}{\rho_{1*}.c_{1*}^2}.\left(\sigma_L - u_* \right) + \Phi_1 \\
d_L &= L_p^L.p_R' + L_u^L.u_R' + L_\rho^L.\rho_R'
\end{aligned}
\qquad (3.53)
$$

The constants in Equation (3.53) can be calculated from Equations (3.54) and (3.55).

$$
\begin{aligned}
L_p^L &= -\frac{1}{\rho_L} - \left(\sigma_L - u_L \right).\Phi_2 \\
L_u^L &= \sigma_L - u_L + \rho_L.c_L^2.\Phi_2 + \rho_L.\Phi_3 \\
L_\rho^L &= - \left(\sigma_L - u_L \right).\Phi_3
\end{aligned}
\qquad (3.54)
$$

$$\Phi_1 = \frac{\partial \Phi}{\partial p}\left(p_*; p_L, \rho_L\right), \qquad \Phi_2 = \frac{\partial \Phi}{\partial \overline{p}}\left(p_*; p_L, \rho_L\right), \qquad \Phi_3 = \frac{\partial \Phi}{\partial \overline{\rho}}\left(p_*; p_L, \rho_L\right)$$

$$(3.55)$$

3.2.4 Solutions for Time Derivative

As mentioned earlier in Part 3.2, the time derivative $\left(\frac{\partial U}{\partial t}\right)_*$ must be determined for the GRP scheme. Assuming the shock wave proceeds to the right and CRW to the left direction, as shown in Figure 3.5, the primitive variables u and p, total derivatives Dp/Dt, and Du/Dt, and therefore, the limiting values $(Dp/Dt)_*$ and $(Du/Dt)_*$ are constant across the contact discontinuity. From this information, calculating first the limiting values $(Dp/Dt)_*$ and $(Du/Dt)_*$, then time derivatives $\left(\frac{\partial u}{\partial t}\right)_*$ and $\left(\frac{\partial p}{\partial t}\right)_*$ will yield $\left(\frac{\partial \rho}{\partial t}\right)_*$.

The Nonsonic Case   For the nonsonic case, i.e., when the sampling point (t-axis) is not inside a rarefaction wave, the limiting values can be obtained from the solution of the pair of linear algebraic Equation (3.56).

$$\begin{aligned} a_L \left(\frac{Du}{Dt}\right)_* + b_L \left(\frac{Dp}{Dt}\right)_* &= d_L \\ a_R \left(\frac{Du}{Dt}\right)_* + b_R \left(\frac{Dp}{Dt}\right)_* &= d_R \end{aligned}$$

$$(3.56)$$

The limiting values of the time derivatives can be obtained from Equation (3.57).

$$\begin{aligned} \left(\frac{\partial u}{\partial t}\right)_* &= \left(\frac{Du}{Dt}\right)_* + \frac{u_*}{\rho_* c_*^2}\left(\frac{Dp}{Dt}\right)_* \\ \left(\frac{\partial p}{\partial t}\right)_* &= \left(\frac{Dp}{Dt}\right)_* + \rho_* u_*\left(\frac{Du}{Dt}\right)_* \end{aligned}$$

$$(3.57)$$

The Sonic Case   For the sonic case, i.e., when the sampling point (t-axis) is inside a rarefaction wave, the limiting values can be obtained from the Equations (3.58) and (3.59).

$$\left.\begin{aligned} \left(\frac{\partial u}{\partial t}\right)_* &= d_L\left(0\right) \\ \left(\frac{\partial p}{\partial t}\right)_* &= \rho_* u_* d_L\left(0\right) \end{aligned}\right\} \qquad if \qquad left\ rarefaction \qquad (3.58)$$

$$
\left.\begin{array}{r}
\left(\frac{\partial u}{\partial t}\right)_* = d_R\left(0\right) \\[2mm]
\left(\frac{\partial p}{\partial t}\right)_* = \rho_* u_* d_R\left(0\right)
\end{array}\right\} \qquad if \qquad right\ rarefaction \qquad (3.59)
$$

Depending on the propagation direction of contact discontinuity and wave type, $(\partial \rho / \partial t)_*$ can be calculated by Equation (3.60) if $u_* > 0$.

$$
\left(\frac{\partial \rho}{\partial t}\right)_* =
\begin{cases}
\frac{1}{c_*^2}\left(\left(\frac{\partial p}{\partial t}\right)_* + (\gamma - 1)\,\rho_* u_* \left(\frac{c_*}{c_L}\right)^{\left(1+\mu^2\right)/\mu^2} T_L S_L'\right) & (left\ rarefaction)\,, \\[3mm]
\left(u_* . f_L - g_p^L \left(\frac{\partial p}{\partial t}\right)_* - g_u^L \left(\frac{\partial u}{\partial t}\right)_*\right) / g_\rho^L & (left\ shock)\,,
\end{cases}
$$
$$(3.60)$$

If $u_* < 0$, $(\partial \rho / \partial t)_*$ can be calculated by the Equation (3.61).

$$
\left(\frac{\partial \rho}{\partial t}\right)_* =
\begin{cases}
\frac{1}{c_*^2}\left(\left(\frac{\partial p}{\partial t}\right)_* + (\gamma - 1)\,\rho_* u_* \left(\frac{c_*}{c_R}\right)^{\left(1+\mu^2\right)/\mu^2} T_R S_R'\right) & (right\ rarefaction)\,, \\[3mm]
\left(u_* . f_R - g_p^R \left(\frac{\partial p}{\partial t}\right)_* - g_u^R \left(\frac{\partial u}{\partial t}\right)_*\right) / g_\rho^R & (right\ shock)\,,
\end{cases}
$$
$$(3.61)$$

The constants can be calculated from Equation (3.62).

$$
\begin{array}{lll}
g_\rho^L = u_* - \sigma_L, & g_p^L = \frac{\sigma_L}{c_{1*}^2} - u_* H_1, & g_u^L = u_* . \rho_{1*}\left(\sigma_L - u_*\right).H_1 \\[2mm]
g_\rho^R = u_* - \sigma_R, & g_p^R = \frac{\sigma_R}{c_{2*}^2} - u_* H_1, & g_u^R = u_* . \rho_{2*}\left(\sigma_R - u_*\right).H_1
\end{array}
\qquad (3.62)
$$

3.2.5 Algorithm of GRP Scheme

The algorithm of the GRP scheme [36] is given by the following four steps:

Step 1. Solve the RP at inter-cell to define the Riemann solution using Equation (3.63).

$$
U_{i+\frac{1}{2}}^n = R^A \left(0; U_i^n + \frac{\Delta x}{2}\sigma_i^n, U_{i+1}^n - \frac{\Delta x}{2}\sigma_{i+1}^n\right) \qquad (3.63)
$$

which results in the Godunov scheme if $\sigma_i^n \equiv 0$.

Step 2. Compute time derivative $\left(\frac{\partial U}{\partial t}\right)_*$ according to the formulae given above sections and determine the numerical flux using Equation (3.64).

$$U_{i+\frac{1}{2}}^{n+\frac{1}{2}} = U_{i+\frac{1}{2}}^n + \frac{\Delta t}{2}\left(\frac{\partial U}{\partial t}\right)_{i+\frac{1}{2}}^n \tag{3.64}$$

Step 3. By using Equation (3.65), determine the new cell averages U_i^{n+1}.

$$U_i^{n+1} = U_i^n - \frac{\Delta t}{\Delta x}\left(F\left(U_{i+\frac{1}{2}}^{n+\frac{1}{2}}\right) - F\left(U_{i-\frac{1}{2}}^{n+\frac{1}{2}}\right)\right) \tag{3.65}$$

Step 4. Calculate the new slope using a slope limiter and Equations (3.66) and (3.67).

$$\begin{aligned} U_{i+\frac{1}{2}}^{n+1,-} &= U_{i+\frac{1}{2}}^n + \Delta t\left(\frac{\partial U}{\partial t}\right)_{i+\frac{1}{2}}^n \\ \sigma_i^{n+1,-} &= \frac{1}{\Delta x}\left(U_{i+\frac{1}{2}}^{n+1,-} - U_{i-\frac{1}{2}}^{n+1,-}\right) \end{aligned} \tag{3.66}$$

$$\sigma_i^{n+1} = minmod\left(\alpha_\sigma \frac{U_i^{n+1} - U_{i-1}^{n+1}}{\Delta x}, \sigma_i^{n+1,-}, \alpha_\sigma \frac{U_{i+1}^{n+1} - U_i^{n+1}}{\Delta x}\right) \tag{3.67}$$

This slope calculation procedure is an essential ingredient of the GRP scheme since it is not affected by the new cell averages, which distinguishes this scheme from other second-order high-resolution techniques, where α_σ is between $(0, 2]$.

This slope limiter used in the GRP method is a modified version of the generalized MINMOD limiter of van Leer[20]. Since the time variation of variables $\left(\frac{\partial U}{\partial t}\right)$ is taken into account in the GRP method, the application of the limiter is specific to this scheme. Van Leer's generalized MINMOD limiter has a high impact on the solution resolution and will be discussed in the next chapter.

CHAPTER 4

RESULTS AND DISCUSSION

The upwind flux computation with the GRP method is implemented in the open-source, FVM-based solver. The implemented solver, FLOWPSI, was developed by Luke et al. [58]. The flow solver is built on a rule-based programming framework named LoCi. This flow solver can resolve the three-dimensional steady-state or unsteady problems of the Euler and Navier-Stokes equations. The solver can work with both structured and unstructured grids, in addition. The solver employs third-order explicit Runge-Kutta method and implicit methods for the integration in time. Moreover, second-order exact and approximate (HLLC) Riemannian convective flux schemes are included in the solver. The gradients in cells are calculated by the least squares method, and they are limited by Barth-Jaspersen and Venkatakrishnan limiters for spatial discretization accuracy.

Firstly, the implemented GRP algorithm is tested in the 1D domain with available limiters. However, obtained results are not close to the reference results. In order to assess this issue in a detailed way, a structured, 1D prototype solver is developed in MATLAB with generalized MINMOD limiter used as in the original work [36]. In addition, thanks to this prototype solver, the solver differences, such as time integration and gradient calculation between original work and unstructured solver, are minimized.

After validating the implemented method in the prototype solver, the generalized MINMOD limiter is also implemented in our solver, FLOWPSI, since it improves the accuracy of results and the obtained results fit well with the reference results. It is observed that the limiter is the driving component of the GRP method. This observation is discussed briefly at the end of this chapter.

37

Table 4.1: Test Plan

Test Step	Step Name	Aim
1	GRP MATLAB	Implementation verification and limiter assessment
2	GRP FLOWPSI	Production code verification and implementation
3	P-M Expansion	Rarefaction wave performance in 2D
4	Inviscid Wedge	Shock wave performance in 2D
5	RAE 2822 Airfoil	Aerodynamic performance for viscous flows
6	ONERA M6 Wing	Performance in 3D

In this chapter, one-dimensional shock tube test cases are analyzed in different aspects. Secondly, two-dimensional problems such as inviscid wedge flow, inviscid Prandtl-Meyer expansion fan, and RAE 2822 transonic airfoil are studied. Finally, the three-dimensional ONERA M6 wing is tested. The test plan is given in Table 4.1.

4.1 One-Dimensional Results

Five 1D shock tube problems are investigated in order to assess the performance of the GRP method for the Euler equations with the developed solver in MATLAB and FLOWPSI. Also, the numerical results of the first-order and second-order Godunov schemes, the exact solutions, and reference results [36] are used for comparison. The left and right constant states of the tests are given in Table 4.2. The tests are taken from [1] and [36]. In section 4.1.1, the results from prototype MATLAB implementation for the GRP method and first-order Godunov scheme are presented with the reference results. Results of FLOWPSI and comparison with reference results [36] are given in section 4.1.2.

4.1.1 Results of Prototype Solver

In all cases, the computational domain is divided into $N = 100$ cells, where domain length L is taken as 1. The ratio of specific heats is selected as $\gamma = 1.4$. The C_{cfl} is taken as 0.1. A discontinuity separates two constant states, which are given in Table 4.2. For the exact solution, the open-source code developed and distributed by Toro

38

Table 4.2: Left and Right States for Five Test Problems

Test	ρ_L	u_L	p_L	ρ_R	u_R	p_R
1	1.0	0.0	1.0	0.125	0.0	0.1
2	1.0	-2.0	0.4	1.0	2.0	0.4
3	1.0	0.0	1000.0	1.0	0.0	0.01
4	5.99924	19.5975	460.894	5.99242	-6.19633	46.0950
5	1.0	-19.59745	1000.0	1.0	-19.59745	0.01

[59] is used. In the results, velocity, pressure, density, and internal energy variables are presented where exact results are shown by the black line; gray triangles indicate reference results, blue circles demonstrate first-order Godunov scheme results, and red crosses indicate solutions of the GRP method with generalized MINMOD limiter from MATLAB.

4.1.1.1 Test Case 1

This test case, which is named as Sod problem [60], consists of a right shock wave, a left rarefaction wave, and contact discontinuity moving in the right direction. The purpose of this test case is to evaluate the accuracy of numerical methods. The gas is initially at rest. Initial discontinuity position has chosen as $x_0 = 0.5$. The results at $T = 0.15$ seconds are shown in Figure 4.1.

The rarefaction wave (which can be seen between $x \approx 0.3$ and $x \approx 0.5$) is well approximated by the GRP method; differently than the Godunov scheme, the accuracy near the head and tail is better.

The shock wave (can be seen at $x \approx 0.75$) is approximated over four computing cells in the first-order method and three computing cells in the GRP scheme without nonphysical oscillations, which shows the shock wave resolution of the GRP method.

It is more challenging to resolve contact discontinuities (which can be seen at $x \approx 0.65$) accurately than resolving the shock waves due to their linear characteristic. It is seen that the GRP method has better resolution than the Godunov scheme when compared.
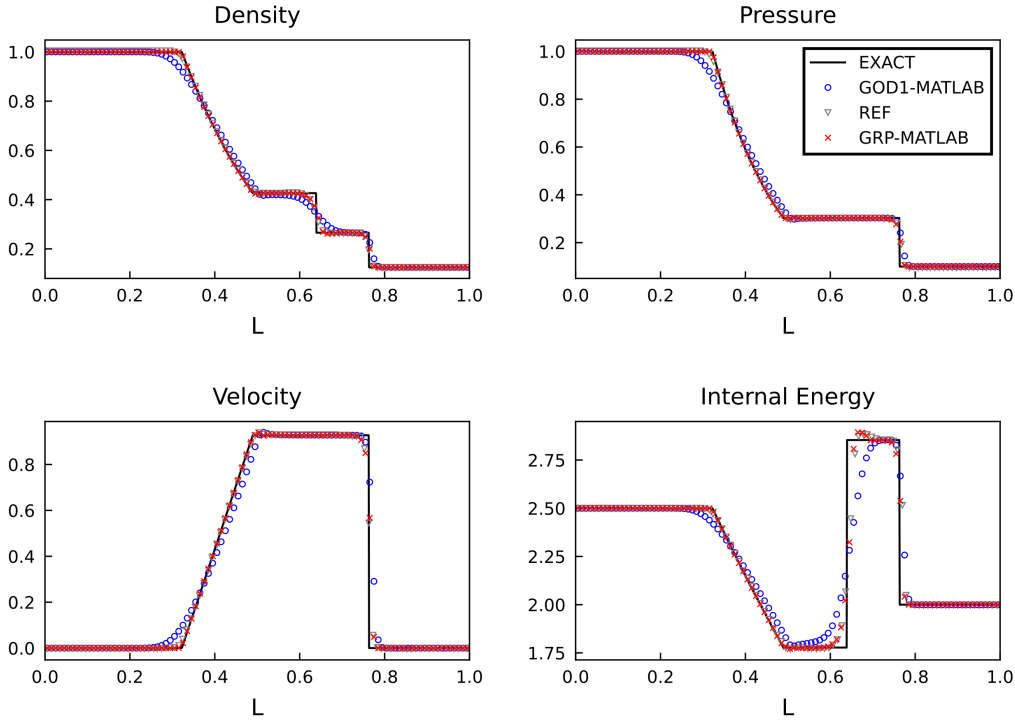
Figure 4.1: Results of Test Case 1

In all figures, the results are in near-perfect fit with the reference study.

4.1.1.2 Test Case 2

This test case, commonly known as the "123 problem", is appropriate for evaluating the effectiveness of numerical techniques flows near a vacuum [61]. A contact discontinuity at $x_0 = 0.5$ with zero speed separates the two symmetric rarefaction waves where the star region is close to the vacuum. The results at $T = 0.1$ seconds are shown in Figure 4.2.

Although the first-order Godunov method shows satisfactory results when ρ, u, p, and E are considered, the GRP method is better near the head of the rarefaction waves. When specific internal energy, e, is considered, the Godunov scheme can be considered unsatisfactory where density and pressure get closer to zero, which results in growing errors in internal energy. It is widely acknowledged that internal energy plots can disclose a lot about the quality of the numerical solution. Moreover, the low-density problems cause numerical schemes to diverge or fail; thus, they also show the
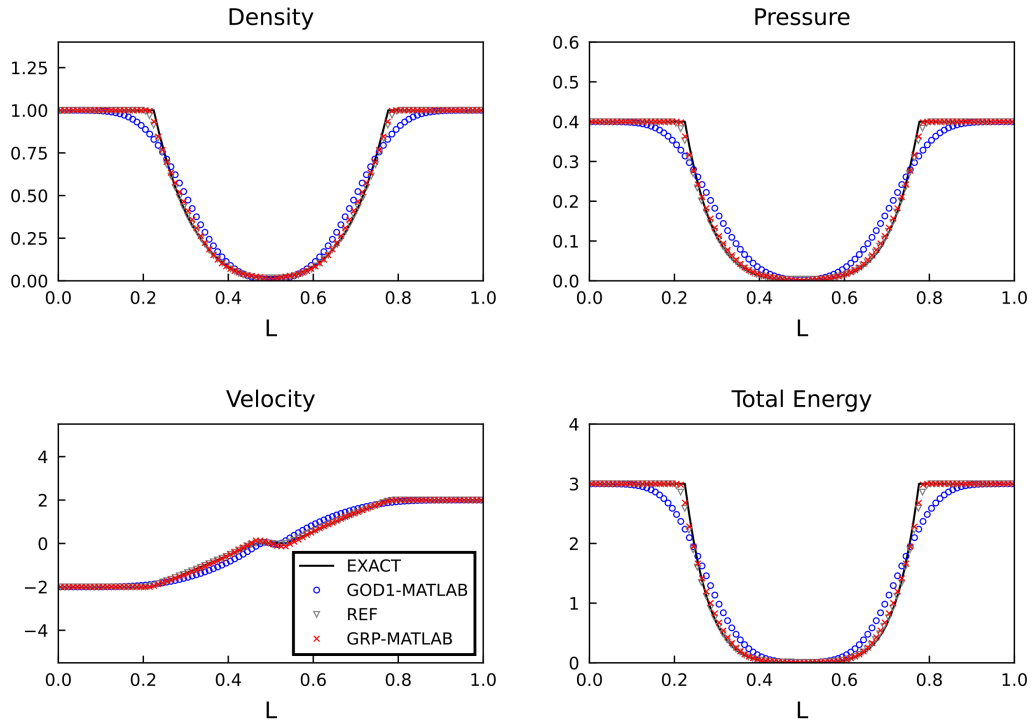
Figure 4.2: Results of Test Case 2

robustness of the methods. The internal energy results are shown in Figure 4.3, where the GRP method proves its superiority. In addition, the solution of the GRP method is in good agreement with the reference solution.

The contact discontinuity stays at $x = 0.5$ since the left and right rarefaction waves are characteristically equal.

4.1.1.3 Test Case 3

The purpose of this test case is to evaluate the accuracy and robustness of numerical methods in the presence of very strong shock waves, rarefaction waves, and contact discontinuities. This problem is left half of the Woodward and Colella [62] problem, and the location of initial discontinuity is at $x_0 = 0.5$. The results at $T = 0.012$ seconds are shown in Figure 4.4.

The GRP method performs well both in the head and tail of the rarefaction wave (which can be seen between $x \approx 0.1$ and $x \approx 0.3$) only with a slight overshoot in the velocity plot. This oscillation is typically close to strong discontinuities for
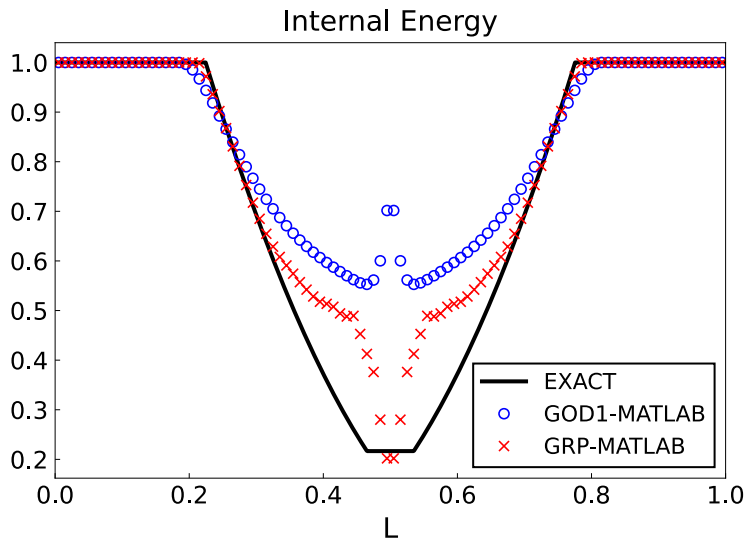
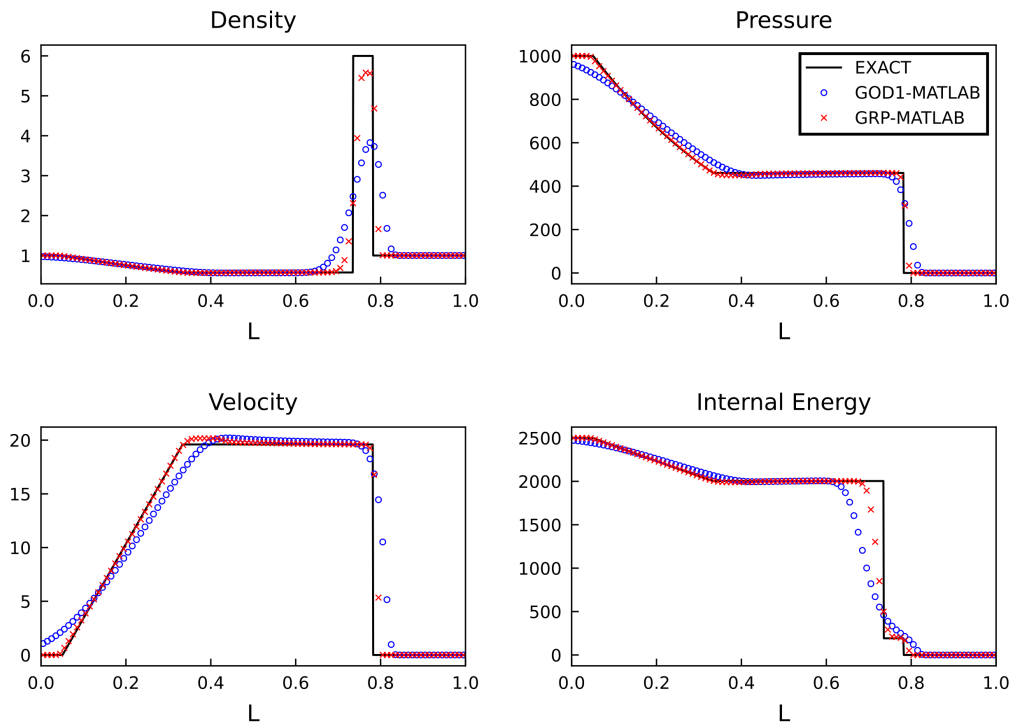Figure 4.3: Internal Energy Results of Test Case 2
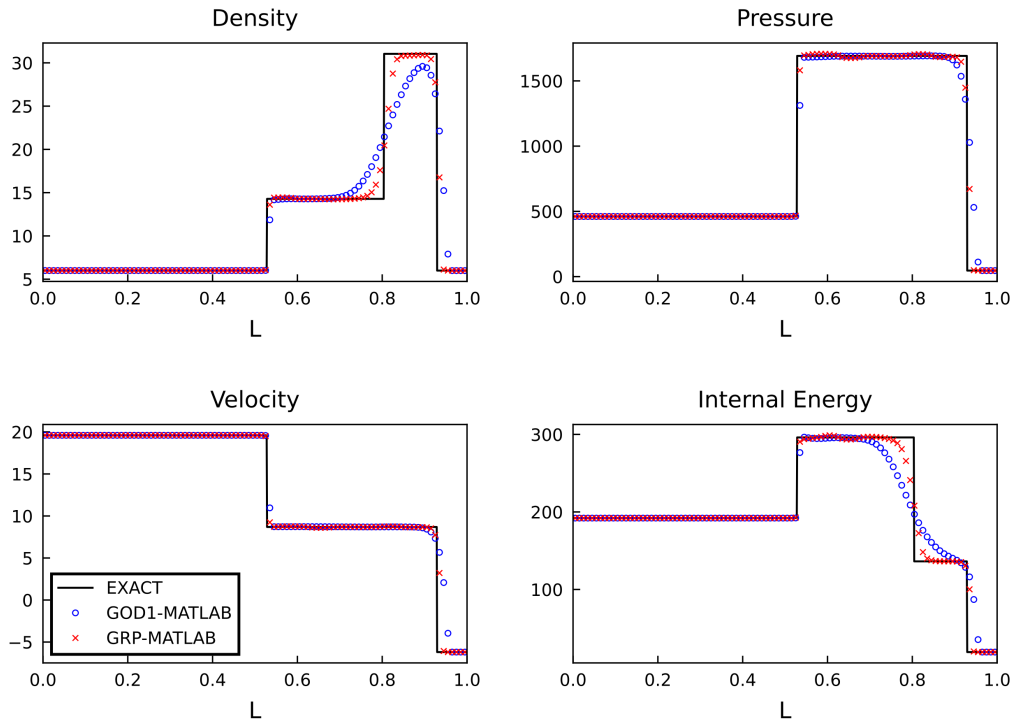

Figure 4.4: Results of Test Case 3

Figure 4.5: Results of Test Case 4

high-order schemes since variables change suddenly.

When compared with the Godunov scheme, the resolution of the shock wave is better in the GRP method, where the approximation took three cells. The shock wave is approximated over five cells with the first-order Godunov method.

Similar to Test Case 1, the performance at contact discontinuity is worse than shock wave, which results in less accurate post-shock values for the Godunov scheme, where it can be seen in the density or energy plot. Again, the GRP method has better results when the magnitude of the results is considered.

4.1.1.4   Test Case 4

In this test case, the accuracy and robustness of the numerical schemes are measured with three strong discontinuities. The initial discontinuity is located at $x_0 = 0.5$ in this case. This problem is obtained by the result of the collision of two strong shock waves moving in reverse directions. The results at $T = 0.035$ seconds are shown in Figure 4.5.
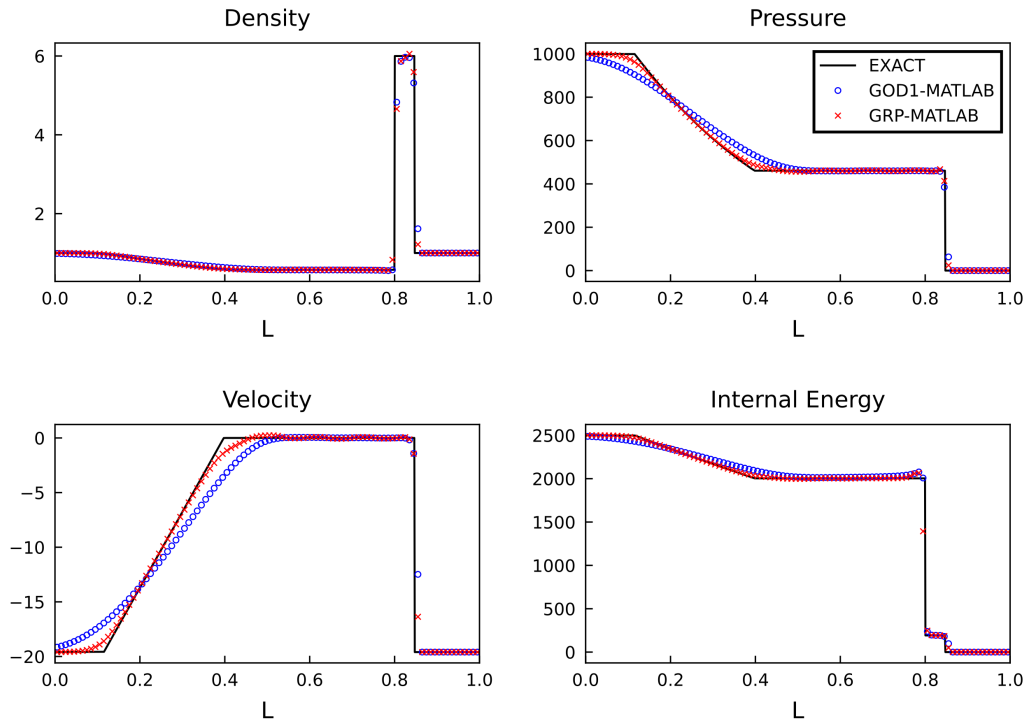
Figure 4.6: Results of Test Case 5

This problem involves two strong shock waves; one of them goes to the right, and the other one goes to the left direction with a very low shock speed. The right shock wave is approximated over five cells in the first-order Godunov scheme and two cells in the GRP method. The left, slow shock wave is sharply resolved in one cell by all of the schemes, but the internal energy plot shows that there are some low-frequency oscillations. The shock wave, which moves slowly, resolved successfully.

The contact discontinuity moves to the right in this problem, and the GRP method solves it better than the Godunov scheme, which can be seen from internal energy and density plots.

4.1.1.5 Test Case 5

The aim of this challenging test case is to evaluate the ability to solve slowly moving or stationary contact discontinuities in addition to evaluating the stability of numerical schemes. Location of initial discontinuity is at $x_0 = 0.8$. The results at $T = 0.012$ seconds are shown in Figure 4.6.

Test case 5 consists of a stationary contact discontinuity at $x = 0.8$, a left rarefaction wave (can be seen between $x \approx 0.1$ and $x \approx 0.4$), and a shock wave (can be seen at $x \approx 0.85$) that propagates to the right. The rarefaction wave is better resolved by the GRP scheme when results at the head and tail of the wave are considered.

The shock wave is approximated over one cell by all methods.

Since the contact discontinuity is stationary, it is resolved sharply by all methods, but an oscillatory behavior is observed in the energy plot behind this discontinuity.

4.1.2 Validation of Flow Solver Implementation

Two 1D shock tube problems are investigated in order to validate the implementation of the GRP method for the Euler equations in FLOWPSI. Also, the numerical results of the reference are used for comparison. In all cases, the computational domain is divided into $N = 100$ cells, where domain length L is taken as 1, and the ratio of specific heats is selected as $\gamma = 1.4$. In the figures, velocity, pressure, density, and internal energy variables are presented where exact results are shown by the black line; gray triangles indicate reference results, and blue crosses demonstrate solutions of the GRP method with generalized MINMOD limiter from FLOWPSI.

4.1.2.1 Test Case 1

This test case consists of a right shock wave, a left rarefaction wave, and contact discontinuity moving in the right direction. The gas is initially at rest. Initial discontinuity position has chosen as $x_0 = 0.5$. The results at $T = 0.15$ seconds are shown in Figure 4.7.

In all figures, the results are in near-perfect fit with the reference study. The resolution of the shock wave is captured by three cells.

It is challenging to resolve contact discontinuities; however, when compared, both of the solvers captured the discontinuity accordingly with reference. There is a small oscillatory behavior after contact discontinuity which is a result of the selected α_σ
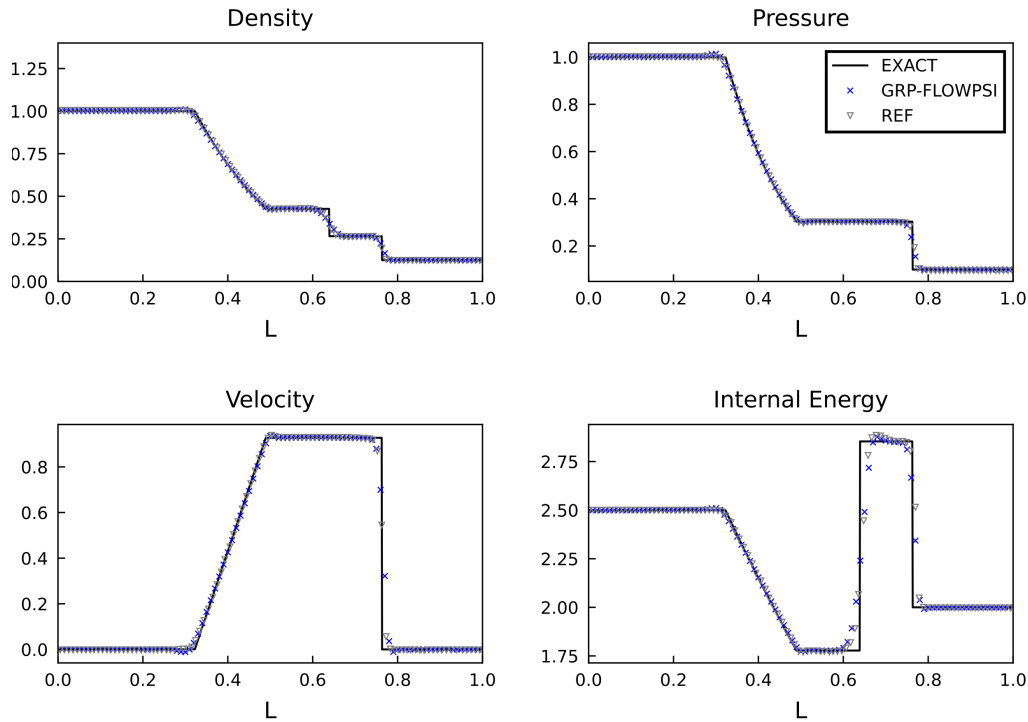
Figure 4.7: Results of Test Case 1

value of 1.9 of the limiter.

The rarefaction wave is resolved similarly in each solver and in good agreement with the reference solution.

4.1.2.2   Test Case 2

In this test case, a contact discontinuity at $x_0 = 0.5$ with zero speed separates the two symmetric rarefaction waves where the star region is close to the vacuum. The results at $T = 0.1$ seconds are shown in Figure 4.8.

The FLOWPSI results are in good agreement with the reference solution and exact results for ρ, u, p, and E. Since internal energy, e, charts disclose a lot about the quality of the numerical solution, when specific internal energy is examined, the result of FLOWPSI can be considered satisfactory. Density and pressure values get closer to zero towards $L = 0.5$, which results in growing differences in internal energy. The internal energy results are shown in Figure 4.9. The overshoots and undershoots in the solutions are observed near the head of both rarefaction waves, and this may be
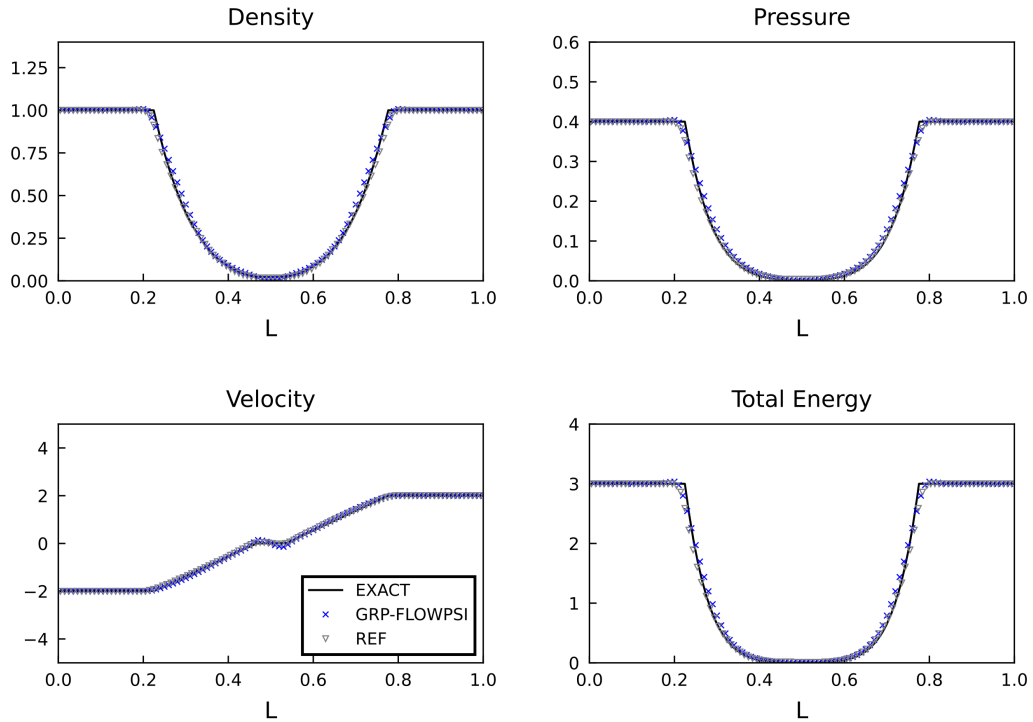
Figure 4.8: Results of Test Case 2

due to the α_σ value of 1.9 in the limiter.

4.2   Two-Dimensional Results

Four 2D cases are investigated to validate and show the performance of implemented GRP method in the two-dimensional domain. Moreover, results of second-order HLLC and Godunov schemes are also used for comparison. Barth-Jespersen limiter is used in all solutions to allow comparisons between different flux functions. The cases are selected from National Program for Applications-Oriented Research in CFD (NPARC) Alliance CFD Validation and Verification archive [63].

4.2.1   Inviscid Prandtl-Meyer Expansion

This inviscid, steady expansion-fan test case is selected to validate the two-dimensional expansion solution of the implemented algorithm and compare the results with Godunov and HLLC flux schemes. This test case is an isolated test to assess the model
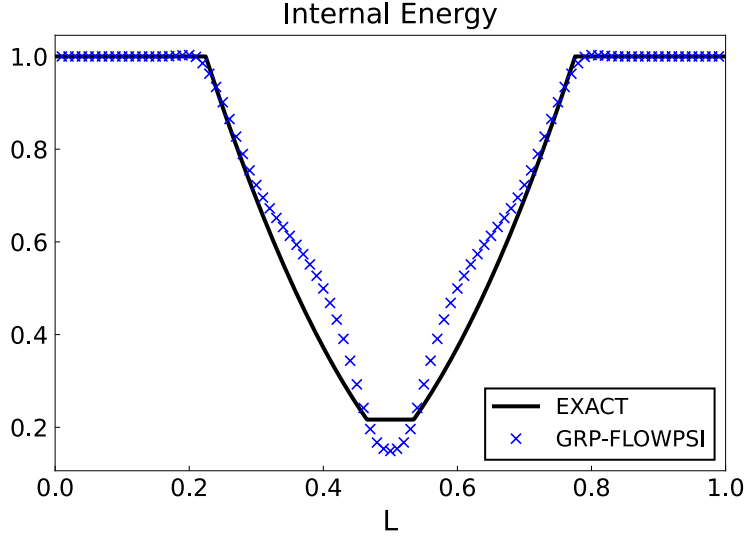
Figure 4.9: Internal Energy Results of Test Case 2

Table 4.3: The Inflow Boundary Conditions of the Solution Domain

	Mach Number	Pressure (Pa)	Temperature (K)
Inflow	2.5	82737.1	305.56

performance on an expansion fan. The domain and boundary types are given in Figure 4.10. The inflow boundary conditions of the problem can be found in Table 4.3.

In order to improve the resolution at the origin of expansion, a grid refinement study is conducted for this case. In this refinement study, the grid refinement factor $r = h_{coarse}/h_{fine}$ is selected as greater than 1.3, as advised in [64]. Three different grids are used, which are shown in Figure 4.11. The grid consists of unstructured tetrahedral cells. Around the expansion fan region, a denser grid is created.

The face and node counts of the grid are given in Table 4.4.

Table 4.4: Grid Information of the Prandtl-Meyer Expansion Case

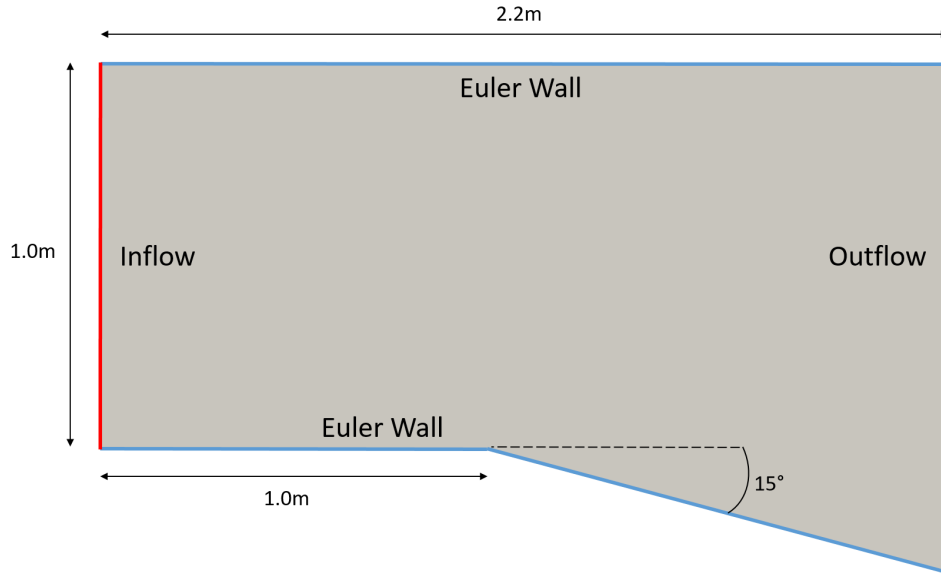|	Node Number	Face Number	r
Coarse Grid (a)	1548	2939	-
Middle Grid (b)	3509	6786	1.52
Fine Grid (c)	5651	11410	1.3

48

Figure 4.10: The Solution Domain and Boundary Types of Prandtl-Meyer Expansion Case

Table 4.5: Comparison of Prandtl-Meyer Expansion Case Results with Different Grids and Exact Solution

Var.	Unit	Exact	GRP-C	% Err.	GRP-M	% Err.	GRP-F	% Err.
M_2	-	3.2368	3.205	0.982	3.2269	0.306	3.2386	-0.056
P_2	Pa	27088	27082	0.022	27083	0.018	27092	-0.015
ρ_2	kg/m^3	0.425	0.419	1.412	0.423	0.471	0.426	-0.235
T_2	K	222.11	224.96	-1.283	222.85	-0.333	222.45	-0.153

The results of the grid refinement study done for the GRP method are presented in this section. As the grid becomes finer, the resolution at the origin of the expansion fan increases. Also, from the fine to the coarse grid, the increased diffusive characteristic of the fan can be observed. Different variables are presented in Figures 4.12 and 4.13; the Mach number contour of the solutions is given in Figures 4.14, 4.15, and 4.16. In all different grid solutions, the fan angle ν was found close to the theoretical value, $17°$; however, it becomes closer as the grid becomes finer. In Table 4.5, the results of the different grids in the region after expansion (denoted with subscript 2) are given.
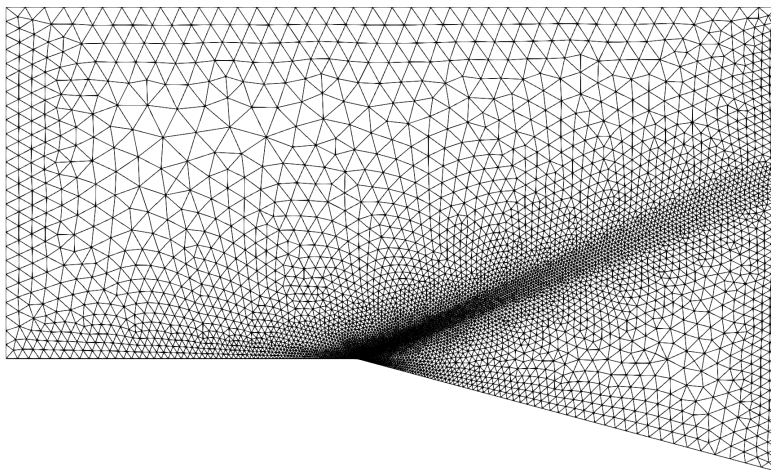
In addition to results obtained on the lower surface, the results at section A-A, which passes across the expansion fan, are also investigated and shown in Figure 4.17. The
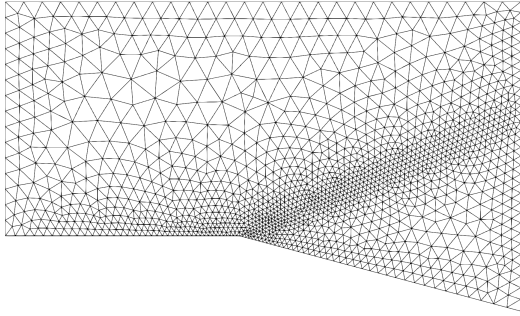
(a) Coarse Grid
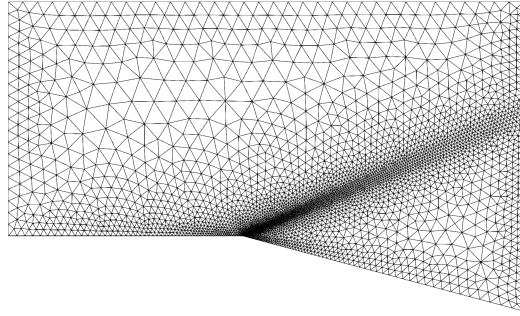
(b) Middle Grid

(c) Fine Grid

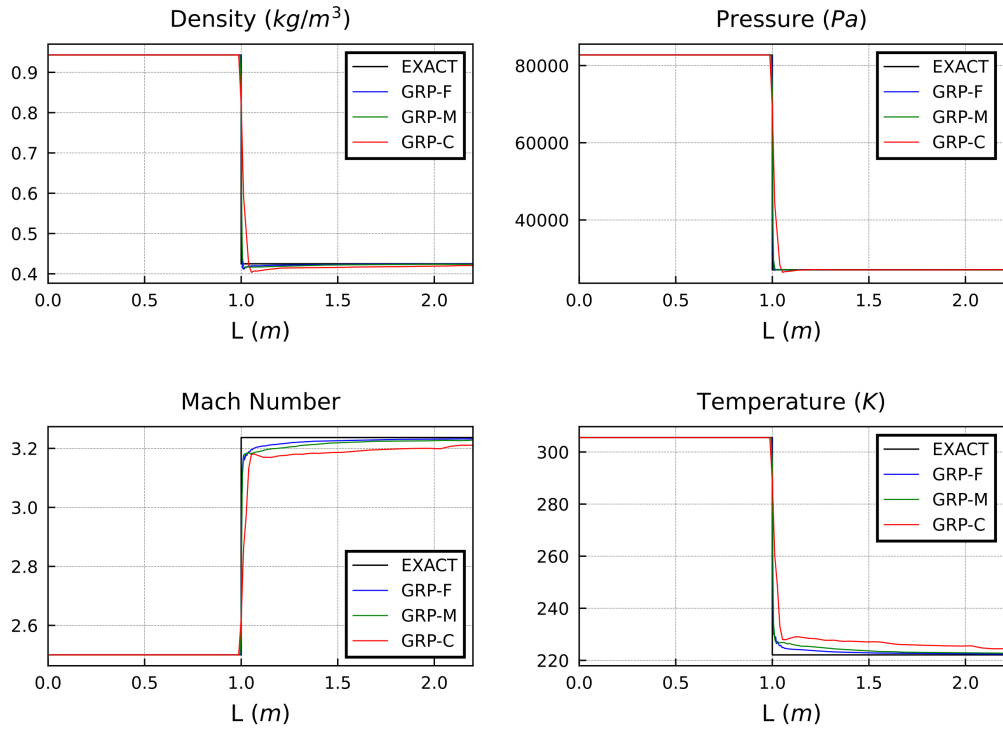Figure 4.11: Grids Used in Prandtl-Meyer Expansion Case

Figure 4.12: Density, Pressure, Mach Number, and Temperature Values of Prandtl-Meyer Expansion Case at Lower Wall of the Domain with Different Grids
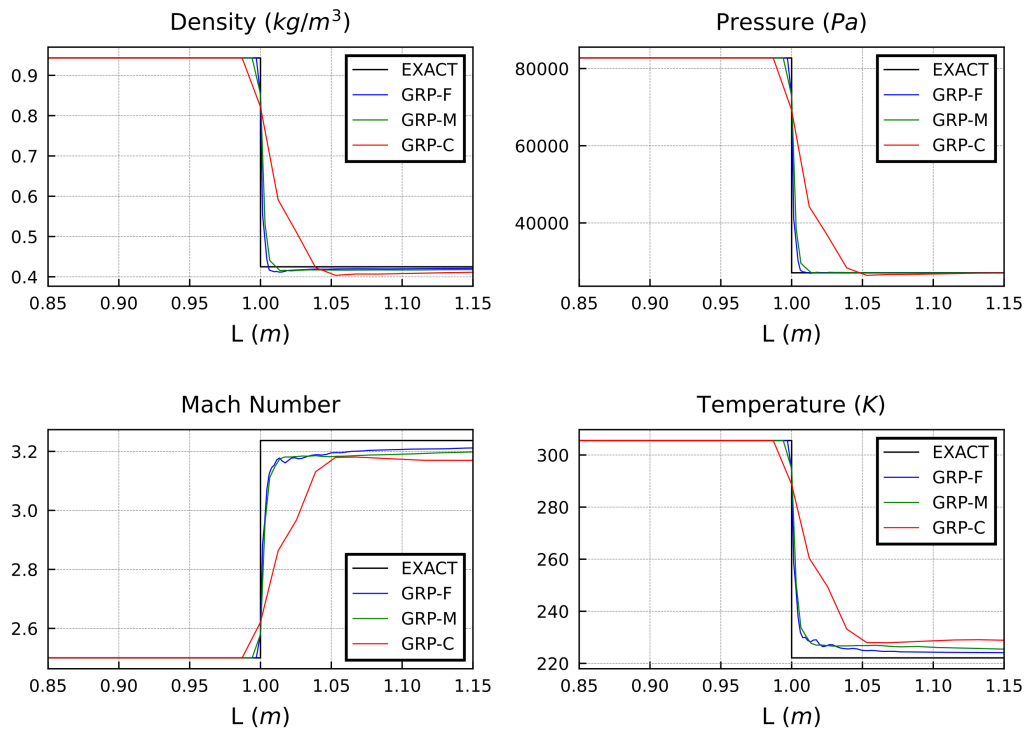

Figure 4.13: Density, Pressure, Mach Number, and Temperature Values of Prandtl-Meyer Expansion Case Near Discontinuity with Different Grids
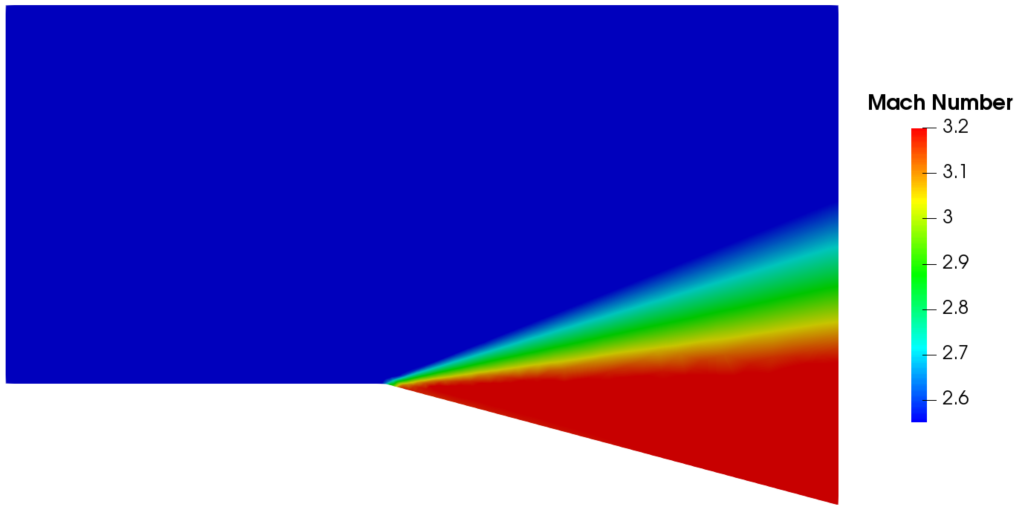
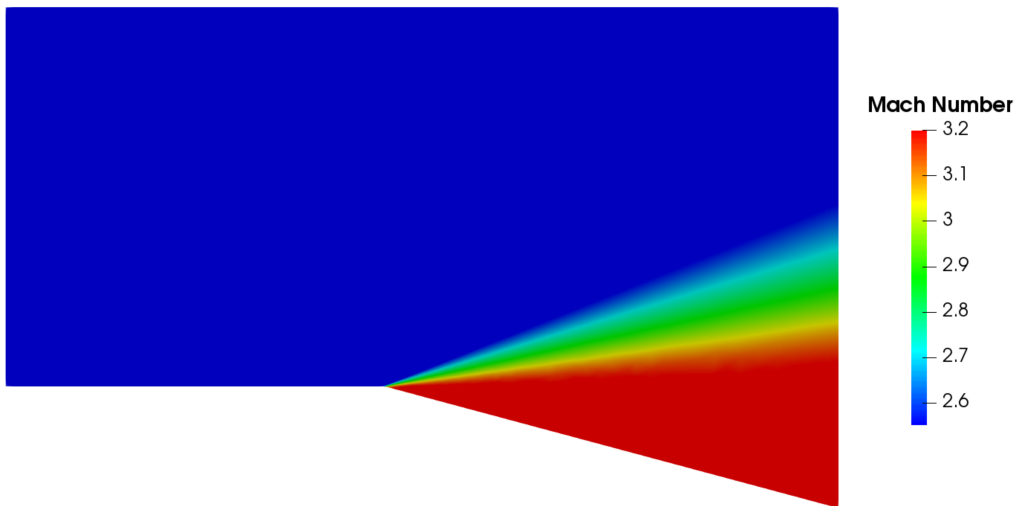Figure 4.14: Mach Number Contour of Prandtl-Meyer Expansion Case with Coarse Grid

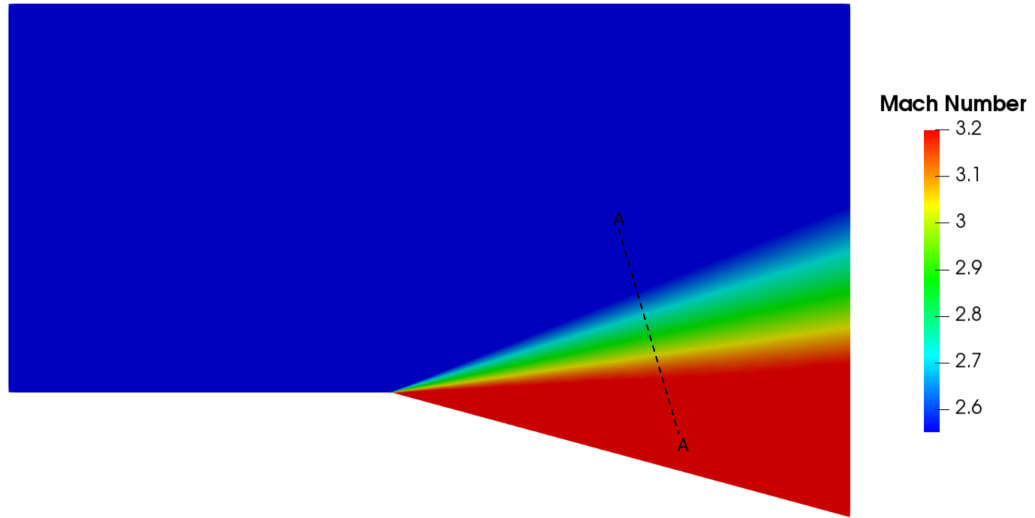Figure 4.15: Mach Number Contour of Prandtl-Meyer Expansion Case with Middle Grid

Figure 4.16: Mach Number Contour of Prandtl-Meyer Expansion Case with Fine Grid

Table 4.6: Comparison of Prandtl-Meyer Case Results with Different Flux Schemes and Exact Solution

Var.	Unit	Exact	GRP	% Err.	God.	% Err.	HLLC	% Err.
M_2	-	3.2368	3.2386	-0.056	3.2302	0.204	3.2286	0.253
P_2	Pa	27088	27092	-0.015	27084	0.015	27094	-0.022
ρ_2	kg/m^3	0.425	0.426	-0.235	0.424	0.235	0.423	0.471
T_2	K	222.11	222.45	-0.153	222.70	-0.266	222.84	-0.329

location of this section is given in Figure 4.16. The expansion fan resolved better as grid became denser.

The results obtained with different convective flux schemes, such as the second-order Godunov method, HLLC scheme, and the implemented method, GRP, for the "fine grid" are given in Figures 4.18 and 4.19. The GRP method shows better resolution near the discontinuity, and values obtained from the GRP method are closer to the exact solution. The results of the HLLC and the Godunov schemes are close to each other, but with the Godunov scheme, better approximations are obtained near the discontinuity. The results of the post-shock region (denoted with subscript 2) are given in Table 4.6.

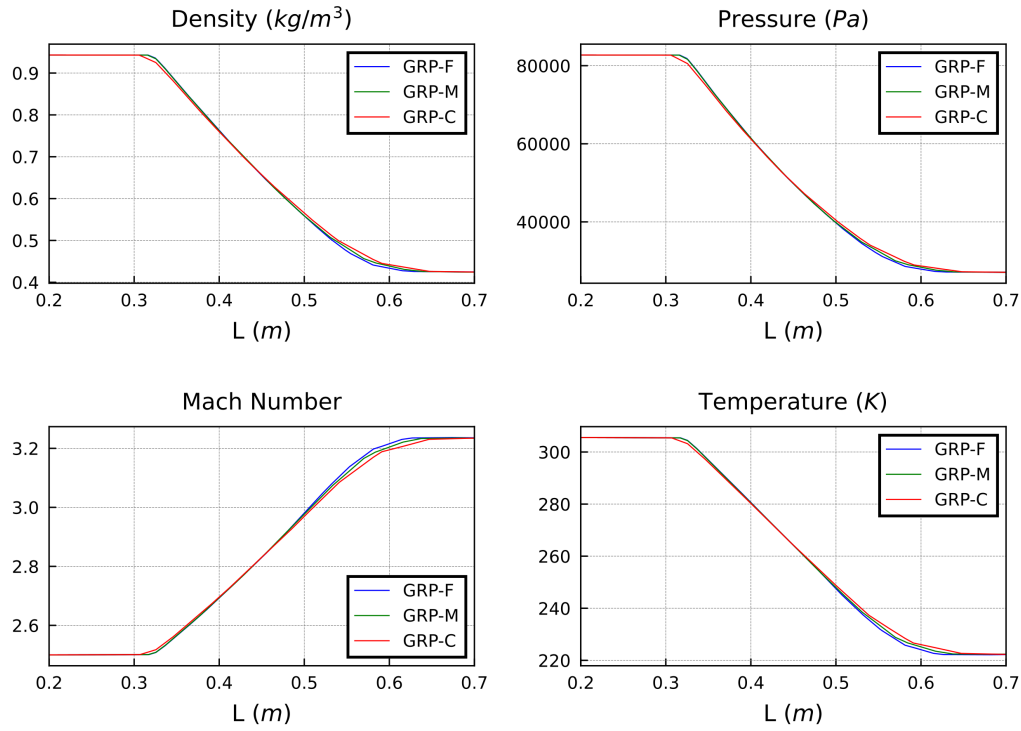The results at section A-A, which is perpendicular to the expansion fan, are also

Figure 4.17: Density, Pressure, Mach Number, and Temperature Values of Prandtl-Meyer Expansion Case at Section A-A with Different Grids
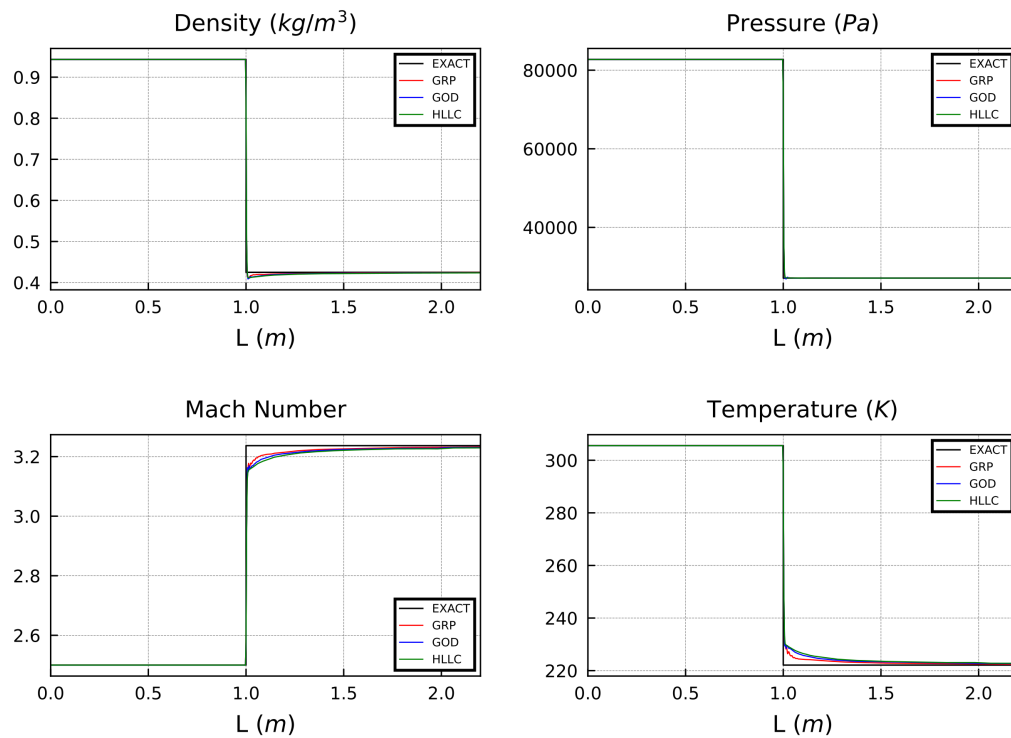

Figure 4.18: Density, Pressure, Mach Number, and Temperature Values of Prandtl-Meyer Expansion Case at Lower Wall of the Domain with Different Flux Schemes
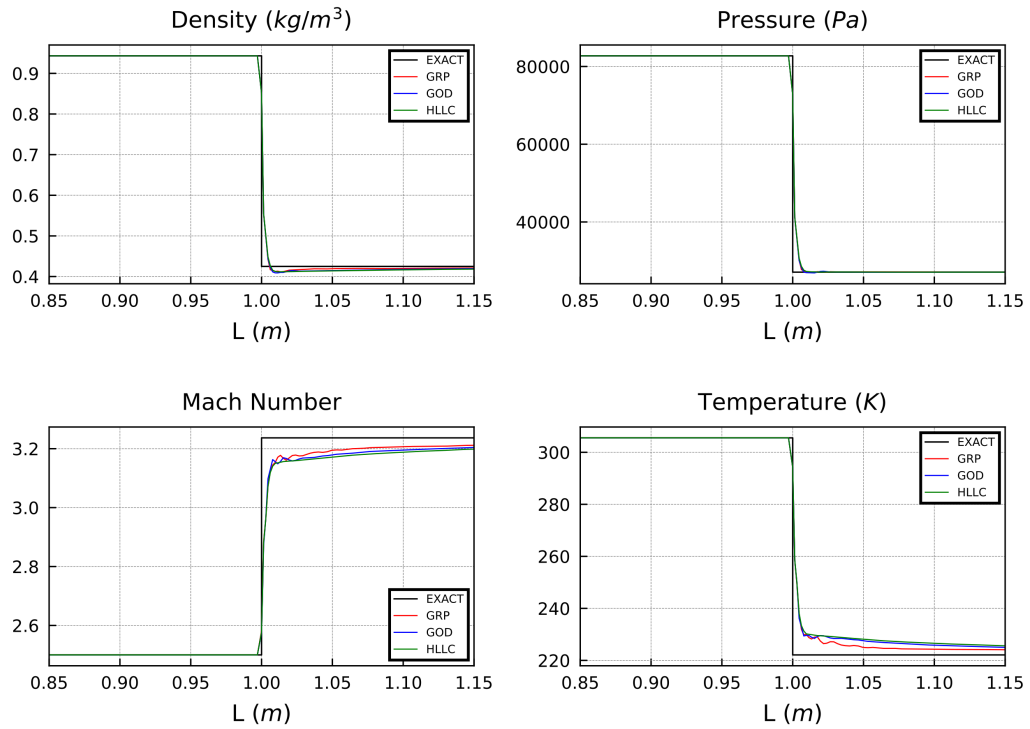
Figure 4.19: Density, Pressure, Mach Number, and Temperature Values of Prandtl-Meyer Expansion Case Near Discontinuity with Different Flux Schemes

investigated for different flux schemes and shown in Figure 4.20. The GRP method has better resolution across the expansion fan when compared with the HLLC and second-order Godunov schemes. The accuracy of the HLLC and Godunov methods is nearly the same.

4.2.2 The Inviscid Supersonic Wedge

This inviscid, steady case is selected in order to validate the two-dimensional shock-capturing ability of the GRP scheme and compare the results with Godunov and HLLC flux schemes. The domain and boundary types are given in Figure 4.21. An oblique shock wave forms as a result of a $10°$ wedge deflecting the flow. The inflow boundary conditions of the problem can be found in Table 4.7.

In order to obtain the theoretical shock angle and compare the solution with different types of grids, structured and unstructured (obtained from [65]) grids are investigated. To increase the resolution of the oblique shock wave and capture this in a smaller
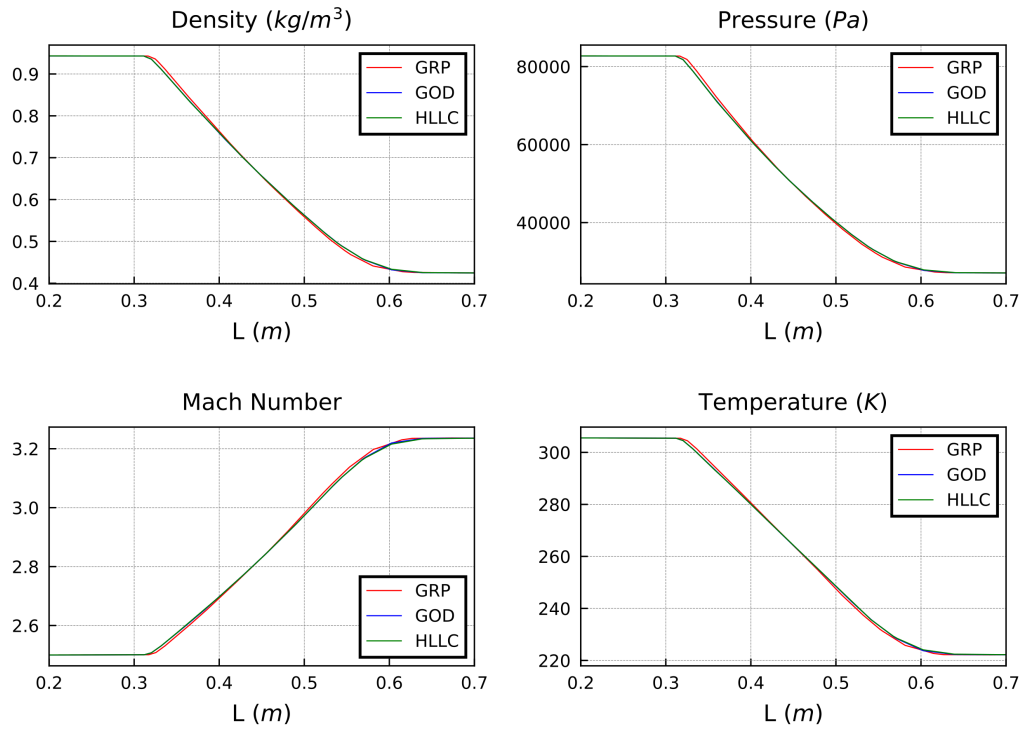
Figure 4.20: Density, Pressure, Mach Number, and Temperature Values of Prandtl-Meyer Expansion Case at Section A-A with Different Flux Schemes
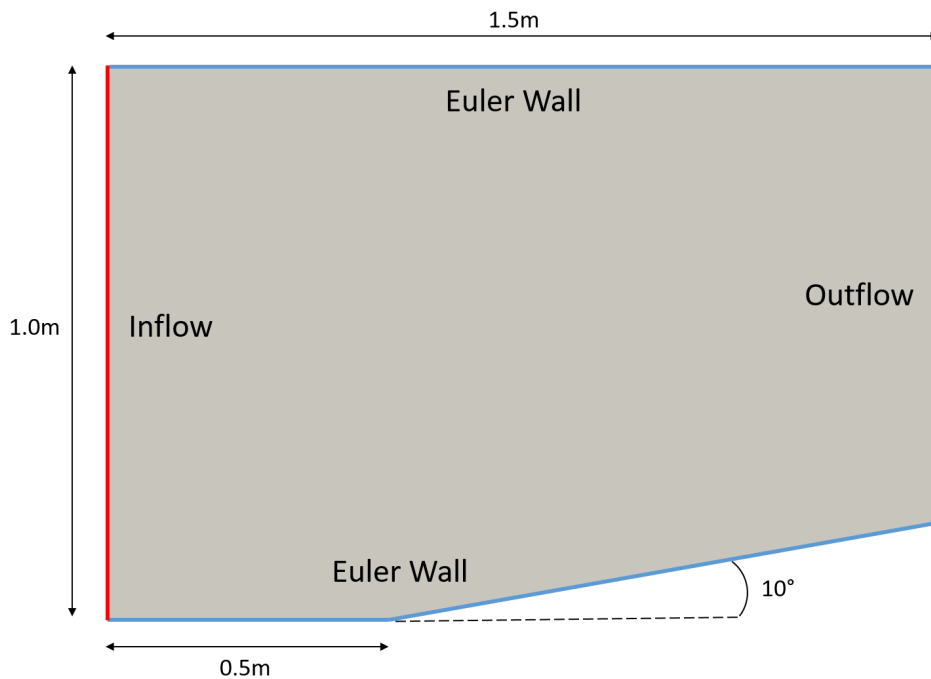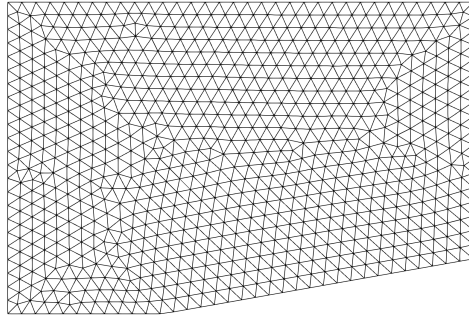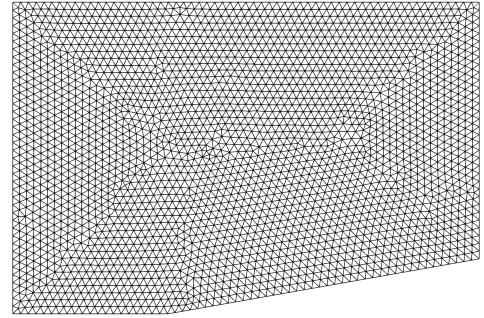

Figure 4.21: The Solution Domain and Boundary Types of Supersonic Inviscid Wedge Case

Table 4.7: The Inflow Boundary Conditions of the Solution Domain of Inviscid Wedge Case
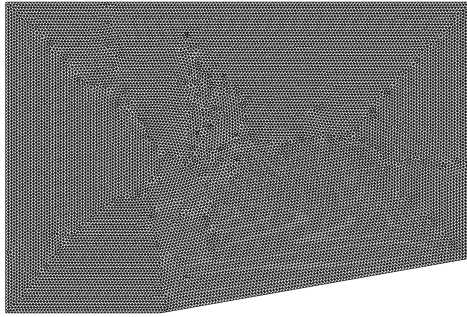
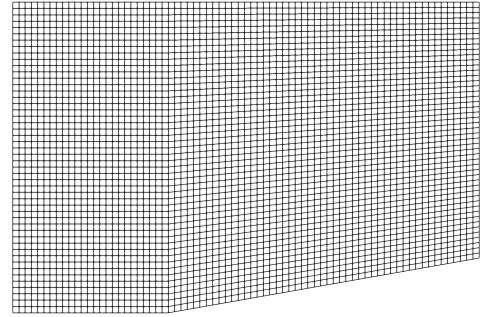|	Mach Number	Pressure (Pa)	Temperature (K)
Freestream	2.0	101325	300

(a) Coarse Grid

(b) Middle Grid

(c) Fine Grid

(d) Structured Grid

Figure 4.22: Grids Used in Inviscid Wedge Case

width, a grid refinement study is done for this case with a refinement factor greater than 1.3. Four different grids are used, which are shown in Figure 4.22.

The face and node numbers of the grid are given in Table 4.8.

A grid refinement study for the GRP method is done. As the grid becomes finer, the oblique shock is captured thinner. Also, from the fine to the coarse grid, the increased diffusive characteristic of the shock wave can be observed. In addition, the solution with a structured grid showed better resolution close to the discontinuity than the "middle grid" case, although the cell number of this case is higher. The values of different variables are given in Figures 4.23 and 4.24, Mach number contour

Table 4.8: Grid Information of Inviscid Wedge Case

	Node Number	Face Number	r
Coarse Grid (a)	847	1584	-
Middle Grid (b)	2662	5128	1.8
Fine Grid (c)	16113	31740	2.5
Structured Grid (d)	3750	3626	-

Table 4.9: Comparison of Inviscid Wedge Case Results with Different Unstructured Grids and Exact Solution

Var.	Unit	Exact	GRP-C	% Err.	GRP-M	% Err.	GRP-F	% Err.
M_2	-	1.641	1.640	0.061	1.640	0.061	1.640	0.061
P_2	Pa	172919	173055	-0.078	173033	-0.066	172999	-0.046
ρ_2	kg/m^3	1.716	1.717	-0.058	1.717	-0.058	1.716	0.000
T_2	K	351.05	351.11	-0.017	351.01	-0.011	351.06	-0.003

of the solutions is given in Figures 4.25, 4.26, 4.27, and 4.28. In all different grid solutions, the shock angle was found close to the theoretical value, $39°$, and shown in the pressure contour Figure 4.29.

In Tables 4.9 and 4.10, the results of the different grids in the post-shock region (denoted with subscript 2) are given.

The results obtained with different convective flux schemes, such as the second-order Godunov method, HLLC scheme, and the implemented method, GRP, for "fine grid"

Table 4.10: Comparison of Inviscid Wedge Case Results with Structured Grid and Exact Solution

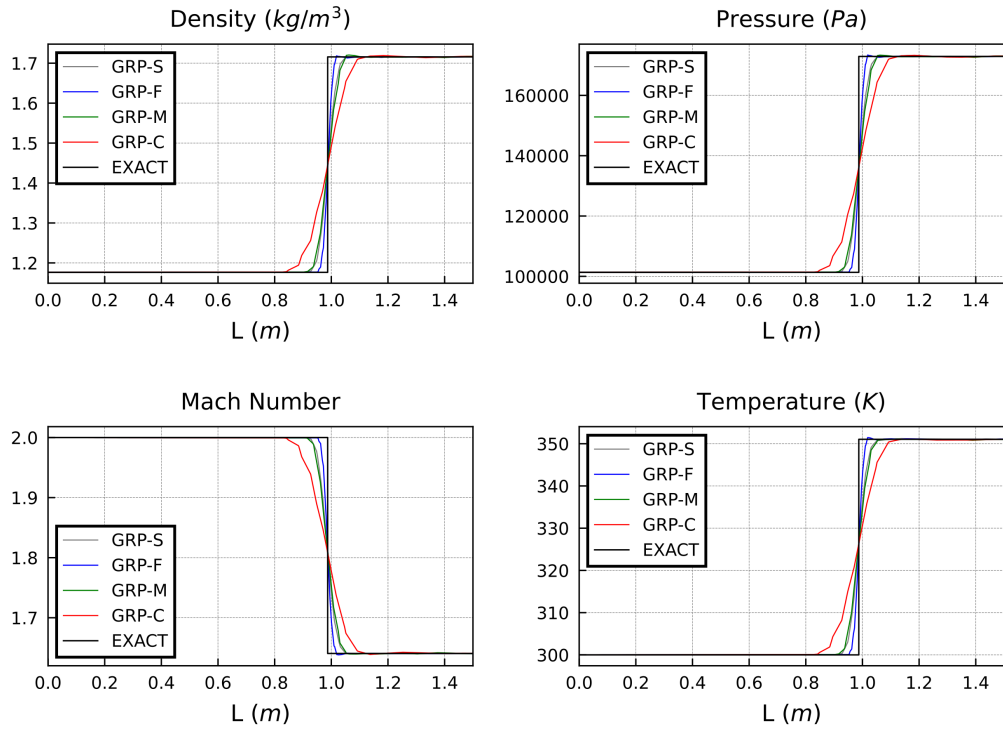| Var.	Unit	Exact	GRP-S	% Err.
M_2	-	1.641	1.640	0.061
P_2	Pa	172919	173027	-0.062
ρ_2	kg/m^3	1.716	1.717	-0.058
T_2	K	351.05	351.07	-0.006

Figure 4.23: Density, Pressure, Mach Number, and Temperature Values of Inviscid Wedge Case at $y = 0.4$ with Different Grids

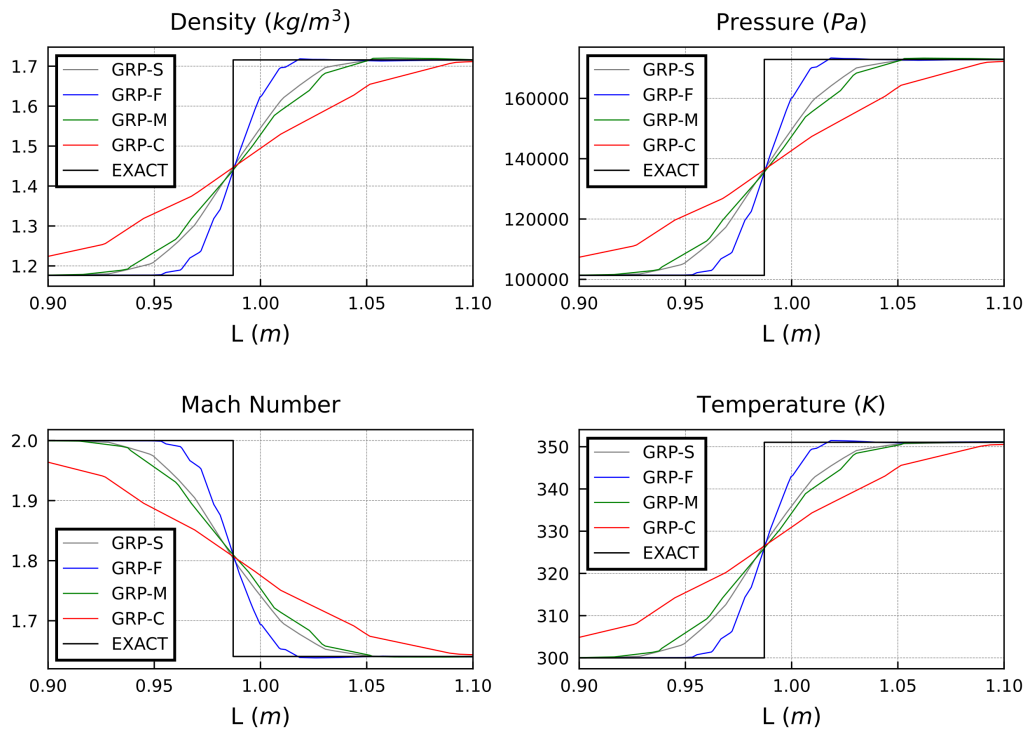Figure 4.24: Density, Pressure, Mach Number, and Temperature Values of Inviscid Wedge Case Near Discontinuity with Different Grids
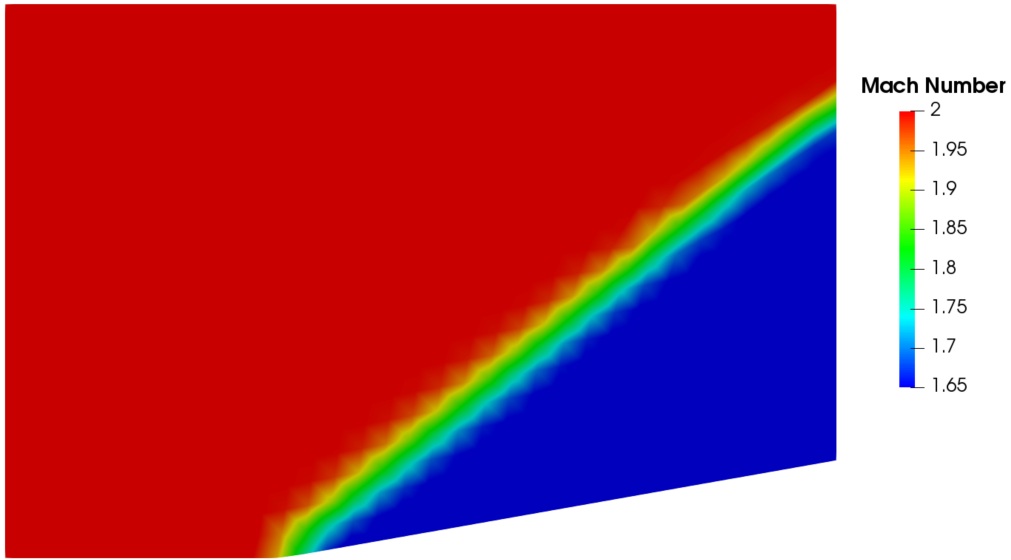
59

Figure 4.25: Mach Number Contour of Inviscid Wedge Case with Coarse Grid
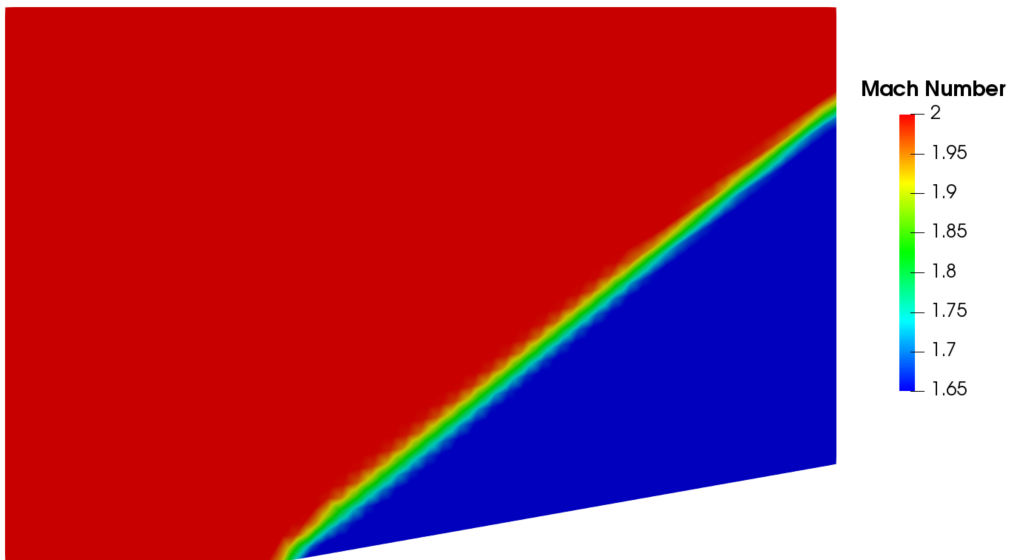

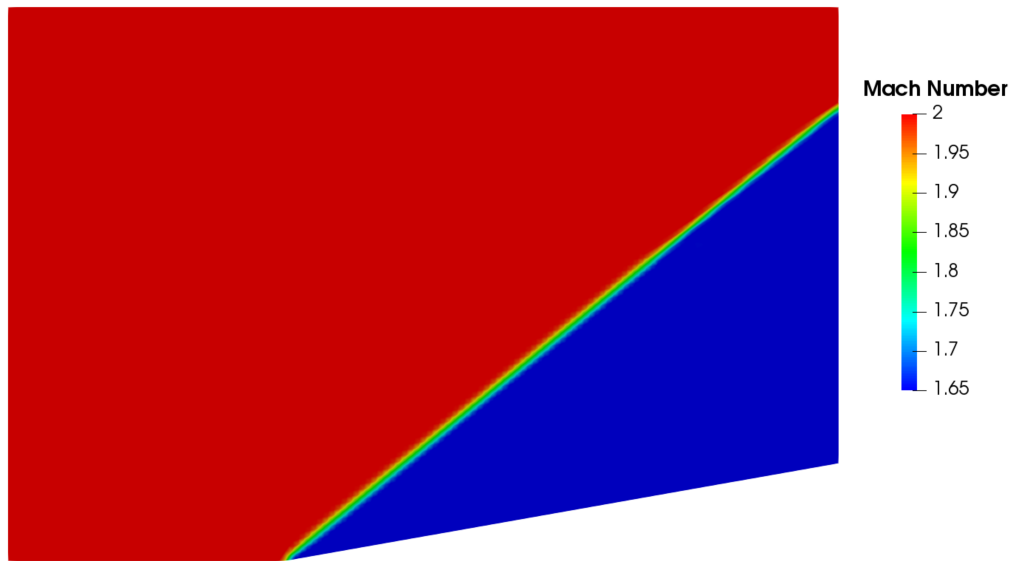Figure 4.26: Mach Number Contour of Inviscid Wedge with Middle Grid

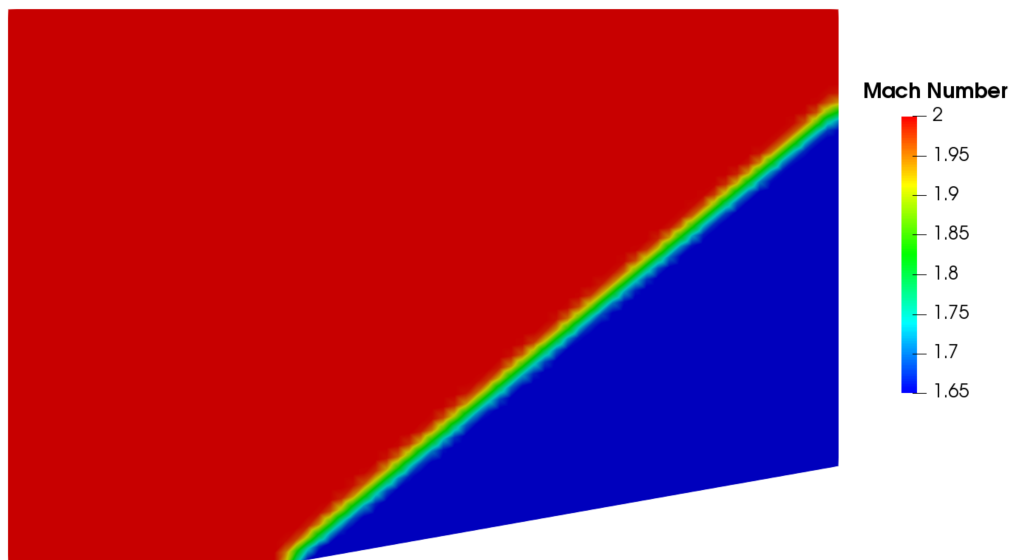Figure 4.27: Mach Number Contour of Inviscid Wedge with Fine Grid

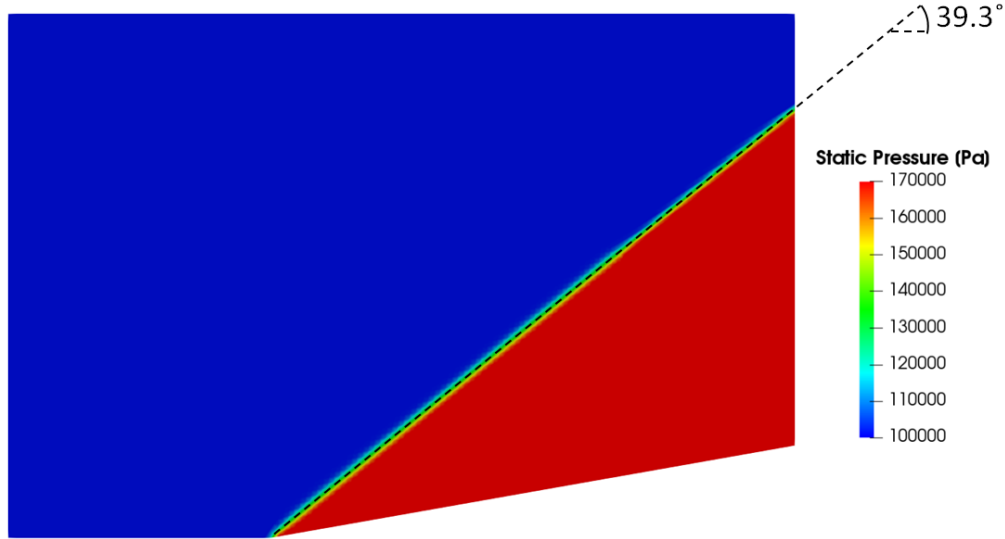Figure 4.28: Mach Number Contour of Inviscid Wedge with Structured Grid

Figure 4.29: Oblique Shock Angle and Pressure Contour of Inviscid Wedge

Table 4.11: Comparison of Inviscid Wedge Case Results with Different Flux Schemes and Exact Solution

Var.	Unit	Exact	GRP	% Err.	God.	% Err.	HLLC	% Err.
M_2	-	1.641	1.640	0.061	1.640	0.061	1.640	0.061
P_2	Pa	172919	172999	-0.046	172930	-0.006	172896	0.013
ρ_2	kg/m^3	1.716	1.716	0	1.715	0.058	1.715	0.058
T_2	K	351.05	351.06	-0.003	351.10	-0.014	351.02	0.009

are given in Figures 4.30 and 4.31. The GRP method shows slightly better resolution near the discontinuity, and values obtained from the GRP method are closer to the exact solution. The results of the HLLC and Godunov schemes are very close to each other. The results of the post-shock region (denoted with subscript 2) are given in Table 4.11.

4.2.3   RAE 2822 Transonic Airfoil Case

In this case, a transonic flow around a non-symmetric airfoil, RAE 2822, is solved with the $k - \omega$ SST turbulence model to study the performance of implemented GRP method in viscous flows and in the transonic flow regime. The grid, which consists of 38492 cells, and 25 layers of boundary mesh with the first height of $3.048 \times 10^{-6} m$ (to
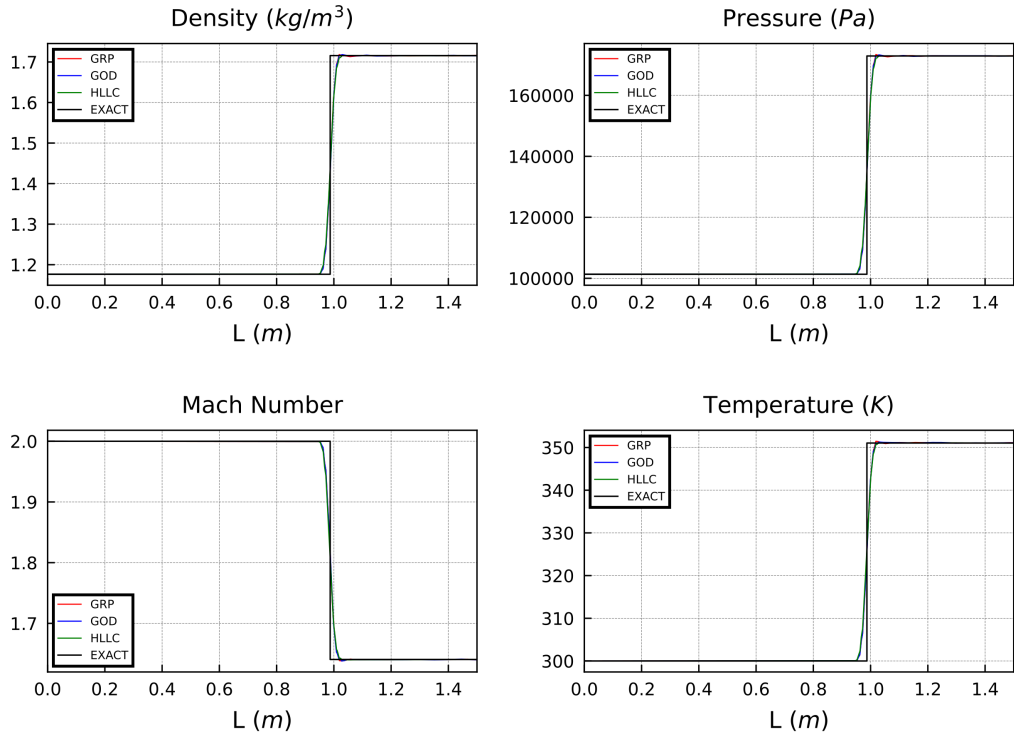
Figure 4.30: Density, Pressure, Mach Number, and Temperature Values of Inviscid Wedge at $y = 0.4$ with Different Flux Schemes
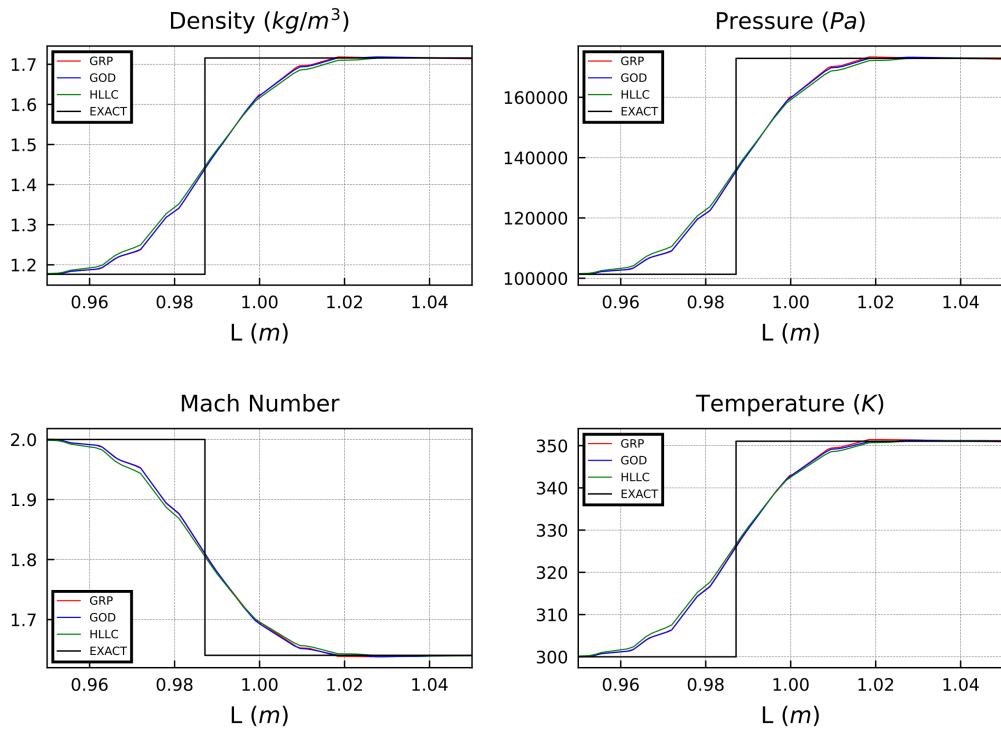

Figure 4.31: Density, Pressure, Mach Number, and Temperature Values of Inviscid Wedge Near Discontinuity with Different Flux Schemes
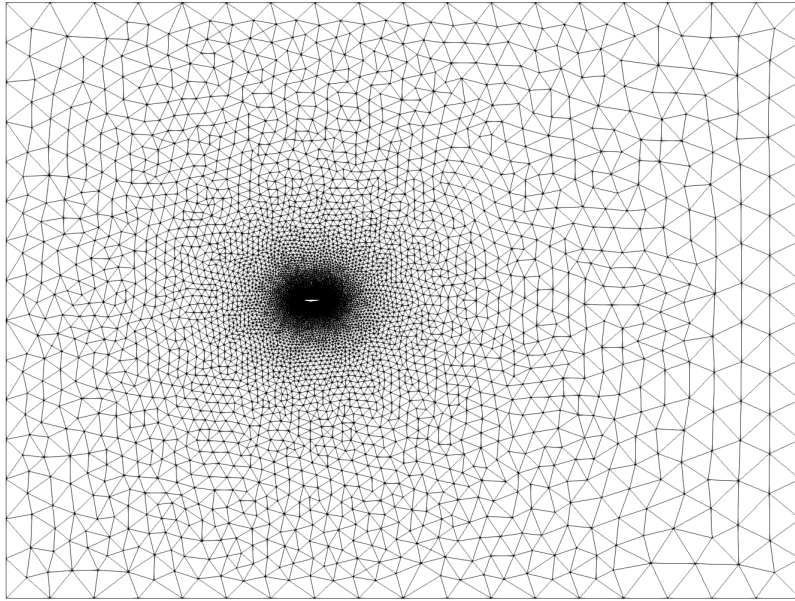
Figure 4.32: The Solution Domain of RAE 2822 Airfoil

Table 4.12: The Freestream Conditions of the Solution Domain of RAE 2822 Airfoil

	Mach Number	AoA (Degree)	Reynolds Number
Freestream	0.729	2.31	6.5×10^6

ensure that y^+ was smaller than 1), is given in Figures 4.32 and 4.33. The geometry of the airfoil is taken from [66]. The Freestream conditions of the problem can be found in Table 4.12.

The results obtained from the CFD solution were compared with experimental data [67] and results from the NPARC code [68]. The simulation with NPARC was performed with a structured C-grid and using the HLLC scheme and SST turbulence model. Note that the grid utilized in NPARC code is significantly higher quality than our grid. The comparison of C_p distribution of RAE 2822 transonic airfoil along the chord is given in Figure 4.34.

The results of the NPARC code and the GRP method are close to each other on the pressure side and suction side of the airfoil. There is a small difference at the peaks of suction in the leading edge between the two numerical results. The GRP method captured the shock wave sharply and the shock location closer to the experimental
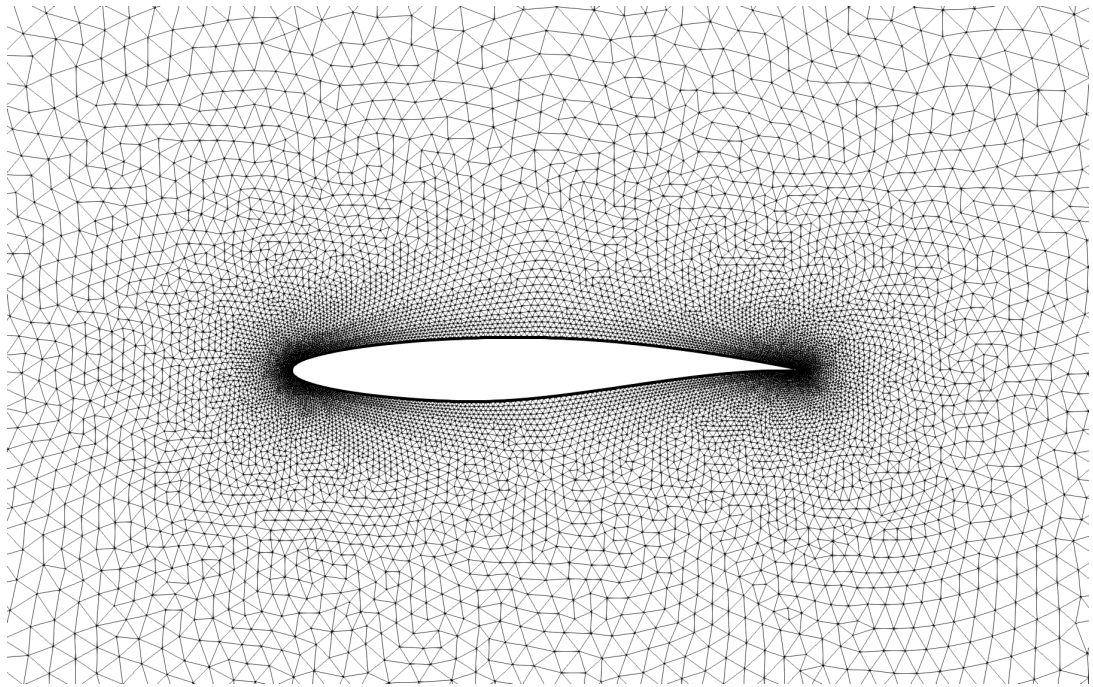
(a) Closer View of the Grid Near RAE 2822 Airfoil
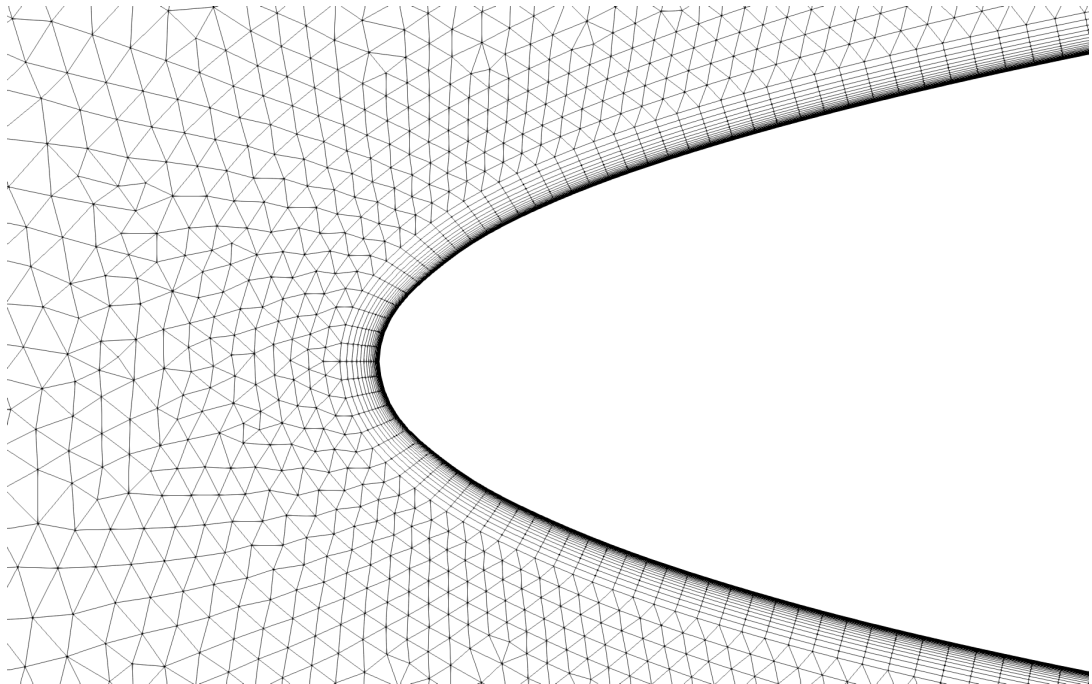
(b) Grid with Boundary Layer Mesh Closer to the Leading Edge of RAE 2822 Airfoil

Figure 4.33: The Grid Used in RAE 2822 Airfoil
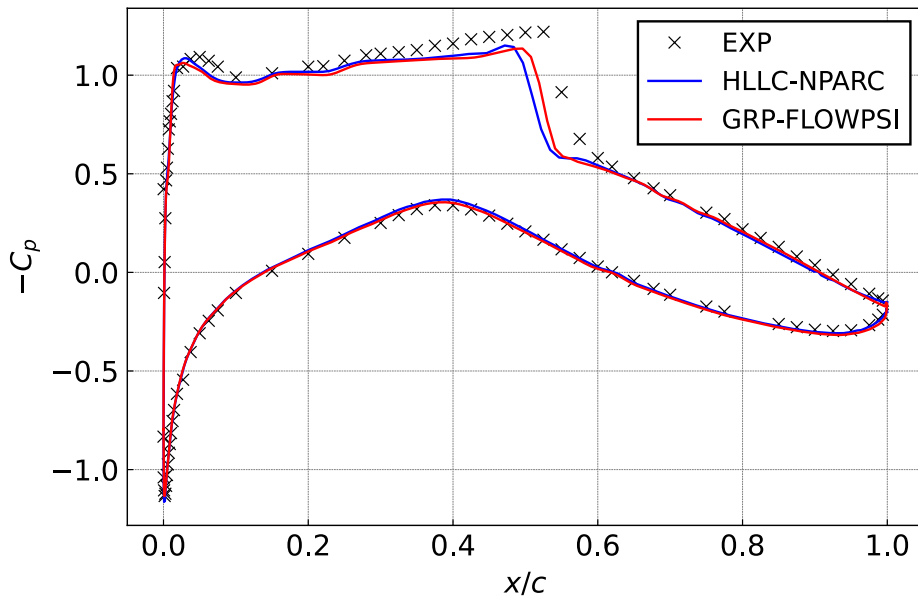
Figure 4.34: Pressure Coefficient Distribution of the RAE 2822 Airfoil

data when compared with the NPARC code. As can be seen from Figure 4.34, for the GRP method, the peaks of suction in the leading edge are well predicted. Except for the shock wave region, the pressure coefficient distribution is in very good agreement with the experimental data. The pressure distribution at the upper surface is underestimated close to the shock region, and although it is captured sharply, the location of the shock wave is not exactly found. The possible reasons for that are:

- the fact that the CAD geometry was not completely similar to the geometry used in the experiment,

- the selected turbulence model.

Computed lift and drag coefficients from the GRP method and experimental data are given in Table 4.13. The percent error of the results is below 7%. The pressure and Mach number contours from the solution from the GRP method are given in Figures 4.35 and 4.36.

Table 4.13: Lift and Drag Coefficient Comparison of RAE 2822 Airfoil

Variable	Exp.	GRP	%Error
C_l	0.7430	0.6911	6.989
C_d	0.0127	0.0129	-1.482
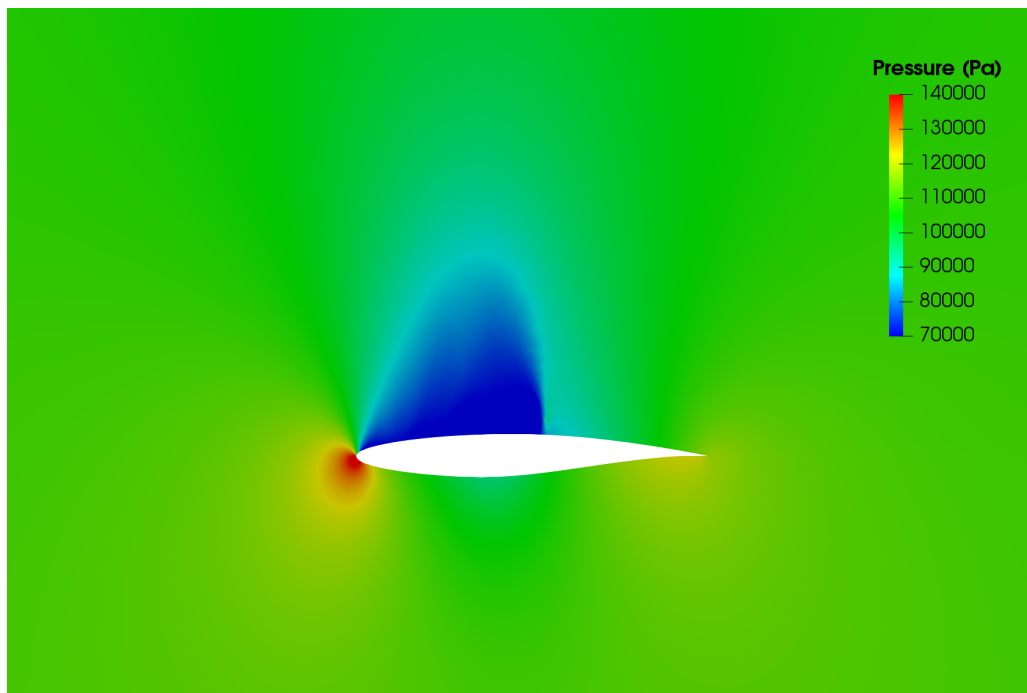
Figure 4.35: Pressure Contour of RAE 2822 Airfoil
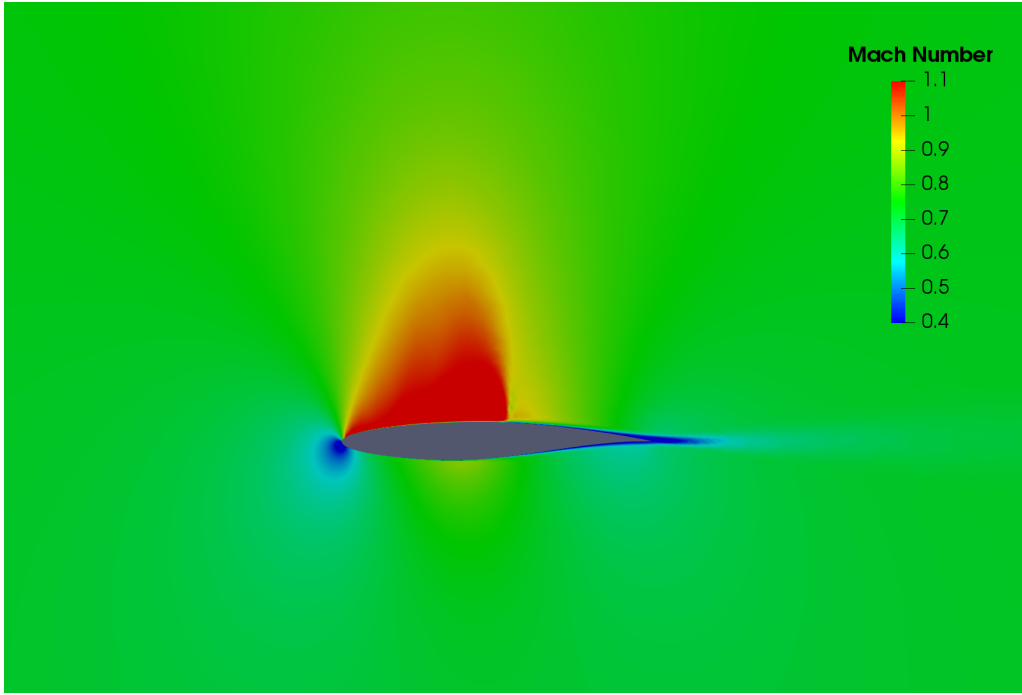
Figure 4.36: Mach Number Contour of RAE 2822 Airfoil

Table 4.14: The Freestream Conditions of the Solution Domain of ONERA M6 Wing
Case

	Mach Number	AoA (Degree)	Reynolds Number
Freestream	0.84	3.06	14.6×10^6

4.3 Three-Dimensional Results

4.3.1 ONERA M6 Transonic Wing Case

The ONERA M6 wing is selected in order to show the performance of the implemented method in the three-dimensional domain and in a challenging aerodynamic condition. This wing was designed in 1972 at ONERA to serve as experimental support in studies of CFD validations. An inviscid investigation of the problem is conducted with the following Freestream conditions given in Table 4.14. The CAD geometry of the wing is obtained from [69], and experimental results are taken from [70].

The layout of the ONERA M6 wing planform is given in Figure 4.37. The rows of
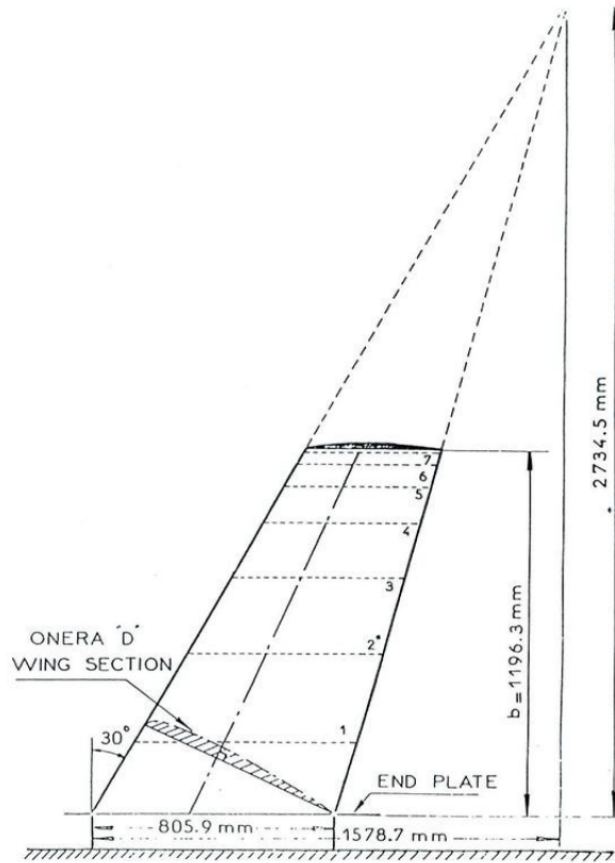
Figure 4.37: The Layout of the ONERA M6 Wing [70]

pressure taps that are located at the experiments are numbered from 1 to 7, which also can be seen in the figure.

The grid, which consists of ≈ 1.2 million tetrahedral cells, the upper surface grid of the wing, and the grid of the symmetry plane are given in Figure 4.38.

Before proceeding to the pressure coefficient results of the wing surface, it is more convenient to introduce the Mach number and pressure contours of the upper surface of the wing in order to understand the flow characteristics on the wing better. A lambda-type shock wave on the upper surface of the wing is formed from two shock waves that merge each other close to the tip of the wing and can be seen in Figure 4.39. In order to capture shock waves sharply, a grid adaption near the shock contours will provide better shock resolution.

With the implemented GRP method, the C_p distributions along the pressure and suc-
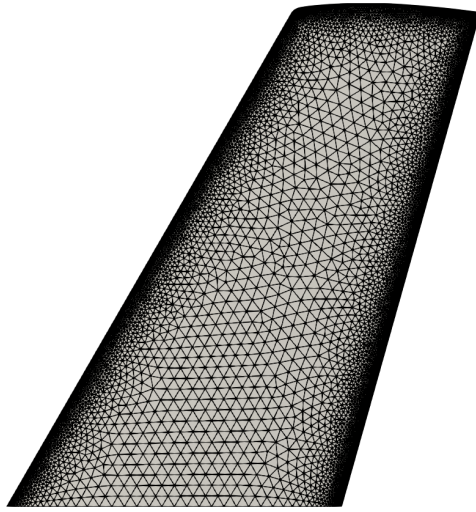
(a) Surface Grid of the Onera M6 Wing
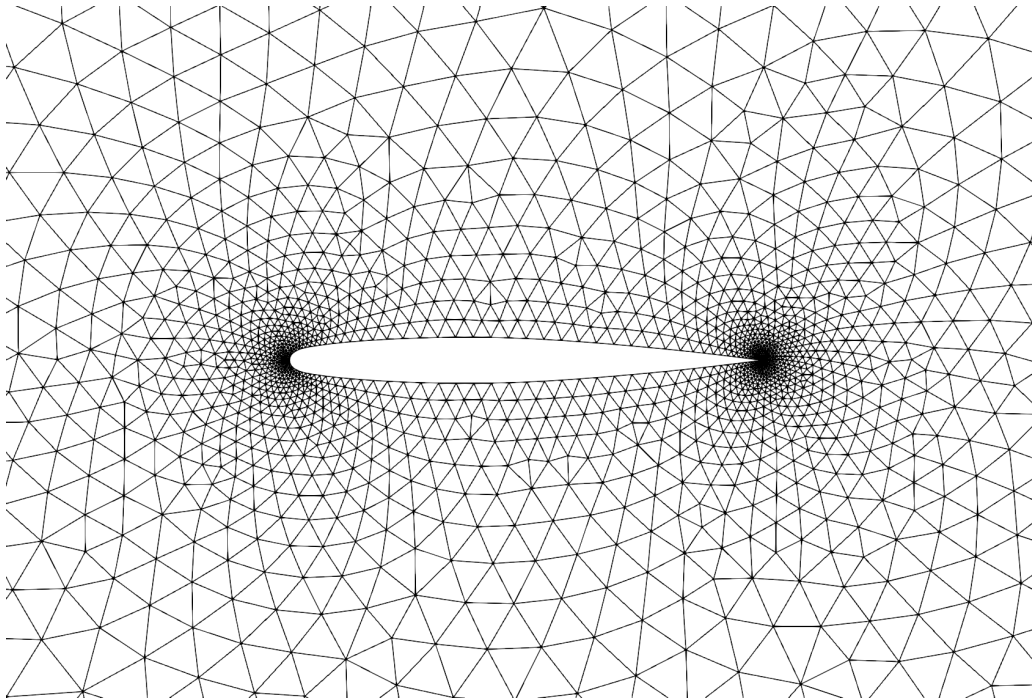
(b) Grids of the Symmetry Plane of ONERA M6 Wing

Figure 4.38: Grids of the ONERA M6 Wing Case at Different Surfaces
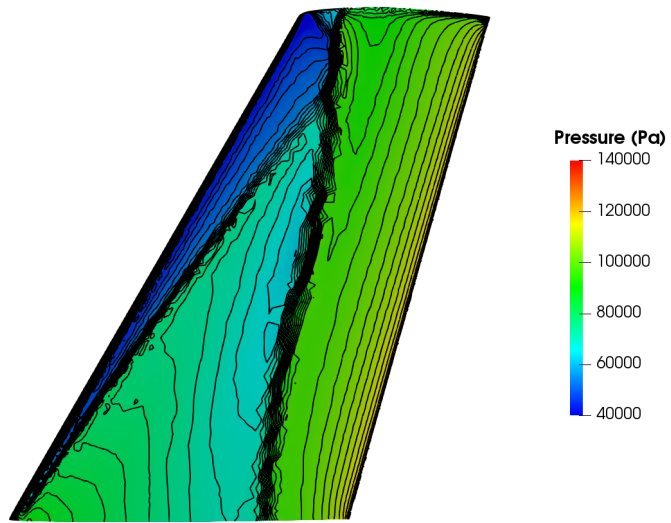
(a) Upper Surface Pressure Contour of ONERA M6 Wing
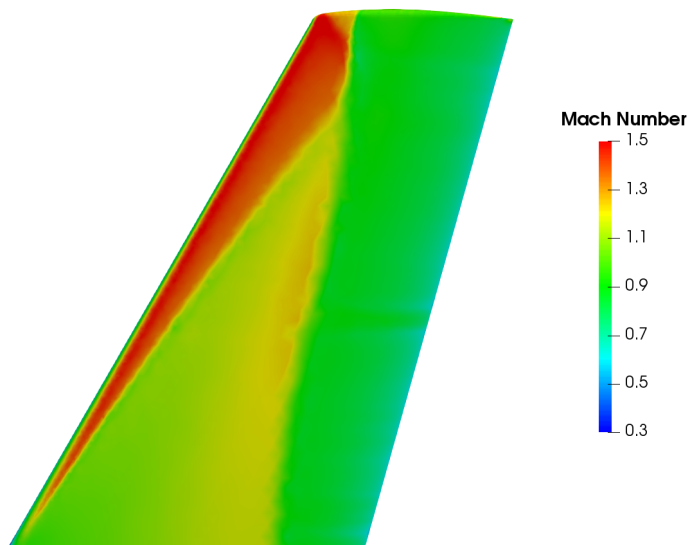
(b) Upper Surface Mach Number Contour of ONERA M6 Wing

Figure 4.39: Pressure and Mach Number Contour of Upper Surface of the ONERA M6 Wing
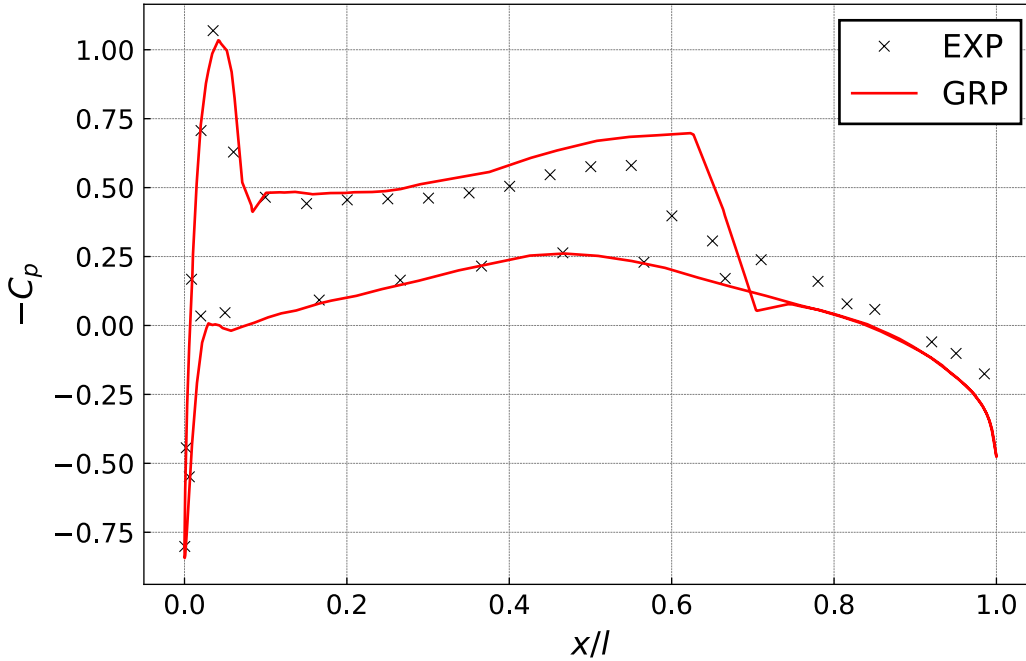
Figure 4.40: C_p Distribution at Section 1 of ONERA M6 Wing

tion sides of the wing in different sections are obtained. The results are compared with the experimental data. In Figure 4.40, the pressure coefficient distribution at section 1 is investigated, where there are two shock waves along this section. The suction peaks close to the leading edge are well predicted. The first shock wave is captured sharply. Although the second wave is captured sharply, it is predicted stronger than the experimental shock wave. As is typical for the inviscid methods for this case, the location of the second shock wave is predicted a little downstream of the location of the experimental shock wave [71]. The suction side pressure coefficients were predicted precisely.

In Figure 4.41, the C_p distribution at section 3 is examined where the two shock locations began to combine. The first shock wave is not captured as sharp as the second one. The reason may be the coarse mesh around the center of the wing. Similar to the results of section 2, the suction peaks close to the leading edge are predicted accurately. The suction side pressure coefficients fit well with the experimental data.

In Figure 4.42, the C_p distribution at section 5 is investigated where the two shock

72
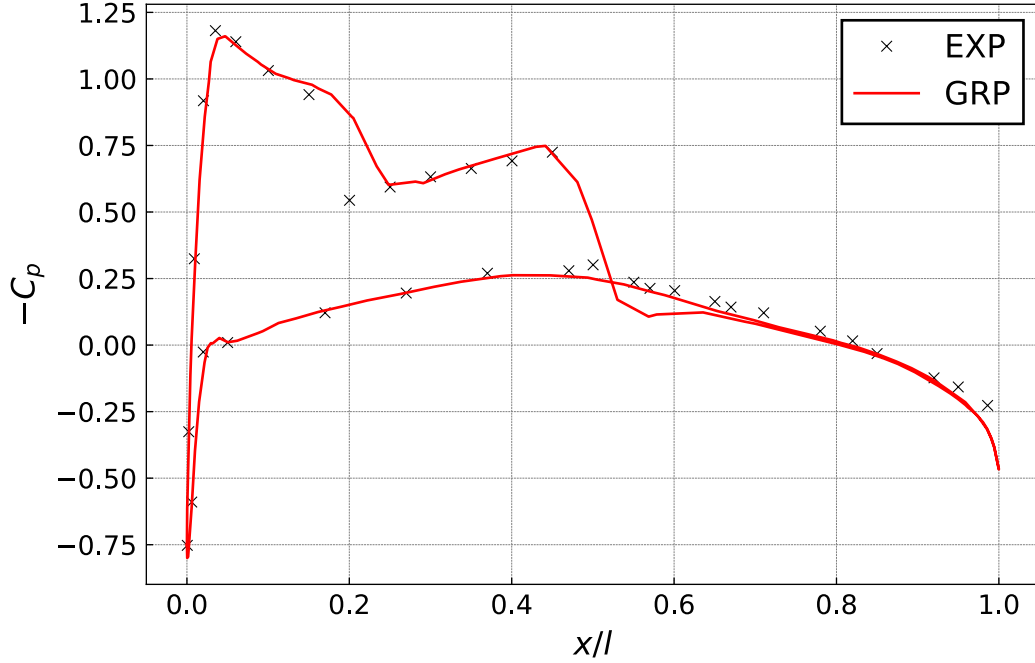
Figure 4.41: C_p Distribution at Section 3 of ONERA M6 Wing

waves are merged, which results in a relatively stronger shock wave. The shock wave was captured sharply. Similar to the results of section 1 and section 3, the suction peaks nearly to the leading edge are well predicted; furthermore, the suction side pressure coefficients are in good agreement with experimental results.

4.4 Critical Assessment of Second-order Schemes

After the assessment of two-dimensional and three-dimensional cases for the GRP method, the results obtained did not show a noticeable difference from other second-order schemes, contrary to our expectations. In order to assess this issue in detail, 1D cases are solved again with a limiter modification. Since a modified generalized MINMOD limiter is used in the GRP method, similarly, the generalized MINMOD limiter of van Leer [20] is implemented accordingly for the second-order Godunov method with removing the time derivative solution of the GRP method, $\left(\frac{\partial U}{\partial t}\right)$, from the limiter. It is observed that the effect of $\Delta t \left(\frac{\partial U}{\partial t}\right)_{i+\frac{1}{2}}^{n}$ component in the GRP method is less than 0.1%. Equation (4.1) demonstrates the **modified** generalized MINMOD

73
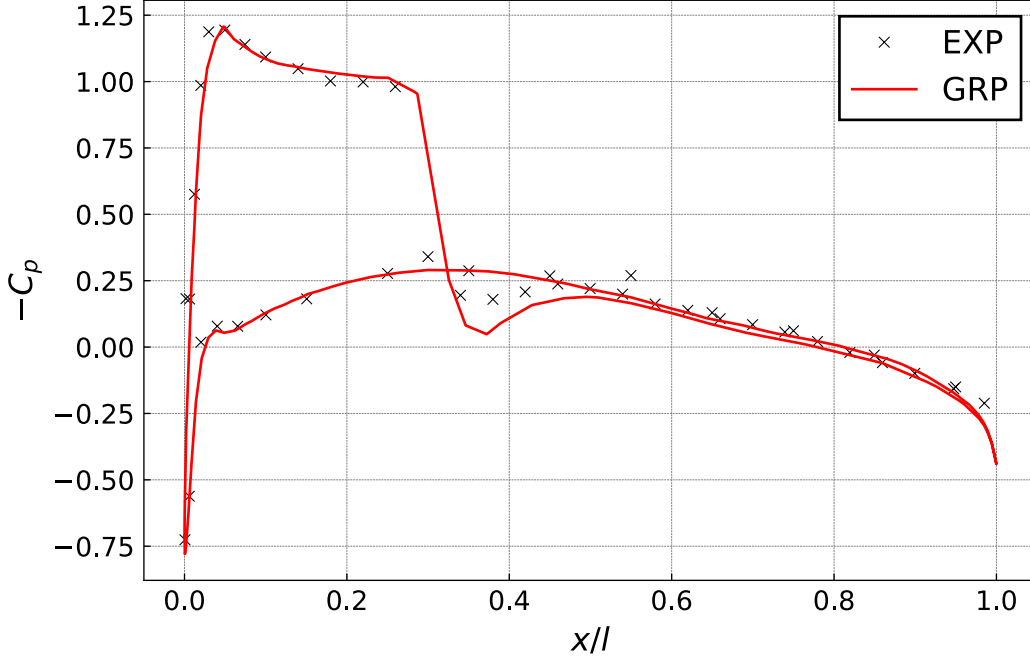
Figure 4.42: C_p Distribution at Section 5 of ONERA M6 Wing

limiter used in the GRP method. Equation (4.2) demonstrates the generalized MIN-MOD limiter used in the second-order Godunov method.

$$
\left.\begin{aligned}
U_{i+\frac{1}{2}}^{n+1,-} &= U_{i+\frac{1}{2}}^{n} + \Delta t \left(\frac{\partial U}{\partial t}\right)_{i+\frac{1}{2}}^{n} \\
\sigma_i^{n+1,-} &= \frac{1}{\Delta x}\left(U_{i+\frac{1}{2}}^{n+1,-} - U_{i-\frac{1}{2}}^{n+1,-}\right) \\
\sigma_i^{n+1} &= minmod\left(\alpha_\sigma \frac{U_i^{n+1}-U_{i-1}^{n+1}}{\Delta x}, \sigma_i^{n+1,-}, \alpha_\sigma \frac{U_{i+1}^{n+1}-U_i^{n+1}}{\Delta x}\right)
\end{aligned}\right\}
\tag{4.1}
$$

$$
\left.\begin{aligned}
U_{i+\frac{1}{2}}^{n+1,-} &= U_{i+\frac{1}{2}}^{n} \\
\sigma_i^{n+1,-} &= \frac{1}{\Delta x}\left(U_{i+\frac{1}{2}}^{n+1,-} - U_{i-\frac{1}{2}}^{n+1,-}\right) \\
\sigma_i^{n+1} &= minmod\left(\alpha_\sigma \frac{U_i^{n+1}-U_{i-1}^{n+1}}{\Delta x}, \sigma_i^{n+1,-}, \alpha_\sigma \frac{U_{i+1}^{n+1}-U_i^{n+1}}{\Delta x}\right)
\end{aligned}\right\}
\tag{4.2}
$$

Five 1D shock tube problems are investigated in order to compare high-order algorithms. The numerical results are obtained with the generalized MINMOD limiter where the α_σ coefficient is taken as 1.9 in all solutions. In all cases, the computational domain is divided into $N = 100$ cells, where domain length L is taken as 1, the ratio of specific heats is selected as $\gamma = 1.4$, C_{cfl} is taken as 0.1. In the plots, velocity,
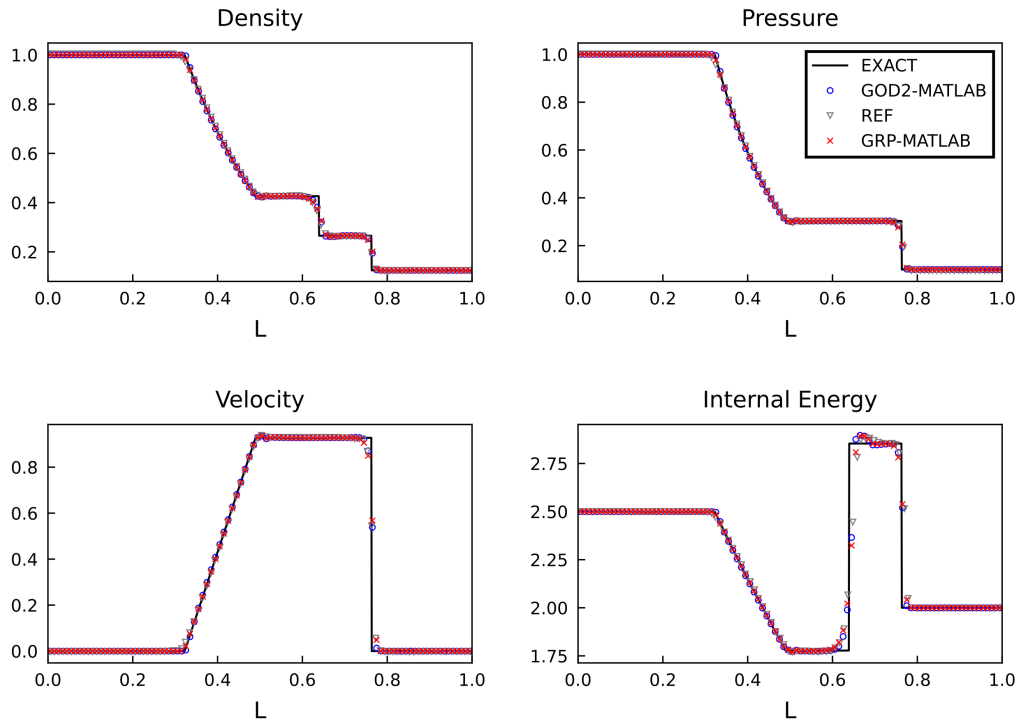
Figure 4.43: Results of Test Case 1

pressure, density, and internal energy variables are presented where exact results are shown by the black line; gray triangles indicate reference results, blue circles demonstrate second-order Godunov scheme results, and red crosses indicate solutions of the GRP method.

4.4.1 Test Case 1

This test case consists of a right shock wave, a left rarefaction wave, and contact discontinuity moving in the right direction where the gas is initially at rest. Initial discontinuity position has chosen as $x_0 = 0.5$. The results at $T = 0.15$ seconds are shown in Figure 4.43.

The rarefaction wave is well approximated by both of the methods, and the results are very close to each other. The shock wave is approximated over three computing cells in both methods without nonphysical oscillations. An overshoot near the contact discontinuity can be seen in both the GRP method and the second-order Godunov scheme with a close magnitude. The solutions are similar in each method and in good
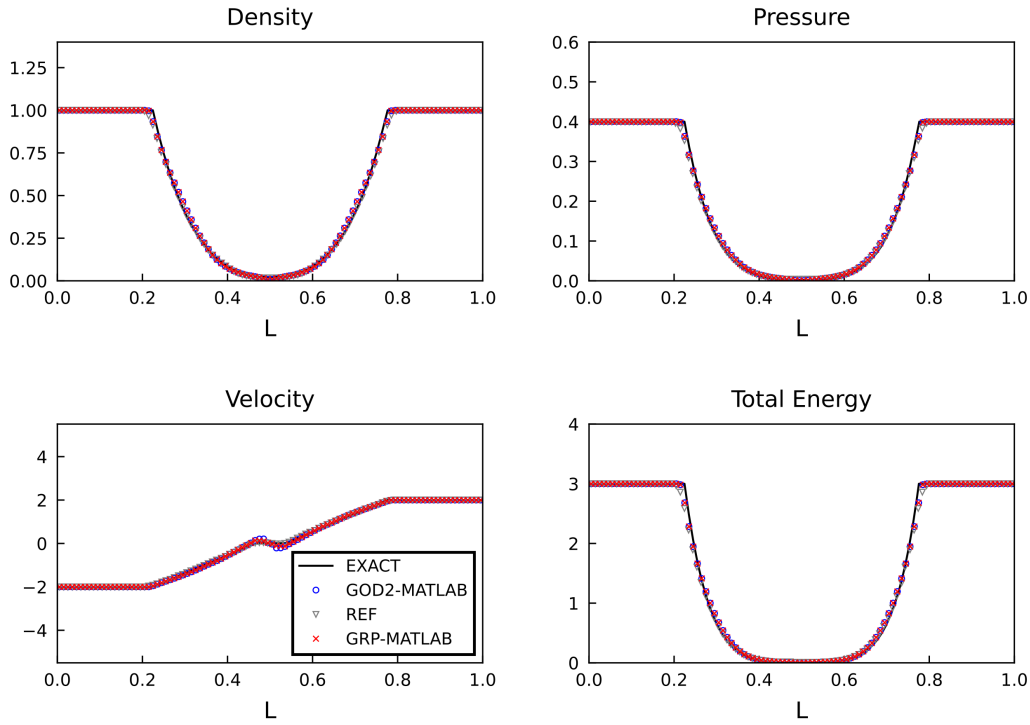
Figure 4.44: Results of Test Case 2

agreement with the reference solution.

4.4.2 Test Case 2

In this test case, a contact discontinuity at $x_0 = 0.5$ with zero speed separates the two symmetric rarefaction waves where the star region is close to the vacuum. The results at $T = 0.1$ seconds are shown in Figure 4.44.

Although both methods show satisfactory results when ρ, u, p, and E are considered, the GRP method has better resolution near the head of the rarefaction waves. Moreover, the GRP method has a lower undershoot and overshoot near the contact discontinuity location, which can be observed from the velocity plot. The results of each scheme are in good agreement with the reference solution. The internal energy, e, results are very similar for the GRP method and second-order Godunov method; the plot is given in figure 4.45.
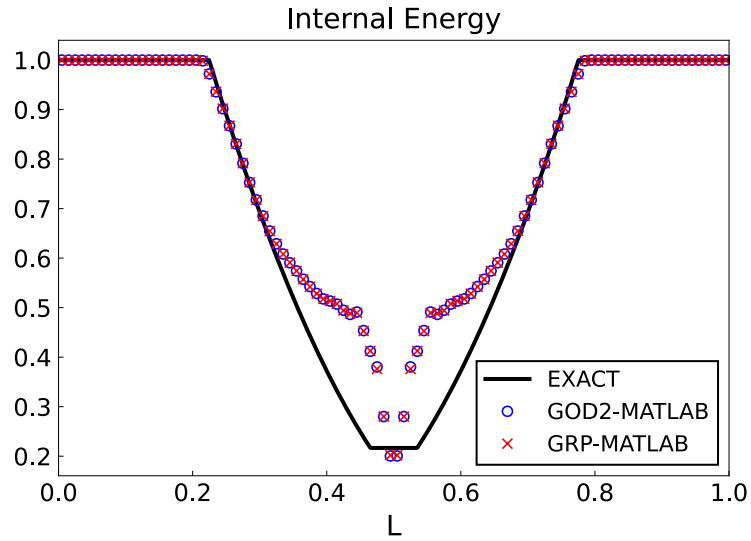
Figure 4.45: Internal Energy Results of Test Case 2

4.4.3 Test Case 3

The results at $T = 0.012$ seconds, where an initial discontinuity is located at $x_0 = 0.5$, are shown in Figure 4.46.

The accuracy of solutions for different variables is the same in the rarefaction wave region.

When the results of the GRP method are compared with the second-order Godunov scheme, the resolution of the shock wave is similar in each method, and the approximation took three cells.

Similar to Test Case 1, the performance at contact discontinuity is worse than the shock wave, which can be seen in the density or energy plot. The GRP method has slightly better results when the magnitude of the density result is considered.

4.4.4 Test Case 4

This problem is obtained by the result of the collision of two severe shock waves moving in reverse directions. The results at $T = 0.035$ seconds are shown in Figure 4.47.

77
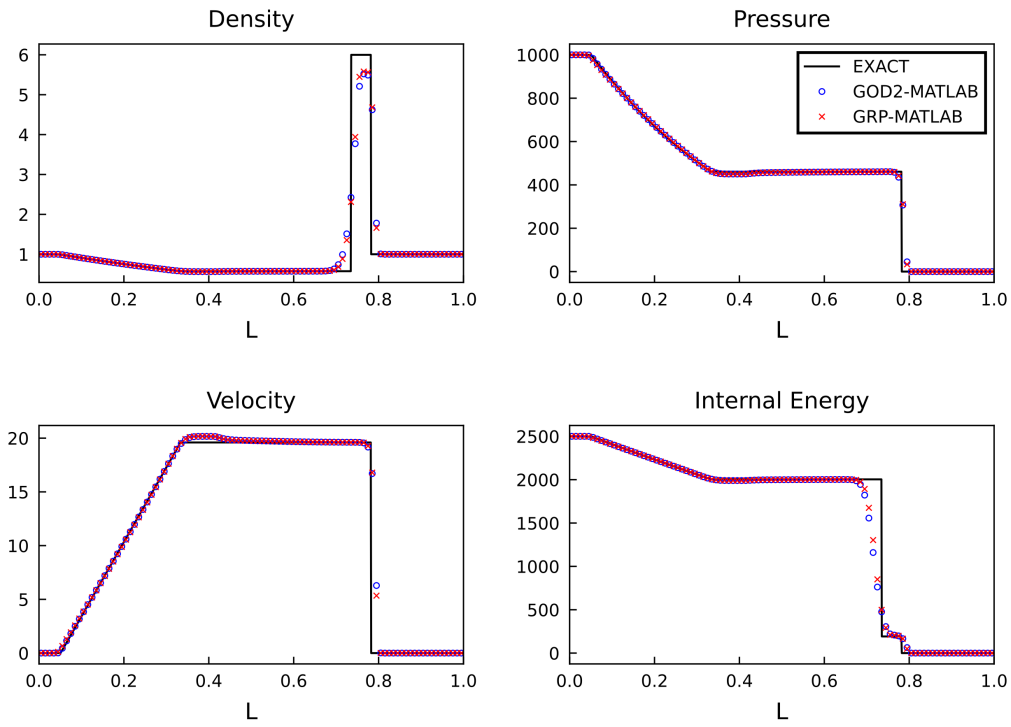
Figure 4.46: Results of Test Case 3
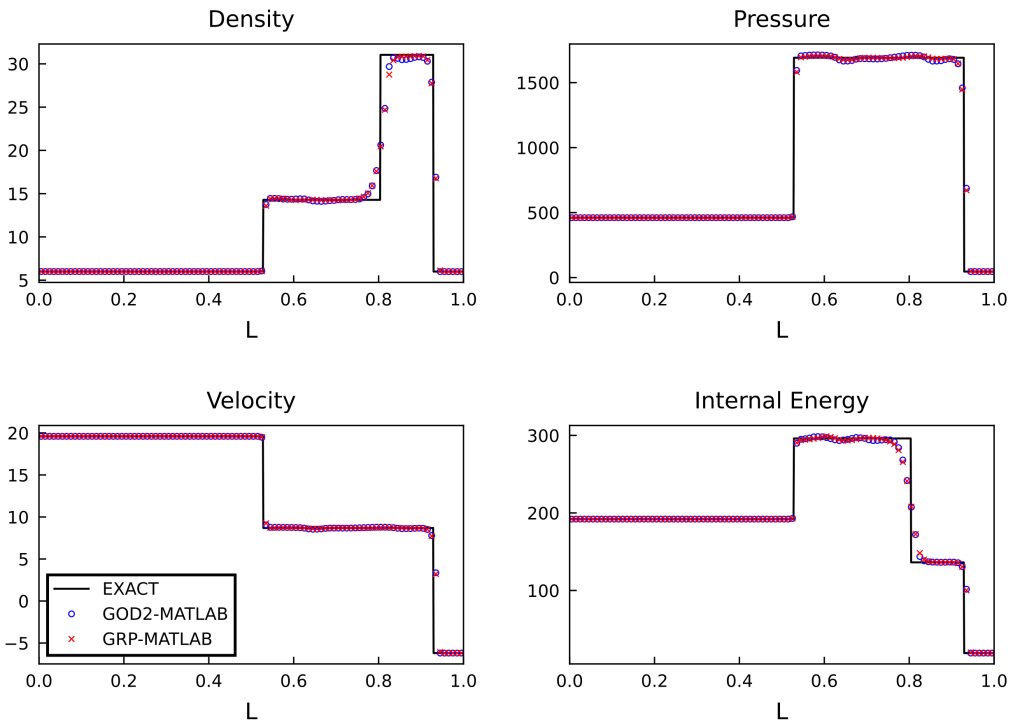
Figure 4.47: Results of Test Case 4
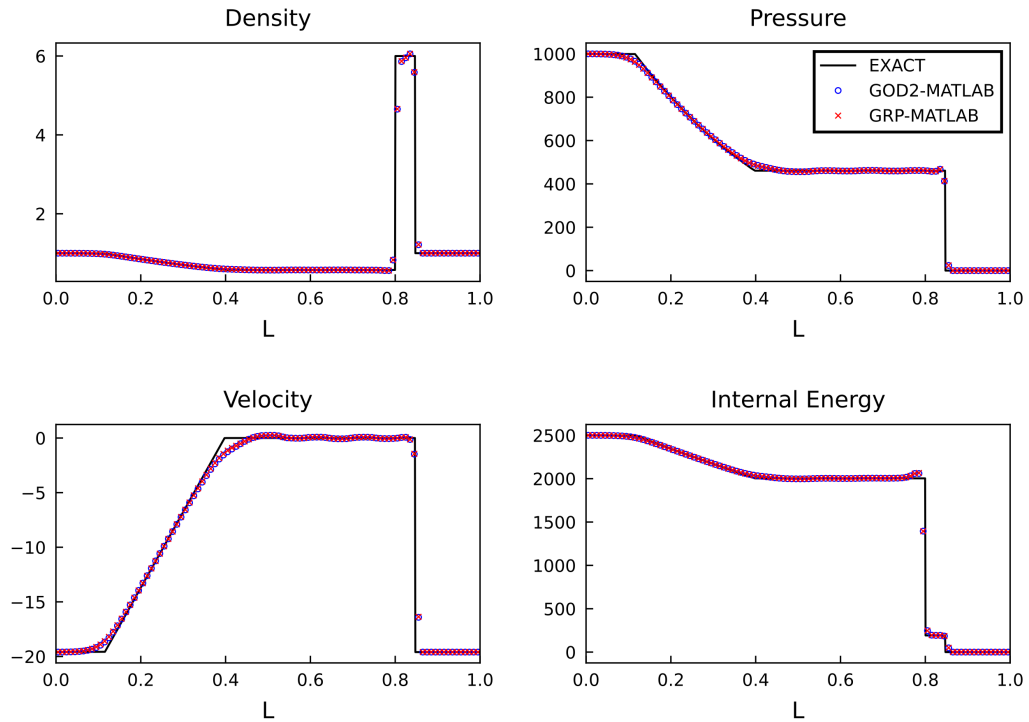
Figure 4.48: Results of Test Case 5

The accuracy of solutions for different variables is the same in the post-shock region. However, in the area between shock wave and contact discontinuity, the two methods have different but close results. The density calculation obtained from the GRP method is closer to the exact solution than the second-order Godunov scheme. Moreover, the magnitude of oscillations in the same area is lower in the results obtained by the GRP method.

4.4.5 Test Case 5

The results of the second-order Godunov scheme and GRP method at $T = 0.012$ seconds are shown in Figure 4.48.

The left-moving rarefaction, the shock wave going to the right, and the contact discontinuity are captured with nearly the same accuracy in both methods except the tail of the rarefaction wave. The magnitude of oscillations before the contact discontinuity is the same for the GRP method and the second-order Godunov scheme.

4.4.6 Discussion on Second-Order Schemes

For one-dimensional results, the accuracy of the GRP method and the second-order Godunov scheme is very close to each other when the same generalized MINMOD limiter is used. It was observed that, in 1D, the effect of the GRP method without limiter contribution was relatively small when compared to the second-order Godunov scheme. The time derivative component, which is the main component that distinguishes the GRP from the second-order Godunov scheme, has an effect less than 0.1%. If the same limiter is used in the solver, a very slight improvement in the accuracy of rarefaction and contact discontinuity is obtained in the GRP method. The effect of the limiter is higher than the time variation of flux for the solution accuracy.

CHAPTER 5

CONCLUSION

In this thesis, a high-order GRP algorithm for the solution of Euler equations is developed and implemented into the in-house, open-source finite volume CFD solver. The implemented code is tested on structured and unstructured meshes, inviscid, viscous, steady, and unsteady flows. This method is also tested for different spatial dimensions with well-known benchmark test cases.

By implementing the GRP method to an open-source CFD solver, second-order spatial accuracy for the convective fluxes is obtained. On the other hand, other methods are used for computing convective fluxes, such as the Godunov method and the HLLC method. Thanks to the GRP method, the second-order accuracy is not achieved by the piece-wise linear reconstruction method only but also by time variation of flux and resolved state. At the cell boundaries, the GRP solution accepts right and left states along with their second-order gradients, which defines the idea of the GRP method. For gradient calculation, the least squares method is used with selectable limiters such as Barth-Jespersen and generalized MINMOD.

With different test cases, the solver is validated for;

- strong rarefaction and strong shock waves,

- near-vacuum problems

- zero-speed contact discontinuities,

- oblique shock waves,

- Prandtl-Meyer expansion fans in multi-dimensions,

- viscous flows,

- complex flow regimes in a three-dimensional domain.

In all these cases, the results of the GRP method are in good agreement with experimental data or analytical results. In addition, it is observed that the improvement of the solution accuracy when the GRP method is used comes from the modified generalized MINMOD limiter.

For future work, to make the solution cheaper, approximate Riemann solvers can be added in the Riemann solution part of the GRP method, where the user can decide depending on the accuracy needs and computational resources. Moreover, a suitable limiter for both the GRP method and the unstructured solver can be developed in order to increase accuracy without oscillations. Finally, an on-off mechanism can be built for the solver when computing convective fluxes where gradients are low; the GRP method could be bypassed.

REFERENCES

[1] E. F. Toro, *Riemann solvers and numerical methods for fluid dynamics: a practical introduction.* Springer Science & Business Media, 2013.

[2] J. Blazek, "Computational fluid dynamics: Principles and applications," 2001.

[3] B. v. Leer, "Flux-vector splitting for the euler equations," in *Eight International Conference on Numerical Methods in Fluid Dynamics*, pp. 507–512, Springer, 1982.

[4] M.-S. Liou and C. J. Steffen Jr, "A new flux splitting scheme," *Journal of Computational physics*, vol. 107, no. 1, pp. 23–39, 1993.

[5] M.-S. Liou, "A sequel to ausm," *Journal of Computational Physics*, vol. 129, no. 2, pp. 364–382, 1996.

[6] A. Jameson, "Positive schemes and shock modelling for compressible flows," *International Journal for Numerical Methods in Fluids*, vol. 20, no. 8-9, pp. 743–776, 1995.

[7] S. Tatsumi, L. Martinelli, and A. Jameson, "A new high resolution scheme for compressible viscous flows with shocks," in *33rd Aerospace Sciences Meeting and Exhibit*, p. 466, 1995.

[8] S. Godunov and I. Bohachevsky, "Finite difference method for numerical computation of discontinuous solutions of the equations of fluid dynamics," *Matematičeskij sbornik*, vol. 47, no. 3, pp. 271–306, 1959.

[9] R. Courant, E. Isaacson, and M. Rees, "On the solution of nonlinear hyperbolic differential equations by finite differences," *Communications on pure and applied mathematics*, vol. 5, no. 3, pp. 243–255, 1952.

[10] C. Farhat, "Numerical methods for compressible flows." `https://web.stanford.edu/group/frg/course_work/AA214/CA-AA214-Ch5.pdf`. Last accessed on July 28, 2022.

[11] A. Harten, P. D. Lax, and B. v. Leer, "On upstream differencing and godunov-type schemes for hyperbolic conservation laws," *SIAM review*, vol. 25, no. 1, pp. 35–61, 1983.

[12] S. Osher and F. Solomon, "Upwind difference schemes for hyperbolic systems of conservation laws," *Mathematics of computation*, vol. 38, no. 158, pp. 339–374, 1982.

[13] P. L. Roe, "Approximate riemann solvers, parameter vectors, and difference schemes," *Journal of computational physics*, vol. 43, no. 2, pp. 357–372, 1981.

[14] B. Einfeldt, "On godunov-type methods for gas dynamics," *SIAM Journal on numerical analysis*, vol. 25, no. 2, pp. 294–318, 1988.

[15] E. F. Toro, M. Spruce, and W. Speares, "Restoration of the contact surface in the hll-riemann solver," *Shock waves*, vol. 4, no. 1, pp. 25–34, 1994.

[16] S. Davis, "Simplified second-order godunov-type methods," *SIAM Journal on Scientific and Statistical Computing*, vol. 9, no. 3, pp. 445–473, 1988.

[17] P. Batten, N. Clarke, C. Lambert, and D. M. Causon, "On the choice of wavespeeds for the hllc riemann solver," *SIAM Journal on Scientific Computing*, vol. 18, no. 6, pp. 1553–1570, 1997.

[18] P. Batten, M. Leschziner, and U. Goldberg, "Average-state jacobians and implicit methods for compressible viscous and turbulent flows," *Journal of computational physics*, vol. 137, no. 1, pp. 38–78, 1997.

[19] V. Kolgan, "Application of the principle of minimizing the derivative to the construction of finite-difference schemes for computing discontinuous solutions of gas dynamics," *Sci. Notes TsAGI 3*, pp. 68–77, 1972.

[20] B. Van Leer, "Towards the ultimate conservative difference scheme. v. a second-order sequel to godunov's method," *Journal of computational Physics*, vol. 32, no. 1, pp. 101–136, 1979.

[21] M. Siavashi, "Total variation diminishing (tvd) methods." `http://www.iust.ac.ir/files/mech/siavashim_f1039/files/TVD_methods.pdf`. Last accessed on July 28, 2022.

[22] B. v. Leer, "Towards the ultimate conservative difference scheme i. the quest of monotonicity," in *Proceedings of the Third International Conference on Numerical Methods in Fluid Mechanics*, pp. 163–168, Springer, 1973.

[23] P. L. Roe, "Some contributions to the modelling of discontinuous flows," *Large-scale computations in fluid mechanics*, pp. 163–193, 1985.

[24] G. van Albada, B. v. Leer, *et al.*, "A comparative study of computational methods in cosmic gas dynamics," *Astronomy and Astrophysics*, vol. 108, pp. 76–84, 1982.

[25] F. Zhang, J. Liu, and B. Chen, "Modified multi-dimensional limiting process with enhanced shock stability on unstructured grids," *Computers & Fluids*, vol. 161, pp. 171–188, 2018.

[26] T. Barth and D. Jespersen, "The design and application of upwind schemes on unstructured meshes," in *27th Aerospace sciences meeting*, p. 366, 1989.

[27] V. Venkatakrishnan, "On the accuracy of limiters and convergence to steady state solutions," in *31st Aerospace Sciences Meeting*, p. 880, 1993.

[28] J. Qian, J. Li, and S. Wang, "The generalized riemann problems for compressible fluid flows: Towards high order," *Journal of Computational Physics*, vol. 259, pp. 358–389, 2014.

[29] J. Qian, J. Li, and S. Wang, "The generalized riemann problems for hyperbolic balance laws: A unified formulation towards high order," *arXiv preprint arXiv:1303.2941*, 2013.

[30] M. Ben-Artzi and J. Falcovitz, "A second-order godunov-type scheme for compressible fluid dynamics," *Journal of Computational Physics*, vol. 55, no. 1, pp. 1–32, 1984.

[31] M. Ben-Artzi and J. Falcovitz, "An upwind second-order scheme for compressible duct flows," *SIAM journal on scientific and statistical computing*, vol. 7, no. 3, pp. 744–768, 1986.

[32] M. Ben-Artzi, "The generalized riemann problem for reactive flows," *Journal of Computational physics*, vol. 81, no. 1, pp. 70–101, 1989.

[33] P. Le Floch and P.-A. Raviart, "An asymptotic expansion for the solution of the generalized riemann problem part i: General theory," in *Annales de l'Institut Henri Poincaré C, Analyse non linéaire*, vol. 5, pp. 179–207, Elsevier, 1988.

[34] A. Bourgeade, P. Le Floch, and P. Raviart, "An asymptotic expansion for the solution of the generalized riemann problem. part 2: Application to the equations of gas dynamics," in *Annales de l'Institut Henri Poincaré C, Analyse non linéaire*, vol. 6, pp. 437–480, Elsevier, 1989.

[35] M. Ben-Artzi and J. Falcovitz, *Generalized Riemann problems in computational fluid dynamics*, vol. 11. Cambridge University Press, 2003.

[36] M. Ben-Artzi, J. Li, and G. Warnecke, "A direct eulerian grp scheme for compressible fluid flows," *Journal of Computational Physics*, vol. 218, no. 1, pp. 19–43, 2006.

[37] M. Ben-Artzi and J. Li, "Hyperbolic balance laws: Riemann invariants and the generalized riemann problem," *Numerische Mathematik*, vol. 106, no. 3, pp. 369–425, 2007.

[38] J. Li and G. Chen, "The generalized riemann problem method for the shallow water equations with bottom topography," *International journal for numerical methods in engineering*, vol. 65, no. 6, pp. 834–862, 2006.

[39] K. Wu, Z. Yang, and H. Tang, "A third-order accurate direct eulerian grp scheme for the euler equations in gas dynamics," *Journal of Computational Physics*, vol. 264, pp. 177–208, 2014.

[40] L. Pan, K. Xu, Q. Li, and J. Li, "An efficient and accurate two-stage fourth-order gas-kinetic scheme for the euler and navier–stokes equations," *Journal of Computational Physics*, vol. 326, pp. 197–221, 2016.

[41] J. Li and Z. Du, "A two-stage fourth order time-accurate discretization for lax–wendroff type flow solvers i. hyperbolic conservation laws," *SIAM Journal on Scientific Computing*, vol. 38, no. 5, pp. A3046–A3069, 2016.

[42] Z. Du and J. Li, "A two-stage fourth order time-accurate discretization for lax–wendroff type flow solvers ii. high order numerical boundary conditions," *Journal of Computational Physics*, vol. 369, pp. 125–147, 2018.

[43] Z. Du and J. Li, "A hermite weno reconstruction for fourth order temporal accurate schemes based on the grp solver for hyperbolic conservation laws," *Journal of Computational Physics*, vol. 355, pp. 385–396, 2018.

[44] Z. Yang and H. Tang, "A direct eulerian grp scheme for relativistic hydrodynamics: two-dimensional case," *Journal of Computational Physics*, vol. 231, no. 4, pp. 2116–2139, 2012.

[45] K. Wu and H. Tang, "A direct eulerian grp scheme for spherically symmetric general relativistic hydrodynamics," *Siam Journal on Scientific Computing*, vol. 38, no. 3, pp. B458–B489, 2016.

[46] J. Li and Y. Wang, "Thermodynamical effects and high resolution methods for compressible fluid flows," *Journal of Computational Physics*, vol. 343, pp. 340–354, 2017.

[47] C. Berthon, C. Sarazin, and R. Turpault, "Space-time generalized riemann problem solvers of order k for linear advection with unrestricted time step," *Journal of Scientific Computing*, vol. 55, no. 2, pp. 268–308, 2013.

[48] E. Han, J. Li, and H. Tang, "An adaptive grp scheme for compressible fluid flows," *Journal of Computational Physics*, vol. 229, no. 5, pp. 1448–1466, 2010.

[49] Q. Zhang and W. Sheng, "A random choice method based on the generalized riemann problem for the euler equations in gas dynamics," *Journal of Computational Physics*, vol. 441, p. 110431, 2021.

[50] E. F. Toro, R. Millington, and L. Nejad, "Towards very high order godunov schemes," in *Godunov methods*, pp. 905–937, Springer, 2001.

[51] V. A. Titarev and E. F. Toro, "Ader: Arbitrary high order godunov approach," *Journal of Scientific Computing*, vol. 17, no. 1, pp. 609–618, 2002.

[52] V. A. Titarev and E. F. Toro, "Ader schemes for three-dimensional non-linear hyperbolic systems," *Journal of Computational Physics*, vol. 204, no. 2, pp. 715–736, 2005.

[53] G. I. Montecinos and E. F. Toro, "Reformulations for general advection–diffusion–reaction equations and locally implicit ader schemes," *Journal of Computational Physics*, vol. 275, pp. 415–442, 2014.

[54] C. E. Castro and E. F. Toro, "Solvers for the high-order riemann problem for hyperbolic balance laws," *Journal of Computational Physics*, vol. 227, no. 4, pp. 2481–2513, 2008.

[55] A. Taube, M. Dumbser, D. S. Balsara, and C.-D. Munz, "Arbitrary high-order discontinuous galerkin schemes for the magnetohydrodynamic equations," *Journal of Scientific Computing*, vol. 30, no. 3, pp. 441–464, 2007.

[56] C. Goetz and A. Iske, "Approximate solutions of generalized riemann problems for nonlinear systems of hyperbolic conservation laws," *Mathematics of Computation*, vol. 85, no. 297, pp. 35–62, 2016.

[57] C. R. Goetz and M. Dumbser, "A novel solver for the generalized riemann problem based on a simplified lefloch–raviart expansion and a local space–time discontinuous galerkin formulation," *Journal of Scientific Computing*, vol. 69, no. 2, pp. 805–840, 2016.

[58] E. Luke, X. Tong, and R. Chamberlain, "Flowpsi: An ideal gas flow solver-the user guide," *sourceforge. net, Starkville*, pp. 29–40, 2016.

[59] E. F. Toro, "He-e1rpexact - exact riemann solver for the time-dependent one dimensional euler equations." `https://github.com/wme7/Aero-shock/blob/master/Numerica/hyper_eul/ONEDIM/E1RPEX.F`. Last accessed on September 03, 2022.

[60] G. A. Sod, "A survey of several finite difference methods for systems of nonlinear hyperbolic conservation laws," *Journal of computational physics*, vol. 27, no. 1, pp. 1–31, 1978.

[61] B. Einfeldt, C.-D. Munz, P. L. Roe, and B. Sjögreen, "On godunov-type methods near low densities," *Journal of computational physics*, vol. 92, no. 2, pp. 273–295, 1991.

[62] P. Woodward and P. Colella, "The numerical simulation of two-dimensional fluid flow with strong shocks," *Journal of computational physics*, vol. 54, no. 1, pp. 115–173, 1984.

[63] "Nparc alliance verification and validation archive." `https://www.grc.nasa.gov/www/wind/valid/archive.html`. Last accessed on September 03, 2022.

[64] I. B. Celik, U. Ghia, P. J. Roache, and C. J. Freitas, "Procedure for estimation and reporting of uncertainty due to discretization in cfd applications," *Journal of fluids Engineering-Transactions of the ASME*, vol. 130, no. 7, 2008.

[65] "Su2 code, tutorials." `https://su2code.github.io/tutorials/Inviscid_Wedge/`. Last accessed on September 03, 2022.

[66] J. W. Slater, "Nparc alliance verification and validation archive." `https://www.grc.nasa.gov/www/wind/valid/raetaf/geom.txt`. Last accessed on September 03, 2022.

[67] P. Cook, M. McDonald, and M. Firmin, "Aerofoil rae 2822-pressure distributions, and boundary layer and wake measurements. experimental data base for computer program assessment," *AGARD Report AR*, vol. 138, 1979.

[68] J. W. Slater, "Nparc alliance verification and validation archive." `https://www.grc.nasa.gov/www/wind/valid/raetaf/raetaf04/cp.nparc.gen`. Last accessed on September 03, 2022.

[69] J. W. Slater, "Nparc alliance verification and validation archive." `https://turbmodels.larc.nasa.gov/onerawingnumerics_val.html`. Last accessed on September 03, 2022.

[70] V. Schmitt, "Pressure distributions on the onera m6-wing at transonic mach numbers, experimental data base for computer program assessment," *AGARD AR-138*, 1979.

[71] J. T. Batina, "Accuracy of an unstructured-grid upwind-euler algorithm for the onera m6 wing," *Journal of aircraft*, vol. 28, no. 6, pp. 397–402, 1991.